1.0

1.1

1.25   1.4   1.6

4.5   2.8   2.5
5.0   3.2   2.2
5.6   3.6
6.3   4.0   2.0

1.8

MICROCOPY RESOLUTION TEST CHART
NATIONAL BUREAU OF STANDARDS-1963-A

FURTHER ASSESSMENT OF INFRARED DATA FROM AIRCRAFT AND ROCKET PROBES

AD A089724

PhotoMetrics, Inc.

442 Marrett Road

Lexington, Massachusetts 02173

30 November 1979

Final Report for Period 1 December 1978—31 October 1979

CONTRACT No. DNA 001-79-C-0013

> **APPROVED FOR PUBLIC RELEASE;**
> **DISTRIBUTION UNLIMITED.**

DTIC
ELECTE
S SEP 30 1980 **D**

B

Prepared for

Director

DEFENSE NUCLEAR AGENCY

Washington, D. C. 20305

80 9 16 010

C950 467L

REPORT DOCUMENTATION PAGE	READ INSTRUCTIONS BEFORE COMPLETING FORM	
1. REPORT NUMBER DNA 5127F	2. GOVT ACCESSION NO.	3. RECIPIENT'S CATALOG NUMBER
4. TITLE (and Subtitle) FURTHER ASSESSMENT OF INFRARED DATA FROM AIRCRAFT AND ROCKET PROBES.	5. TYPE OF REPORT & PERIOD COVERED Final Report for Period 1 Dec 78—31 Oct 79	
	6. PERFORMING ORG. REPORT NUMBER PhM-05-79	
7. AUTHOR(s) I. L. Kofsky D. P. Villanucci	8. CONTRACT OR GRANT NUMBER(s) DNA 001-79-C-0013	
9. PERFORMING ORGANIZATION NAME AND ADDRESS PhotoMetrics, Inc. 442 Marrett Road Lexington, Massachusetts 02173	10. PROGRAM ELEMENT, PROJECT, TASK AREA & WORK UNIT NUMBERS Subtask I25AAXHX639-05	
11. CONTROLLING OFFICE NAME AND ADDRESS Director Defense Nuclear Agency Washington, D.C. 20305	12. REPORT DATE 30 Nov 79	
	13. NUMBER OF PAGES 136	
14. MONITORING AGENCY NAME & ADDRESS(if different from Controlling Office)	15. SECURITY CLASS (of this report) UNCLASSIFIED	
	15a. DECLASSIFICATION/DOWNGRADING SCHEDULE	

16. DISTRIBUTION STATEMENT (of this Report)

Approved for public release; distribution unlimited.

17. DISTRIBUTION STATEMENT (of the abstract entered in Block 20, if different from Report)

18. SUPPLEMENTARY NOTES

This work sponsored by the Defense Nuclear Agency under RDT&E RMSS Code B322078462 I25AAXHX63905 H2590D.

19. KEY WORDS (Continue on reverse side if necessary and identify by block number)

Nuclear-Effects Simulation	Ionosphere Modification
Daytime Aurora	Upper Atmosphere
Infrared Radiation	
Radiometry and Photometry	

20. ABSTRACT (Continue on reverse side if necessary and identify by block number)

Measurements from an aircraft and rockets of the yield of 2.8-3.1 μm-band photons from air irradiated by ionizing particles are evaluated. The nighttime column emission in aurora, viewed from below by a sensitive radiometer with $<$1 km field of view, is found to be temporally-spatially correlated with the column energy input to within a few sec and a few km. The "equilibrium" chemiluminous efficiency in the SWIR band, measured with lower-resolution instruments in several hr of flight, shows statistically-significant variations of about a factor two (data from 1976 missions,

DD FORM 1473 EDITION OF 1 NOV 65 IS OBSOLETE
1 JAN 73

20. ABSTRACT (Continued)

reported in HAES 79, lie in a narrower range). Its mean value is very near
that expected from laboratory and HAES rocket measurements. Altitude pro-
files of the SWIR photon yield from two DNA/AFGL rockets have a pronounced
minimum near 110 km altitude, qualitatively similar to that predicted by
models of collisional quenching of vibrationally-excited nitric oxide
molecules by oxygen atoms.

The aircraft-borne instruments' capability for measuring SWIR yields from
the sunlit auroral atmosphere is demonstrated. Results from attempted
coordination of moving fields of view with the Chatanika incoherent-scatter
radar's steerable beam are assessed; little useful data overlap is found.
Energy input within the fields of infrared spectrometers and radiometers
carried by two rocket probes are calculated from ground photometry data.

Preliminary results of the aircraft's photometric (including airglow-
sensitive video) and radiometric measurements on the ionospheric plasma
depletion produced by release of H_2^n and H_2O from an Atlas Centaur rocket
engine are presented. Intense OI forbidden line emission extending over
$\sim 10^5$ km^2 resulted, as well as a persisting increase in the zenith back-
ground in the 2.8-3.1 μm band. We tentatively interpret this F-region SWIR
glow as due to selective population of low vibrational states of hydroxyl
in electron recombination reactions.

SUMMARY

The objective of the work reported here is to assess and evaluate data taken from a DNA/AFGL KC-135 aircraft and sounding rockets on atmospheric optical/IR radiations whose excitation simulates that from nuclear explosions. In addition auroral particle energy inputs were determined for normalization and scaling of rocket measurements of infrared photon yields and emission spectra, and preliminary results were obtained from aircraft radiometry of the widespread ($\sim 10^5$ km^2) airglows produced when exhaust gases from a satellite launch vehicle deplete the ionosphere plasma.

Vertical column-integrated yields of $2.8 - 3.1 \mu$m-band photons from the ionizing particle-irradiated upper atmosphere were measured from altitudes above the absorbing water vapor layer by aircraft instruments with 10° fields of view and ~ 30 sec integration time. The cumulative results from some 16 hr of flight under IBC $\gtrsim$ II aurora show variations of about a factor two (the data from the earlier missions, reported in Ref 1 (HAES 79), fall in a narrower range). When this emission is given its usual interpretation as nitric oxide vibrational radiation excited in aerochemical reactions following ionization of air, the chemiluminous efficiency in the complete NO overtone sequence is $0.35 - 0.7\%$. This flight segment-to-segment variability, which is statistically significant, is not yet explained.

Measurements with a sensitive narrow-angle (0.4° square field), rapid-response (< 1 sec) radiometer and photometer recently installed on the aircraft show this nighttime emission correlated with the particle energy input to within a few sec and a few km horizontally. These high-resolution data indicate that the spatial-temporal inhomo-geneities in the SWIR background that is produced by nuclear explosions are very similar to those observed at visible wavelengths (by, for example, photographic cameras deployed at past tests). Further quantitative information about the infrared structure and source is present in the data. The chemiluminescent efficiency in the 2.9μm -

1

band measured from DNA's auroral dynamics rocket (Section 3) shows
a pronounced minimum near 110 km altitude, similar to that reported
in a previous HAES rocket investigation.   This finding, taken with
the simultaneously-measured altitude profile of [O], can be used to
verify computer models of quenching of $NO^{\ddagger}$ by the atmosphere's
O atoms.

The capability of the aircraftborne instruments to measure
both SWIR and energy input-indicating visible emission when the
auroral altitudes are in sunlight – that is, to determine daytime
SWIR yields – is demonstrated from past flight data (Section 5).
Results from attempted coordination of the moving instrument fields
with the beam of the DNA 617 incoherent-scatter radar(at Chatanika,
AK) are assessed (Section 4); it is found that multi-spectral photo-
metry data taken from the aircraft platform itself provide a more
useful measure of charged-particle energy inputs and deposition
altitudes.

Deposition of energy into the fields of HIRIS II's interferometric
spectrometer (Section 2) and the 1978 auroral dynamics rocket's
4. 3μm radiometer (Section 3) is calculated from the groundbased
photometry and Chatanika radar data. The measurements of 2. 9μm-
band radiation taken on upleg of the 1974 multi-instrumented rocket
(A18. 219-1) are found to be too inconsistent for further consideration.

A preliminary assessment was made of data taken with the
aircraft instruments (with some modifications) on the airglows
excited over a large area of the Atlantic Ocean by the H_2 and H_2O
molecule exhaust of the Centaur upper-stage engine on 20 Sep 79(Section 7).
The OI forbidden-line intensities were considerably higher than
predicted, and an unexpected increase in the 2. 8 - 3. 1μm background
from the F-region was observed. We postulate that this SWIR glow
near 400 km altitude arises from selective population of low vibrational
states of OH in electron recombination reactions. The aircraft's

2

low light level video camera images are high-resolution, radiometrically-calibrated maps of the column rate of depletion of the ionospheric plasma in the reactions following the gas release. The optical/IR measurements of the growth and transport of the $\sim 10^7$ km^3 electron-underdense volume ("hole") are compared with results from electromagnetic sensors.

PREFACE

This report, which is HAES (High Altitude Effects Simulation) No.   and the Final Report on Contract DNA001-79-C-0013, covers PhotoMetrics' work in evaluating field data on optical/IR sky backgrounds in the period 01 Dec 78 - 31 Oct 79. A current bibliography of all reports in the HAES series is maintained and available on request at DASIAC, DoD Nuclear Information and Analysis Center, 816 State St., Santa Barbara, CA 93102, Telephone (805)965-0551. Summaries of results from the HAES program were presented at two Infrared Data Reviews sponsored by the Defense Nuclear Agency, held 13-15 Jun 77 (at Falmouth, MA) and 10-12 Apr 79 (Bedford, MA), proceedings of which are also available from DASIAC.

Simulation data from the following sources are evaluated.

HIRIS II rocket IC630.02-1A, launched from
Poker Flat Research Range, AK on 01 Apr 76;

Auroral Dynamics Rockets IC807.15-1 and
IR807.57-1, launched from Poker on 26 Oct 78;

USAF NKC-135A 55-3120 (Air Force Geophysics
Laboratory's IR-Optical Flying Laboratory),
aircraft missions performed under DNA
sponsorship from Eielson AFB, AK and
Pease AFB, NH in 1976-79.

In addition, some of the radiometry data from rocket A18.219-1 (1974) are assessed and found to be of insufficient quality for futher evaluation.

This work was done under the direction of I.L. Kofsky, to whom questions about it should be addressed. Mrs. C.C. Rice was responsible for typing the manuscript, and Ms. Z. Reinhardt contributed to the photoreproduction work. Supporting information was provided by many of the staff of the Air Force Geophysics Laboratory's

4

TABLE OF CONTENTS

TABLE OF CONTENTS (continued)

LIST OF ILLUSTRATIONS

LIST OF ILLUSTRATIONS (continued)

Blank

SECTION 1

EVALUATION OF SWIR INTENSITY AND STRUCTURE DATA FROM THE DNA/AFGL AIRCRAFT

INTRODUCTION

Measurements of chemiluminous yield in the 2.8-3.1μm band from auroral particle-excited air were made from AFGL's IR/Optical Flying Laboratory (USAF NKC-135A S/N 55-3120) in flights from Eielson AFB, AK between 27 Aug and 07 Sep 1978. This Section evaluates these data using the standard procedure described in Section 1 of Ref 1, and compares the results to those from missions with the same 10°-field, zenith-pointing instruments in 1975 - 77. Preliminary data from a coaligned radiometer and photometer with very narrow field (0.4°, or less than 1 km at energy deposition altitudes), which was flown in 1979, are also presented. The principal goal of this flight program (Appendix I of Ref 1) is to investigate the sources of SWIR emission resulting from excitation of air by nuclear radiations, and to establish their spatial and temporal correlation with the deposition of ionizing-particle energy in the upper atmosphere.

Background information on the aircraft program is in Section 1 and Appendix I of Ref 1. Fig 1 illustrates the pointing from the aircraft of the wide-field (flown in 1975-78) and narrow-field (1979) instruments, and the narrower of the two fields of view of the low light level video camera used to assess the temporal-spatial structure of the particle precipitation and to measure upper-atmospheric dosing previous to the arrival of the radiometer. It also shows (upper right) a typical trajectory of the aircraft across the rotating auroral oval. Particular reference is made to the descriptions of the 10°-circular field filter radiometer (Ref 2) and the liquid nitrogen-cooled 0.4°-field instrument (Ref 1), which is tilted 13° forward to point along the local geomagnetic field line in southward flight at auroral latitudes. As noted, we apply the systematic (and nominally unbiased) statistical procedure developed in Ref 1 to derive energy efficiencies for what

13

0.6km

~17km at 110 km altitude

Q = 3 Auroral Oval

0.36°
1979

1975-1978

80°

LOW LIGHT LEVEL VIDEO

2.832-3.125μm

70°

TYPICAL FLIGHT PATH

13°

2.828-3.041 μm RADIOMETER, 3914Å PHOTOMETER + SUPPORT INSTRUMENTS

53120
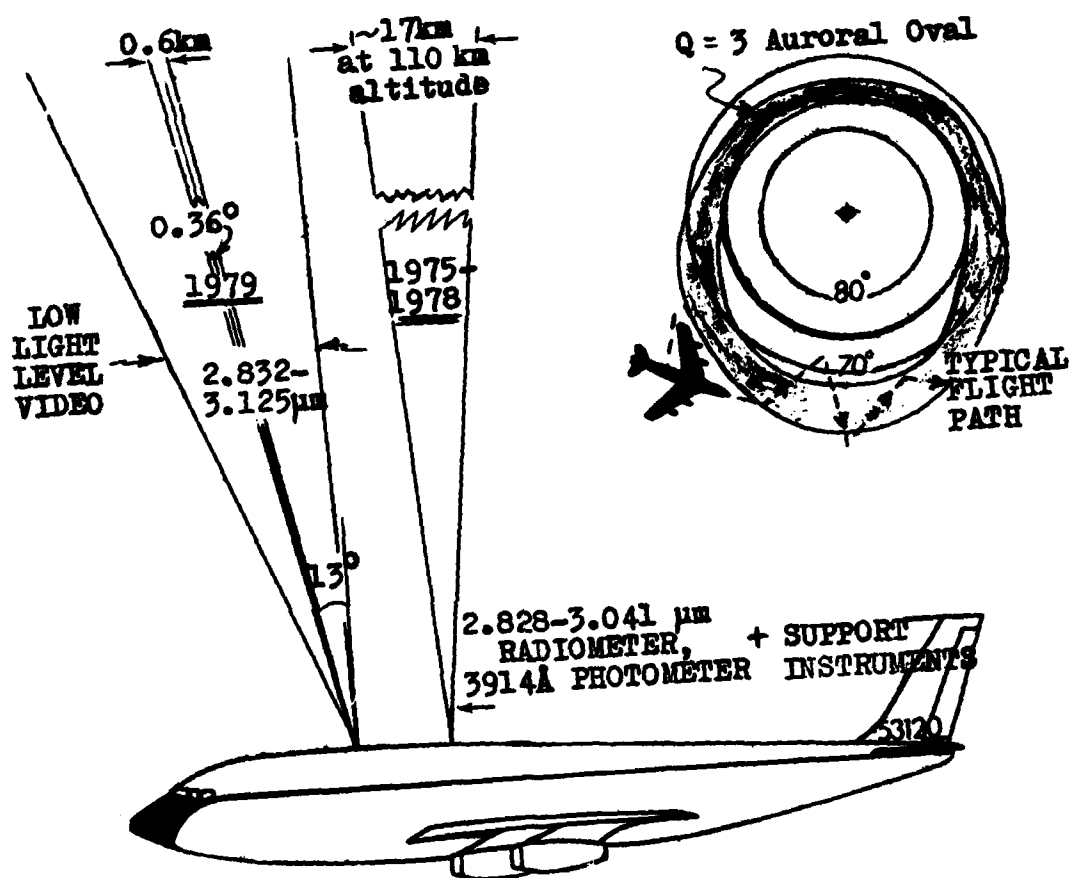
Figure 1. Schematic diagram of wide- and narrow-field radiometry of particle precipitation-associated SWIR enhancements from the AFGL / DNA aircraft (see also Fig 34, which shows the wavelength-cycling photometer, OH Δ v=2 monitor, and all-sky camera field).

we interpret as chemiluminescence in the vibrational overtone of nitric oxide. These NO molecules are thought to become excited in aerochemical reactions of the type summarized in Fig 3 in Appendix I of Ref 1 (and are collisionally deactivated by O atoms, as discussed in Sections 3 and 5).

RESULTS FROM THE WIDE-FIELD RADIOMETER AND PHOTOMETER

Fig 2 shows the spectral response of the zenith-pointing radiometer (Ref 3), the intensity distribution in the NO $\Delta v = 2$ sequence derived from initial-state population measurements in a cryocooled laboratory reaction chamber (Ref 4), and the transmission of the atmosphere above the aircraft. Sky background intensities from mesospheric airglow in the hydroxyl fundamental bands (typically, 100 kR) and lower atmospheric thermal emission (~10 kR), which vary very slowly compared to the particle precipitation-associated radiations, are documented in Table 2 of Ref 1 and in Ref 3. Aircraft measurement operations are described in Ref 1.

The data were received in the standard radiance-vs-time format provided by the measurement group (Fig 1 of Ref 1 is an example). IBC $\gtrsim$ II aurora — which results in SWIR enhancements with adequate signal/noise — was in the aircraft's zenith in 4 of the 21 hr of flight in the Alaska midnight sector. Selection of these segments is the only conscious bias in the data assessment process. The signals from the radiometers and air fluorescence photometers had been digitally pre-integrated for 35 sec (flights 820 (27 Aug), 824 (02 Sep) and 826 (07 Sep)) or $2\frac{1}{2}$ sec (flight 821 (28 Aug)). Within the ~3/4 min, 17 km resolution of the measurements, the SWIR radiances closely follow the power input, without any discernible systematic offset or "spread" – just as did those in the earlier flight series.

We reduced these records by first enlarging them 3X photographically, and then manually reading the traces at a uniform (15 sec)
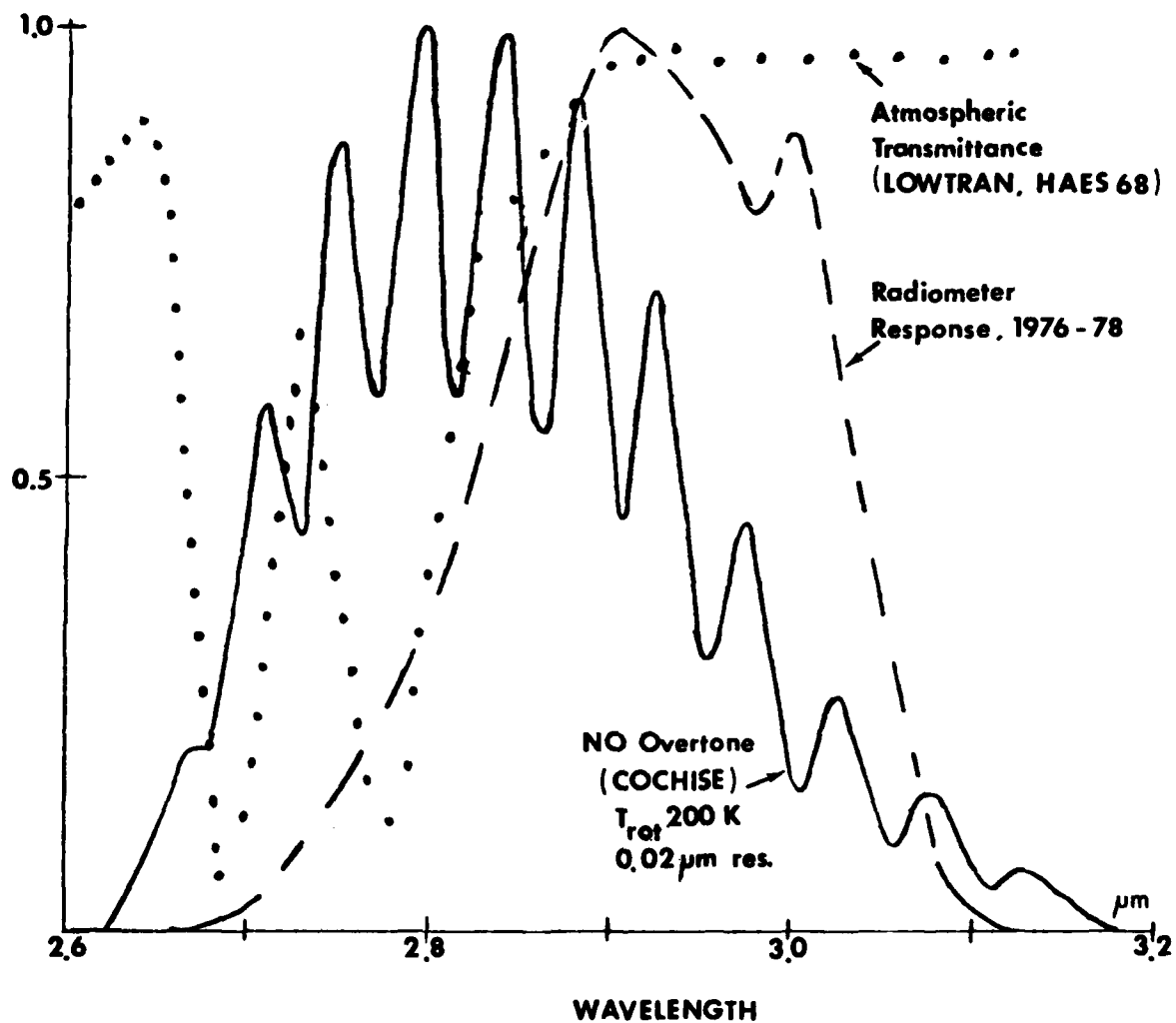
Figure 2. Expected emission spectrum in the nitric oxide overtone, transmission of the atmosphere above the aircraft, and response of the aircraft radiometer.

sampling interval without smoothing or forcing alignment of maximums.
(Data for flight 826 were received on a compressed time scale, so
that the minimum effective sampling interval was 60 sec.) The
radiances measured by the $1.7\mu m$ OH overtone monitor were as usual
corrected for their small air-fluorescence component before being
scaled to subtract out the fundamental-sequence intensities. Table 1
summarizes the procedures applied in assessing the data from the
twelve 1978 and earlier aircraft flights.

Cross-plots of the simultaneously measured $2.9\mu m$ and 3914 Å -
band column intensities in the four useful 1978 data segments are shown in
Fig's 3a-d. The straight lines are least-squares fits calculated with
two uniform and proportional-to-signal weightings, as described in
Ref 1. Chemiluminous energy efficiencies for the entire nitric oxide
overtone sequence determined from the slopes of these best-fit lines
by the procedure outlined in Table 1, along with confidence limits
and correlation coefficients calculated as in Ref 1, are on each figure.
Note that the procedure explicitly assumes that all of the $NO^{\ddagger}$ is
populated by $N^2D + O_2$ reactions, and that the cascade spectrum is
not warped by collisional quenching.

Table 2 compares these new results with those from previous data
flights. The chemiluminous yields by and large apply to E-region air
in which the duration of near-constant particle bombardment is com-
parable to the time for the reactions producing $NO^{\ddagger}$ to go to completion
("equilibrium" irradiation). Yields from the 1978 flights are generally
higher ($\sim 50\%$) than the average $0.4_5\%$ from most of the earlier data
segments. (The variability in 1977 may be due to changes in the radio-
meter's sensitivity, as discussed in Section 1 of Ref 1; otherwise,
periodic calculations by the instrument group indicated its respons-
ivity was constant within 10% for all the measurements.) In three
of the four 1978 segments the efficiency within its statistical un-
certainty checks with the mean figure of 0.6% measured by side-
looking instruments from HAES rockets A18.219-1 (1974, Section II
of Ref 5) and IC807.15-1 (1978, Section 3).

17

Table 1 . Summary of procedures in evaluation of aircraft data

- Corrections for SWIR air fluorescence and hydroxyl airglow:

  (0.2kR/kR 3914 Å) subtracted from 1.7μm readings

  (C kR/kR 1.7μm)   subtracted from 2.9μm readings

	Flight	C (observed)	C (theoretical)
HAES 69	IC-75-4	-	1.3
	76-6	1.7	2.1
	76-9	1.7	2.1
	76-10	1.7	2.1
HAES 79	76-16	2.1	2.1
	#720	0.85	2.1
	#724	0.36	2.1
	#725	0.35	2.1
	#820	2.43	2.1
	#821	2.11	2.1
Fig's 3a-d	#824	2.13	2.1
	#826	1.82	2.1

(IC-75-4):

- Original traces manually smoothed, 150 sec sampling interval
- Uniform weighting, points < 2 kR 3914 Å omitted

(Others):

- 15 sec sampling interval on 35 sec pre-integrated data
  (except 76-10 and #826, 1 min sampling;
  #821, $2\frac{1}{2}$ sec pre-integrated data)

- Uniform and proportional weighting, all data points included

- Fraction of NO $\Delta v = 2$ sequence in radio-meter FWHM   0.56 (IC-75-4)
  0.46 (Others)

- Atmospheric transmission to NO $\Delta v = 2$ in-band   0.75 (IC-75-4)
  0.965 (Others)

- COCHISE population, Billingsley cascade, no collisional quenching of $NO^{\ddagger}$

- 20.5 ion pairs/3914 Å photon (120 km mean energy deposition altitude), 34 eV/ion pair

400

320

240

2.94μm (OH Corrected), kR

160

80

0

UNIFORM

PROPORTIONAL

#820 27 Aug 78
TIME, UT 1003-1057

	UNIFORM	PROPORTIONAL
SLOPE	5.17	5.16
INTERCEPT	0.38	8.91
CORRELATION COEFFICIENT	0.91	0.96
EFFICIENCY %	0.71±0.04	0.70±0.02

3914Å, kR

20   40   60   80   100

3(a)
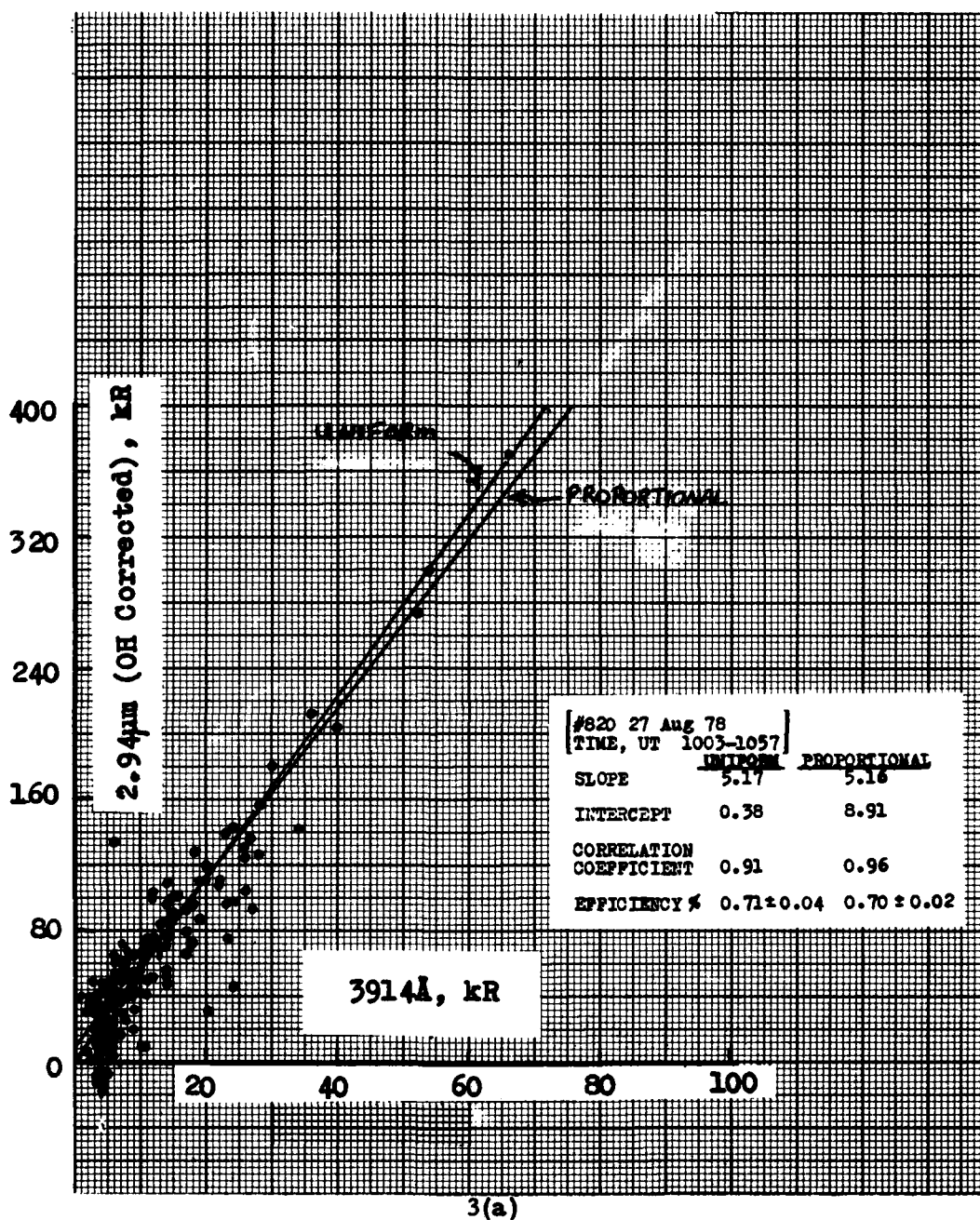
Figure 3a-d.   Scatter plots of 2.828-3.041 μm and 3914Å-band
zenith intensities for four data flights in September
1978. Uniformly- and proportionally-weighted
least-squares fits of the SWIR intensities corrected
using the measured hydroxyl-band ratios are shown.
These results are summarized in Table 2.

19

800

600

2.94μm (OH Corrected), kR

400

200

0

#821 28 Aug 78
TIME, UT 1025-1033

	UNIFORM	PROPORTIONAL
SLOPE	4.74	5.06
INTERCEPT	-26.8	-36.3
CORRELATION COEFFICIENT	0.96	0.95
EFFICIENCY ∮	0.65±0.04	0.69±0.05

PROPORTIONAL

UNIFORM

3914Å, kR

20   40   60   80   100   120   140

3(b)

3(c)

2.94μm (OH Corrected), kR

UNIFORM PROPORTIONAL

80

60

#826 07 Sep 78
TIME, UT 0930-1125

	UNIFORM	PROPORTIONAL
SLOPE	6.47	5.69
INTERCEPT	0.35	9.50
CORRELATION COEFFICIENT	0.78	0.82
EFFICIENCY	≤0.88±0.12	0.78±0.09

40

3914Å, kR

20

0

20   40   60

-20

3(d)

22

Table 2. Summary of results of SWIR yield measurements

Mission Date	Time	Chemiluminous Efficiency (%)			Correlation Coefficient[*]
		Uniform Weighting	Proportional Weighting	Recalibrated[+]	
IC-75-4 10 Mar 75	0805-0930 1120-1215	0.45 ± 0.09	(150 sec sampling, manual smoothing)		0.80
	0930-1120	0.60 ± 0.12			0.88
IC-76-6 03 Mar 76	0500-0528	0.46 ± 0.02	0.41 ± 0.02	0.42	0.95
IC-76-9 07 Mar 76	0922-0928	0.45 ± 0.10	0.33 ± 0.09	0.38	0.86
	0950-1030	0.44 ± 0.03	0.47 ± 0.02	0.42	0.92
	1134-1145	0.46 ± 0.02	0.46 ± 0.02	0.42	0.98
IC-76-10 08 Mar 76	0740-0845	0.46 ± 0.02	0.43 ± 0.02	0.45	0.98
	0850-0925	0.47 ± 0.05	0.41 ± 0.03	0.46	0.94
IC-76-16 26 Mar 76	0906-0931	0.46 ± 0.04	0.42 ± 0.04	0.29	0.88
	1013-1055	0.66 ± 0.03	0.63 ± 0.02	0.42	0.94
	1120-1159	0.50 ± 0.02[++] (0.50±0.02)	0.46 ± 0.02	0.28	0.97
720 11 Sep 77	0436-0529	0.56 ± 0.06	0.53 ± 0.05	0.67	0.81
	0820-0856	0.43 ± 0.06	0.33 ± 0.05	0.52	0.73
	0911-0925	0.35 ± 0.04[++] (0.40±0.02)	0.33 ± 0.05	0.42	0.88
724 15 Sep 77	0905-1000	0.18 ± 0.04	0.16 ± 0.03	0.72	0.58
725 16 Sep 77	0945-1005	0.38 ± 0.05	0.35 ± 0.03	1.27	0.84
820 27 Aug 78	1003-1057	0.71 ± 0.04	0.70 ± 0.02	0.72	0.91
821 28 Aug 78	1025-1038	0.65 ± 0.04	0.69 ± 0.05	0.68	0.96
824 02 Sep 78	1115-1200	0.58 ± 0.04	0.53 ± 0.03	0.60	0.90
826 07 Sep 78	0930-1125	0.88 ± 0.12	0.78 ± 0.09	1.47	0.78

[+]Quiet radiometer renormalized to 100 kR OH $\Delta v = 1$, uniform weighting.

[++]All data points included in the fit.

[*]With uniform weighting.

These rocket data show that the SWIR volume emission rate per eV/sec input depends on altitude, and therefore presumably on the upper atmosphere's oxygen-atom concentrations. Thus the variability in vertical-column yield may be an effect of changes in the profile of [O].

The extent to which the chemiluminous yields depend on the distribution of altitudes at which energy is deposited has not yet been fully investigated. A preliminary assessment for long ($\geq \frac{1}{2}$ hr) segments of the 1976-77 missions (Ref 1) showed no systematic correlation; however, since the relatively long period covered by most of the cross-plots usually includes a wide range of auroral brightnesses and peak deposition altitudes, this result is not conclusive. (On the other hand lack of detectable curvature in the scatter plots tends to support the preliminary findings.) Efficiencies inferred from shorter data periods in which the energy spectrum of the incoming auroral electrons holds more nearly constant may provide further information on this issue. Altitudes for the 1978 flight series are currently being determined from the ratios of intensities of the 6300 $\overset{o}{A}$ OI and 4278 $\overset{o}{A}$ N_2^+ features measured in flight (Appendix II of Ref 5).

PRELIMINARY RESULTS FROM THE NARROW-FIELD
RADIOMETER AND PHOTOMETER

The 0.4°-field, 13° forward-tilted instruments became available in April 1979. The initial chart records from flights of this high-resolution system in eastern Canada clearly show that the SWIR radiance enhancements are correlated with the particle energy input to within a few sec in time and a few km in space.

Fig 4 shows some examples of raw data from arc forms and pulsating aurora. The only processing of the radiometer's output is integration with the instrument's ~ 0.2 sec time constant (the recorder pen's response time is also of this order). Final radiance calibration is not yet available. The photometer pen's deflection is nonlinear in column energy input, as it has break-points at which the slope of

MAY 2, MISSION 911A
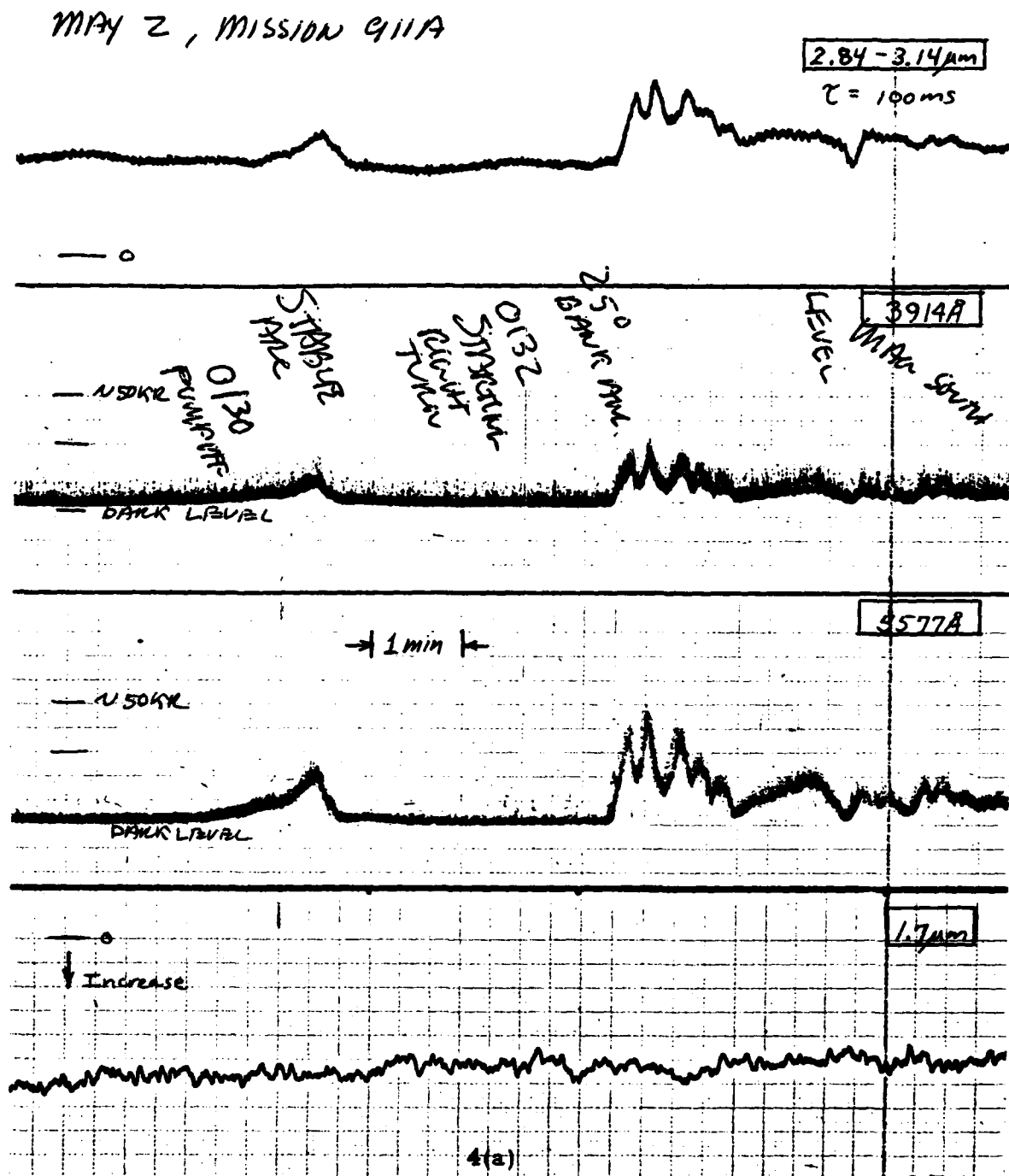
Figure 4a-d. Strip chart records from flights of the narrow-field aircraft instruments. Final radiometric calibrations are not yet available.

APRIL 27, MISSION 909A   APRIL 25ᶻ, MISSION 908A
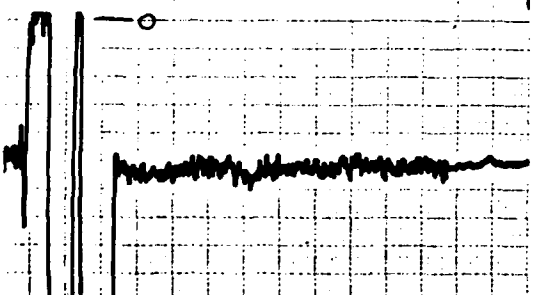
2·84 - 3.14μm
200ms FS
G=1
7=100ms

Ⓑ

—0

0225ᶻ

— ~50KR

— —DARK LEVEL

3914 A°
G=6

Tulewin
South

Roll Kc
out 0639

Ⓐ

— ~50KR

— DARK LEVEL

5577 A°
G=3.4

—o

1.7μm

4(b)

26

APRIL 25 Z, MISSION 908A

2.84-3.14μm

3914A

PUMP 0429 IN

ENTERING WINDOW DUE TO INCREASE WHITE LINE

PULSATING AURORA

5577A

DARK LEVEL

1.7μm

4(c)

27

17 Sep Z

2.84 - 3.14μm

D

3

—0

AURORA

PUMP OFF
T3 = -75

3914Å

5577Å

SOLAR DEPRESSION
9.4°

1.7μm
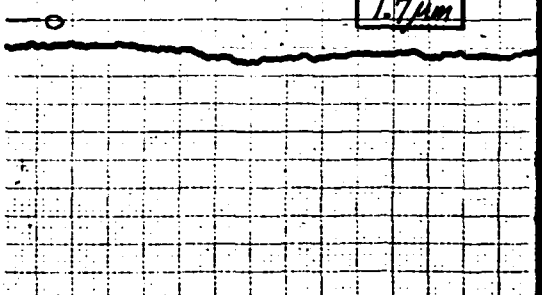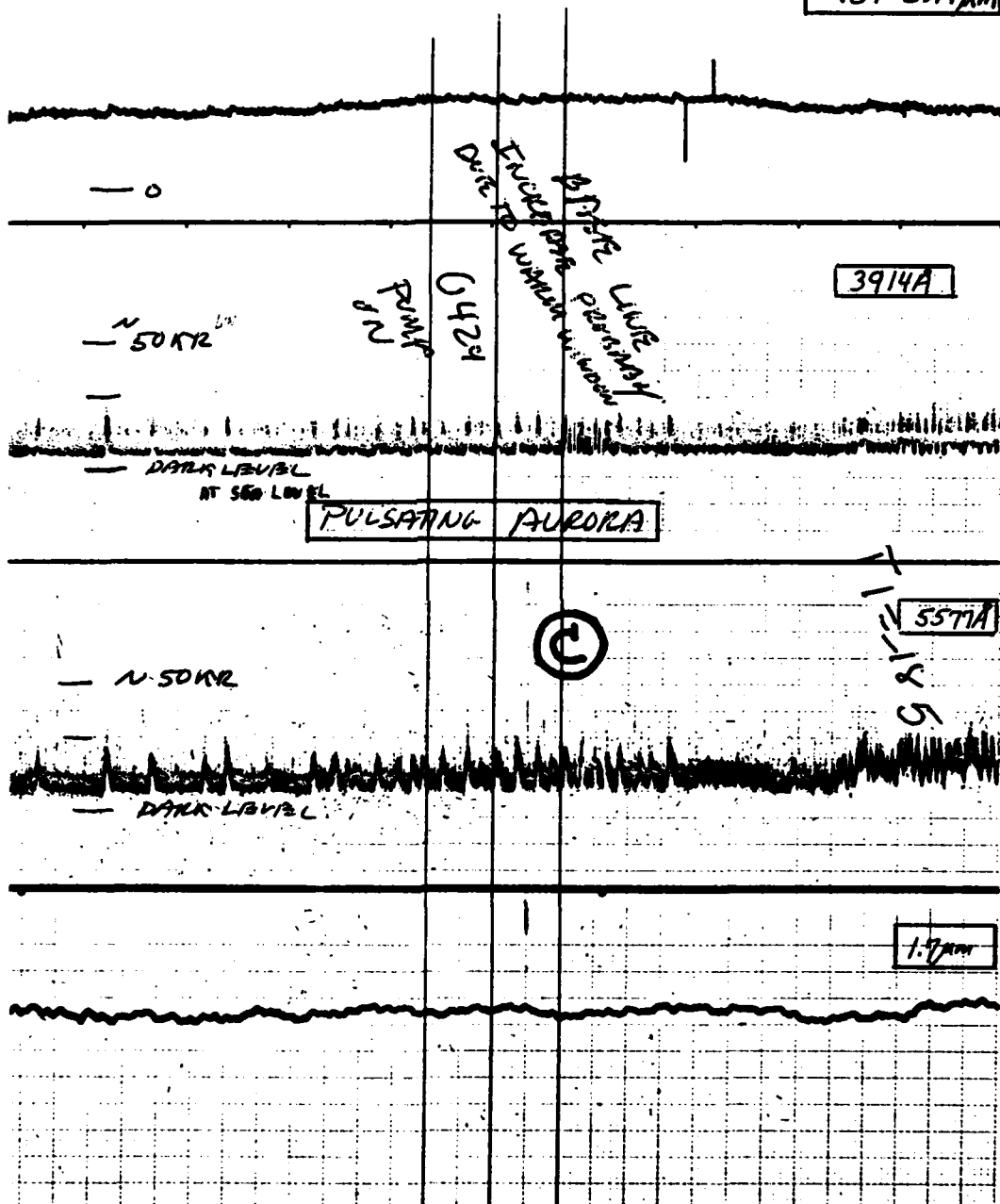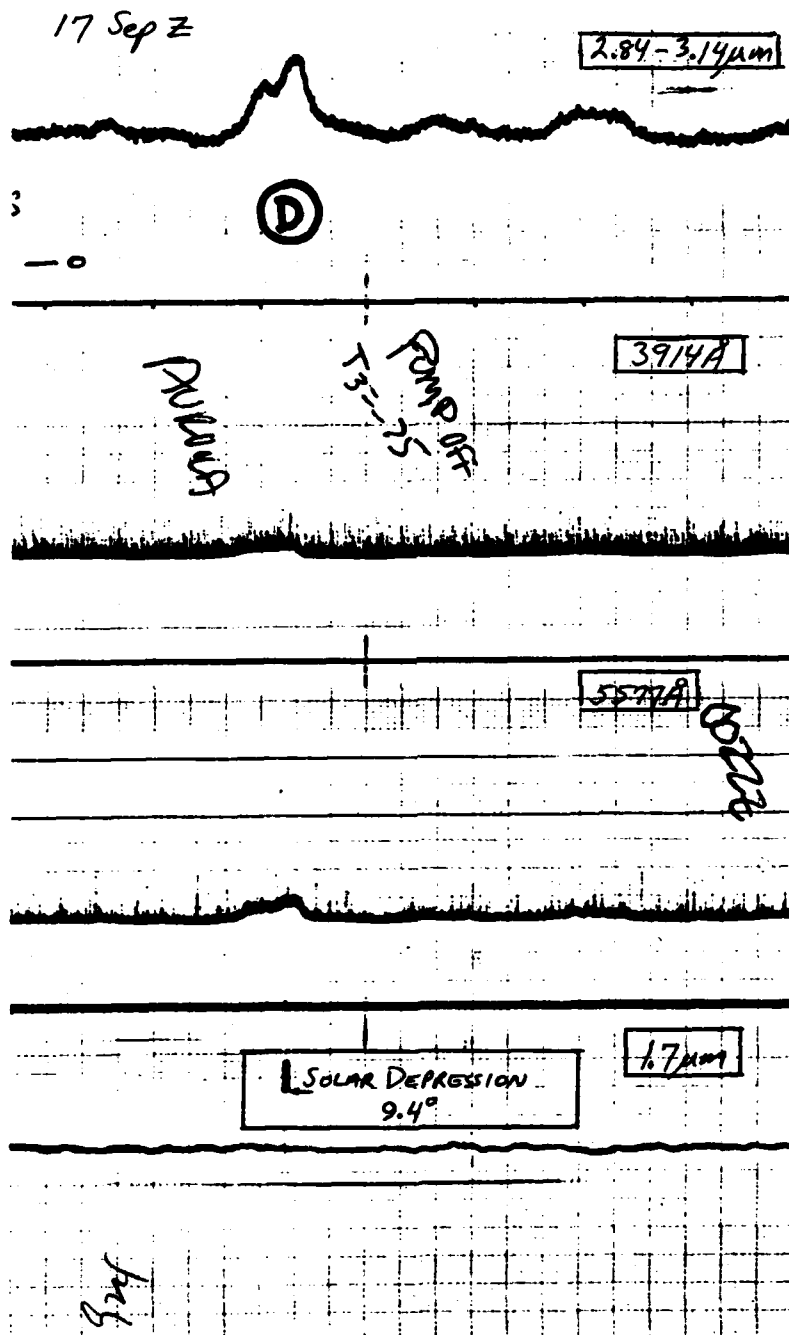
4(d)

the input-output characteristic decreases to increase the dynamic
range of auroral bombardment intensities that can be read out in
flight. The very narrow spikes on the photometer traces are
thought to be due to electrons released near the photomultiplier tube's
first dynode by cosmic rays, as the trace is much quieter when the
instrument is operated at sea level (where the cosmic ray flux is an
order of magnitude less than at flight altitude).

Initial examination of the traces at the scale in Fig 4 shows that
the rise and fall times of the 2.9μm radiometer signal are within
5 sec of the corresponding characteristic times of their accompanying
3914 $\mathring{A}$ and 5577 $\mathring{A}$ signals. (5 sec is 1$\frac{1}{4}$ mm advance of the chart paper.)
Note, for example, the very rapid falloff in the arc (B) at the right of
Fig 4b; and that each of the auroral pulsations (C) (Fig 4c), which
have duration about 4 sec and mean amplitude 15 kR 3914 $\mathring{A}$, is closely
followed in the SWIR trace. In addition no visible-infrared offset
greater than 5 sec can be resolved in the original aircraft records.

We attempted to improve this estimate of correlation by photo-
graphically enlarging the as-received traces and smoothing them
manually. This somewhat empty magnification procedure — most of
the noise as well as the signal is amplified —, applied to the complex
arc system (A) at the left of Fig 4b, indicated that the 10-to-90% rise
and fall times of the visible fluorescence and SWIR emission are
within 3 sec of one another. The results for the pulsating aurora (C)
suggested that the SWIR fall time is 1 or 2 sec longer, but as the
apparent "contrast" in the traces depends, often critically, on the
selection of background levels this preliminary figure cannot be taken
too seriously.

As these data are available on magnetic tape for digitization,
calibration and conversion to scene brightness, subtraction of back-
grounds, and averaging-weighting by computer, no further manual
processing of the chart records was attempted. Their assessment
also requires information on the particle input's temporal and spatial

29

variations provided by the video camera (as described in Appendix
I of Ref 1).

Attention is directed to a small segment of the twilight record
during which intense particle precipitation was overhead, (D) in
Fig 4d. (As is noted in Section 5, auroral activity was weak during
most of the measurements on the sunlit upper atmosphere.) In
contrast to the behavior seen in the other (nighttime)traces, the decay
time of the SWIR pulse is considerably longer than that of the air
fluorescence pulses. The apparent delay may, however, be an
artefact of the compressed and possibly nonlinear scale of the 3914 Å
and 5577 Å strip chard record. Clearly, the original pen deflections
must be converted to quantitative sky radiances for effective evaluation
of these daytime SWIR structure-yield data.

DISCUSSION

The results from a total of some 16 hr of moderate-resolution
measurements from jet aircraft altitude of SWIR emission from
auroral particle-bombarded air show statistically significant segment-
to-segment variations of about a factor two in "equilibrium" chemi-
luminous yield; these are not yet satisfactorily explained. One
potential mechanism is variability in the altitude profile of concen-
tration of oxygen atoms, which collisionally quench vibrationally-
excited nitric oxide (Section 3) and have other effects on the chain of
aeronomic reactions (Section 5). The mean energy efficiency, $\frac{1}{2}\%$
if the radiation is the NO overtone, is consistent with the altitude-
averaged value measured from rockets, and that inferred from
laboratory data.

Preliminary results from the high-resolution ($\sim$1 km-field),
high-sensitivity radiometer and photometer show the SWIR column
emission to be correlated with air fluorescence to at least 5 sec
both when the particle precipitation is pulsating and when arc forms
are scanned by the aircraft's forward motion. Following further

30

computer reduction of these otherwise-unprocessed flight data, the
procedures developed in Appendix I of Ref 1 for deriving SWIR grow-
in and decay time constants and determining input-output relationships —
and thus verifying code models — can be applied. This new finding
indicates that the aerochemical reactions that excite the 2.9μm-band
output "follow" the initial energy input to within a few sec, or a few
km spatially. The spatial and temporal variability of the SWIR sky
background produced by ionizing radiations from atmospheric nuclear
explosions would therefore reflect closely that of the visible air
fluorescence, on which extensive photographic data are available.

SECTION 2

ENERGY INPUT IN HIRIS II's FIELD

INTRODUCTION

We calculate here rates of particle-energy input within HIRIS II's field of view during six further spectrum scans, using the procedure outlined in Section 2 of Ref 1 . As was previously described (Section V of Ref 6), the rocket (IC 630.02-1A) lost vertical attitude stabilization and tumbled about a southeast-northwest axis at $\sim 10\frac{1}{2}^{\circ}$/sec, which resulted in large variations in power input while individual interferograms were being compiled. Specifically, the axially mounted instrument's elevation angle changed by as much as 14° during the 1.26-sec mirror scans, making the field's intercept sweep across the distant excited volumes by tens of kilometers in altitude (as can be seen in Fig 5).

We applied the meridian scanning photometer data and all-sky photographs taken at the Poker Flat (Ref's 7 and 8) and Fort Yukon ground stations (Ref 8) to determine the spatial distributions of power input into the upper atmosphere. Ionospheric electron concentrations measured by the DNA 617 incoherent-scatter radar were in some cases used to correct the apparent auroral surface radiances for out- and inscattering by the lower atmosphere. Model volume emission rate profiles, based on the altitudes of peak energy deposition (Ref 9) measured by triangulation, were derived for each particle-precipitation region. An example, which shows typical horizontal extents of the glows, is given in Fig 13 of Ref 1 . Column integrals were then summed along the instrument's line-of-sight.

SCANS 35, 61, 74, 86, 112, 150

Figure 5 shows the el and az of HIRIS II's optic axis at the beginning and end of the 12 scans for which column inputs have so far been calculated. The input data support infrared spectra taken

GROUND RANGE NORTH OF PKR , km

Figure 5. Pointing of the HIRIS II (1C630.02-1A)spectrometer's optic axis at the beginning and end of the 12 scans for which column input rates have been derived. Scans marked † are reported here, * in HAES 79 (Ref 1). The rocket's trajectory is projected into the meridian plane through PKR. Its altitudes during three meridian photometer scans from PKR (these start pointing toward the N) are indicated.

Table 3. Summary of HIRIS II's pointing geometry and average power input within the field in half-scans

SCAN	TIME, sec START	END	ALTITUDE, km START	END	ELEVATION, ° START	END	AZ (MAG), ° START	END	AVERAGE POWER INPUT, kR 3914Å 1st half	2nd half
M 23⊗	100.9	102.1	96.3	97.2	0.1	13.6	36.9	34.8		
N 24*	102.2	103.4	97.3	98.2	14.1	27.9	34.9	32.9	25	9
S 35†	117.0	118.3	107.0	107.7	11.7	-1.1	211.1	208.9	206	214
M 48⊗	134.6	135.9	115.9	116.4	-8.9	4.7	39.0	36.1		
S 61†	152.2	153.5	121.8	122.1	4.8	-8.4	211.2	208.9	237	261
N 74†	169.7	171.0	124.9	125.0	-3.4	10.6	38.6	35.4	87	65
S 86†	185.9	187.1	125.1	125.0	12.9	-0.2	213.6	210.9	64	214
M 99⊗	203.5	204.8	122.6	122.3	-10.2	3.5	40.6	37.6		
S 112†	221.0	222.3	117.2	116.7	6.8	-7.0	214.9	231.8	516	365
M 125*	238.5	239.8	108.9	108.2	-6.2	8.0	40.3	37.0	79	109
S 137*	254.7	256.0	98.6	97.7	15.2	1.5	218.2	215.2	46	108
N 150†	272.3	273.6	84.6	83.5	-12.2	2.9	42.2	38.4	0+	14

⊗ Not Completed
* Reported in Ref 1
† Reported here
+ Pointing below aurora

34

near the atmosphere's limb (as requested by AFGL), where the van Rhijn path length gain resulted in significant increases in IR signal/noise ratios (Ref 10). Five double-sided spectrums were taken with the instrument pointing generally SW, where most of the simultaneous and previous dosing took place (these are labeled with an S after the scan number), and seven (labeled N) pointing NE toward considerably weaker particle precipitation; refer to Fig 5 . (Rotation of the rocket axis is counterclockwise in Fig 5's projection). Table 3 presents the viewing geometry and the calculated power input in each half-scan. Since the rocket's altitude changed by $\lesssim$ 1.1 km during all of Fig 5's interferometer scans (<0.2 km in some), we have made the approximation that the instrument's altitude remains constant during each scan.

All-sky images of the visible radiance distributions at Poker Flat and Fort Yukon when the rocket's altitude was between 107 km on upleg and 84 km on downleg are in Fig 6. Three of the six spatial distributions shown are assessed here. The dark (curved) solid line drawn on each frame is a projection onto the film plane of the instrument's line-of-sight at the mid-point of the scan interval. Eℓ and az from the camera site at which the instrument's optic axis intercepts altitudes along the trajectory is marked as a white dot.

The results of the calculations – apparent time dependence of 3914 Å-band column emission rate from individual regions before correction for scattering by the atmosphere, and sums along lines-of-sight after correction – are plotted in Fig 7. The corrected sums are intercompared in Fig 9. Particulars of the data assessment for each of the six interferometer scans are as follows.

Scan 35S (107.4 km mean rocket altitude)

Most of the energy deposition during this spectrum scan is in the narrow ($\sim$ 25 km wide) intense arc centered $\sim$ 5° south of the Poker Flat zenith (see Fig 6). The altitude of maximum deposition

[PKR]

185.9 – 187.1
125.1 – 125.0
12.9 – –0.2
213.6 – 210.9

86   179

[FYU]

272.3 – 273.6
84.6 – 83.5
–12.2 – 2.9
42.2 – 38.4

150

[FYU]

134.6 – 135.9
115.9 – 116.4
–8.9 – 4.7
39.0 – 36.1

48

[PKR]

254.7 – 256.0
98.6 – 97.7
15.2 – 1.5
218.2 – 215.2

137   171

[PKR]

117.0 – 118.3
107.0 – 107.7
11.7 – –1.1
211.1 – 208.9

S-35

[FYU]

203.5 – 204.8
122.6 – 122.3
–10.2 – 3.5
40.6 – 37.6

99

Mag N
W — S — E

HIRIS II

SCAN INTERVAL, sec
ROCKET ALTITUDE, km
INSTRUMENT El°
INSTRUMENT Az° (Mag)
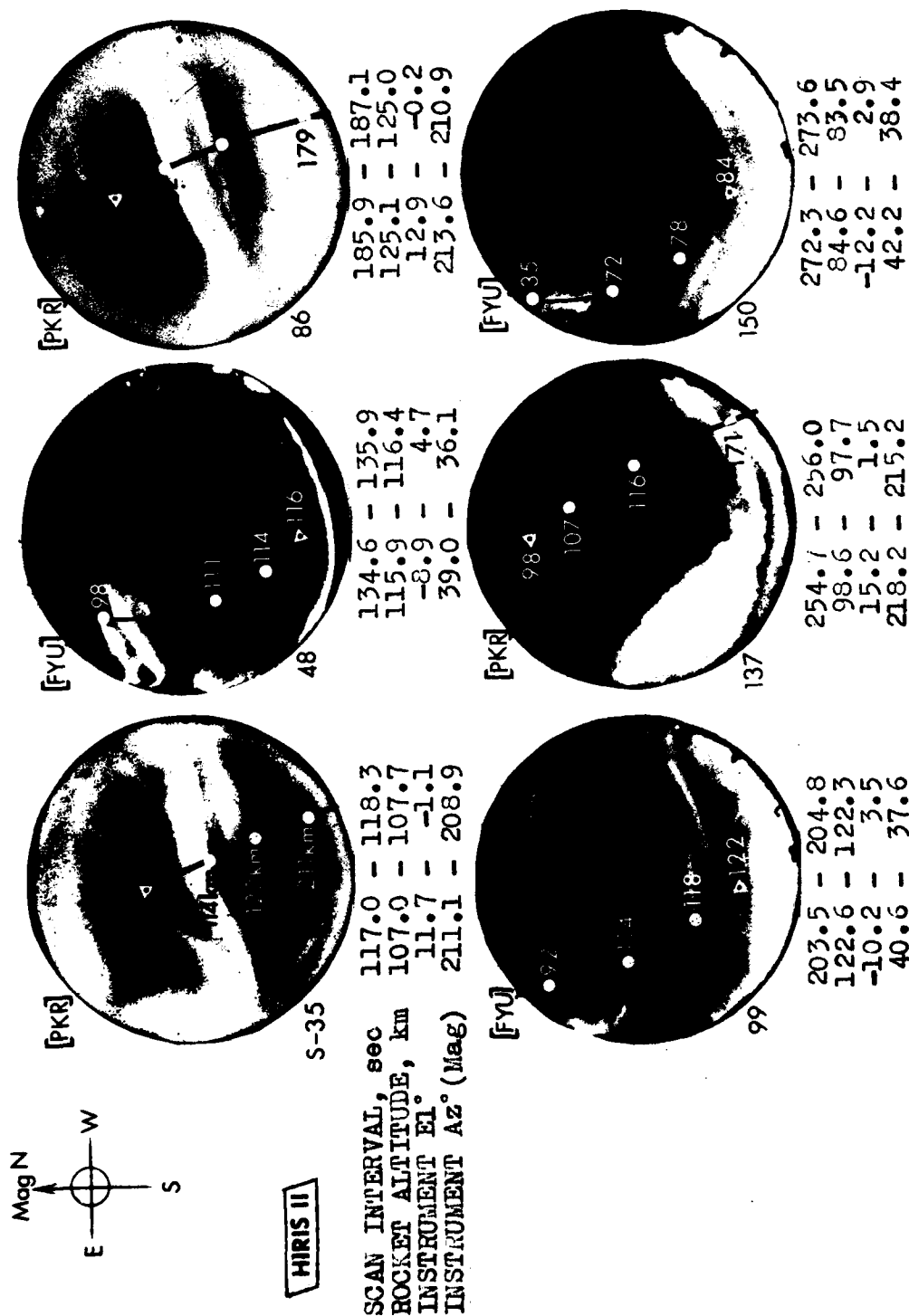
Figure 6. Auroral radiance distributions during six HIRIS II interferometer scans (all-sky images from PKR and FYU), with projections onto the film plane of the instrument's line-of-sight at the midpoint of each scan interval. The white dots indicate the altitudes at which the optic axis intercepts the direction vectors from the camera stations at PKR (shown for scans during which the instrument was pointing SW) or FYU (instrument pointing NE). (The lines of sight curve on all-sky projections.)

36
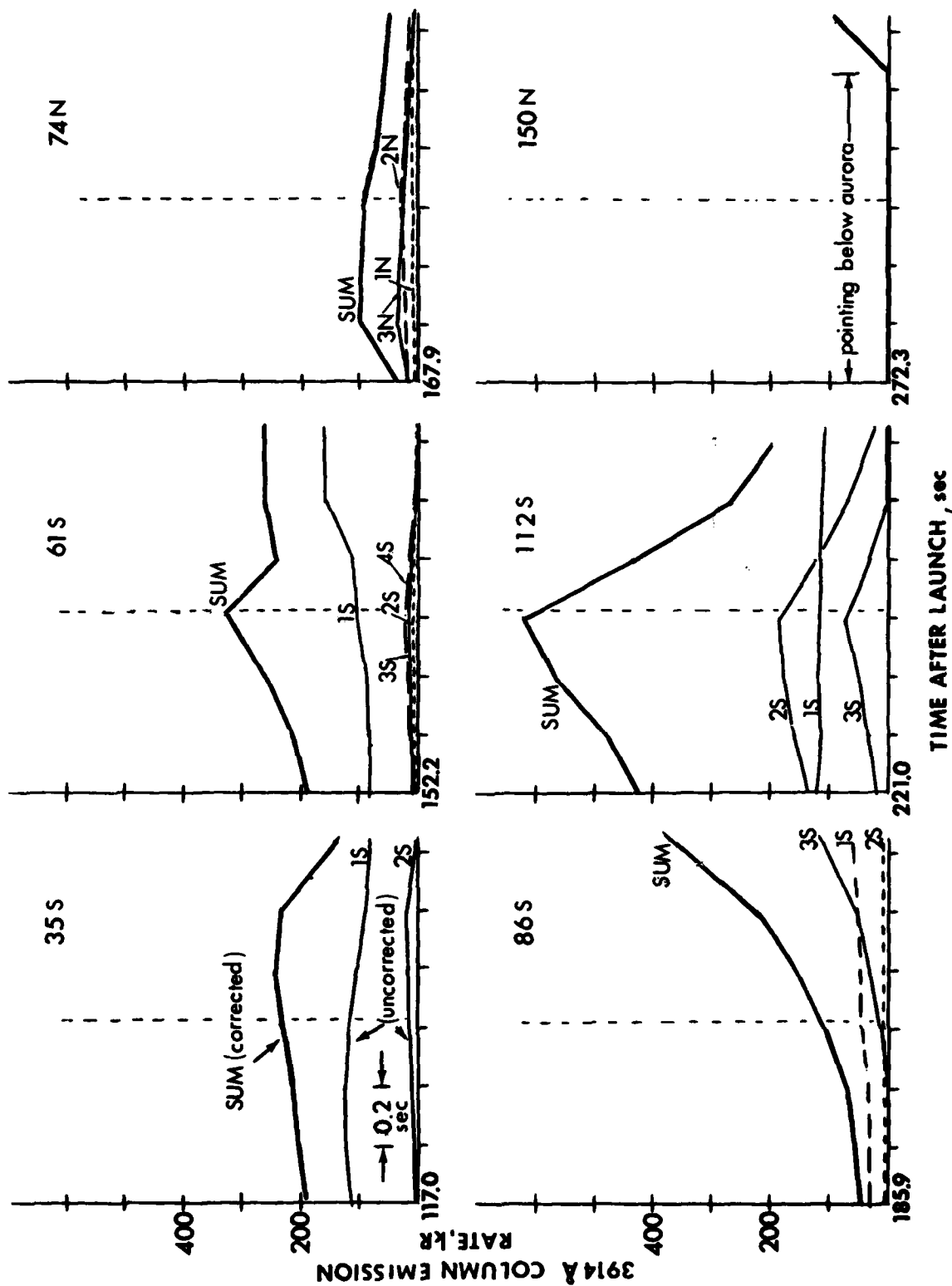
Figure 7. Power inputs from auroral regions within HIRIS II's field before correction for scattering by the lower atmosphere, and summed after correction. The symbols 1S, 2S, ..., etc. represent individual emitting volumes such as those shown in Fig 13 of Ref 1.

rate, determined by triangulation from the two-station meridian photometer data, is 115 km. This peak altitude would result from a Maxwellian incoming-electron spectrum having a characteristic energy α about 3 keV (Ref 9). Using the procedure in Ref 1 and taking the arc as uniform in the E-W direction (so that the meridian photometer data apply to HIRIS's field), the maximum 3914 Å volume emission rate was found to be 4×10^4 photons/cm^3-sec. (No correction for scattering by the lower atmosphere has been applied up to this point).

A second and much weaker arc far to the south of PKR (at ~75° zenith angle) lies too near the FYU horizon to permit effective triangulation. As its apparent intensity was substantially less than that of the arc near the zenith, its peak-emission altitude was taken as 122 km ($\alpha = 1.9$ keV, maximum 3914 Å volume emission rate 1.6×10^3 photons/cm^3-sec). Earth curvature increases the intercept altitudes on this south-lying arc by some 12 km. Altitude profiles were as usual taken as uniform across the N-S "width" of each of the two arc regions. A weak, diffuse glow between the two arcs (< 7 kR maximum 3914 Å from PKR, some of which is due to atmospheric scattering) was neglected.

The contributions from the two regions before correction for light scattering and attenuation are shown in Fig 7. Following Ref 1, we adopt narrow-beam 3914 Å transmissions through the clear winter model atmosphere of 0.53 per air mass, or 0.53 and 0.12. Buildup of inscattered photons in the directions of the two excited air volumes has the effect of increasing the atmosphere's transmission; following our previous model (outlined in Section V of Ref 5, applied to other HIRIS II data in Section 2 of Ref 1), we estimate effective transmissions of 0.60 and 0.20 respectively.

The total corrected power input is shown by the curve marked SUM in Fig 7. Since the major fraction comes from the near-zenith arc, accuracy is limited primarily by the inherent uncertainties

in lateral uniformity of the energy deposition profile assigned to this region (and only secondarily to errors in buildup corrections). As the horizontal separation between rocket and arc is small ($\sim$ 50 km), errors in altitudes at which the field intercepts the emitting volume are expected to be small. The expected uncertainty in energy input rates is therefore + 50%, -40%.

Scan 61S (122.0 km)

Four regions contribute power input. The bright arc of Scan 35 remained just S of the PKR zenith, a second, weaker arc formed 20°S of PKR, and the region near the southern horizon split in two and increased in intensity. The sky brightness distribution at the time of Scan 61 is similar to that shown for Scan 86 in Fig 6 and for 164 sec in Fig 58 of Ref 5 .

Peak altitudes in the two arcs near the PKR zenith were determined by triangulation (using Ref 7's elevation-scanning photometer data only), and altitudes of the two emitting regions far to the south were estimated on the basis of their relative uncorrected radiances. Altitudes and characteristic primary electron energies are 107 km - 5. 5 keV for the arc 6° S of PKR zenith, and 120 km - 2 keV for the other three regions. Peak (uncorrected) 4278 $\overset{\circ}{A}$-band volume emission rates are 2.2×10^4, 7.3×10^2, 5.5×10^2, and 4.7×10^2 photons/cm^3 -sec. (N_2^+ 3914 $\overset{\circ}{A}$ -band emission is a factor 2.9 higher.) Thus the bright arc just south of PKR is again the major contributor to the energy deposition within the instrument's field (see Fig 7).

The narrow-beam 4278 $\overset{\circ}{A}$ photon transmissions from the four auroral regions are 0. 57, 0. 55, 0. 26, and 0. 12. Estimating buildup as described earlier, the effective transmissions become 0. 65, 0. 65, 0. 30, and 0. 25. As the power input is again dominated by the near-zenith arc ($\sim$ 65 km horizontally from the northward-moving rocket) we estimate the uncertainty in the total shown in Fig 7 to be + 50% - 40%.

Scan 86S (125.0 km)

By this time the particle precipitation distribution south of
Poker Flat has evolved into three arcs; refer to the all-sky view in
Fig 6 . The pointing geometry is similar to that for Scan 137
(Section 2 of Ref 1), in that the instrument field makes a near-
vertical sweep into the peak in the deposition altitude profile. The
change in elevation angle from 12.9° to -0.2° results in a very rapidly
increasing column emission rate toward the end of the spectrum scan,
with the average power input during the second half more than three
times that of the second half (as shown in Table 3).

Altitudes of peak energy deposition and characteristic particle
energies are 110 km - 4.0 keV, 118 km - 2.5 keV, and 112 km - 3.7 keV
for the arcs at 5° (1S), 37° (2S), and 60° (3S) zenith angle. We applied
3914 Å photon transmissions of 0.58, 0.66, and 0.56, corrected for
buildup, to get the total power input shown in Fig 7 . Since regions
1S and 3S contribute about equally to the sum, its uncertainty is
expected to be dominated by the error in buildup in 3S and (secondarily)
by errors in lateral uniformity assigned to 3S and 1S. The estimated
error in total power input is +65%, -50%.

Scan 112S (117.0 km)

At this time (221 sec after launch) the visible-auroral distribution
was changing rapidly; a representative view is Fig 5 of Ref 1 , ~20
sec after the scan was completed. The rocket is penetrating an intense
narrow arc at an altitude very close to the maximum in energy deposi-
tion. The ground-based photometers and cameras show this arc
(1S in Fig 7) forming and then disappearing near 36° zenith angle
north of PKR in a span of about 40 sec. Its peak deposition altitude
is 110 km. Two other broad arcs south of PKR, at 120 km (12°, 2S)
and 122 km (assumed; 66°, 3S) were also viewed from near co-altitude
during this spectrum scan. 4278 Å wide-beam transmissions applied
were 0.65 - 1S, 0.65 - 2S, 0.40 - 3S.

Long viewing path lengths through regions 2S and 3S resulted
in higher column inputs during scan 112 than in the eight other limb-
viewing scans in Table 3 . The uncertainty arises principally from
errors in buildup in diffuse regions 2S and 3S as well as (again) in the
widths of these regions; we estimate it as + 75%, - 50%.

Scan 74 N (125. 0 km)

During this scan the instrument was pointing NW towards much
weaker particle precipitation than in the previously-discussed four
scans in the SE.   The all-sky projection for scan 74 is qualitatively
similar to those for scans 48 and 99 in Fig 7 (see also Fig 58 of Ref 5).
These show that the volume in HIRIS II's field does not overlap the
volume in the meridian photometers' fields and that the sky brightnesses
are not uniform in the east-west direction.

The radiances and altitude profiles in the direction of the infrared
measurements can, however, be estimated with the aid of an equi-
density contour plot made from the Fort Yukon all-sky frame at 169 sec
(Fig 8). The two-dimensional sky brightness distribution was calibrated
using the 1-D 4278 $\overset{o}{A}$ photometer cut through the meridian from FYU.
Corrections to the absolute brightnesses for vignetting by the all-sky
camera lens and for scattering of photons by the lower atmosphere,
which are not shown in Fig 8 , were applied later.

Peak deposition altitudes of three emitting regions were then
estimated on the basis of their relative brightnesses in the projection
to FYU. Following the argument in Section 2 of Ref 1 , two diffuse
regions at 15° north and 30° south zenith angle (from FYU)were
assigned peak altitudes of 135 km ($\alpha = 1.4$ keV) and a third brighter
region (3 N, $42\frac{1}{2}^{o}$ north) an altitude of 120 km ($\alpha = 2$ keV). The re-
sulting contributions from each emitting volume in Fig 7 are adjusted
for lens vignetting and increased by 50%, the adjustment that has been
applied to all Fort Yukon photometer data to normalize them to those
from Poker Flat (see Section 2 of Ref 1 , p 50).
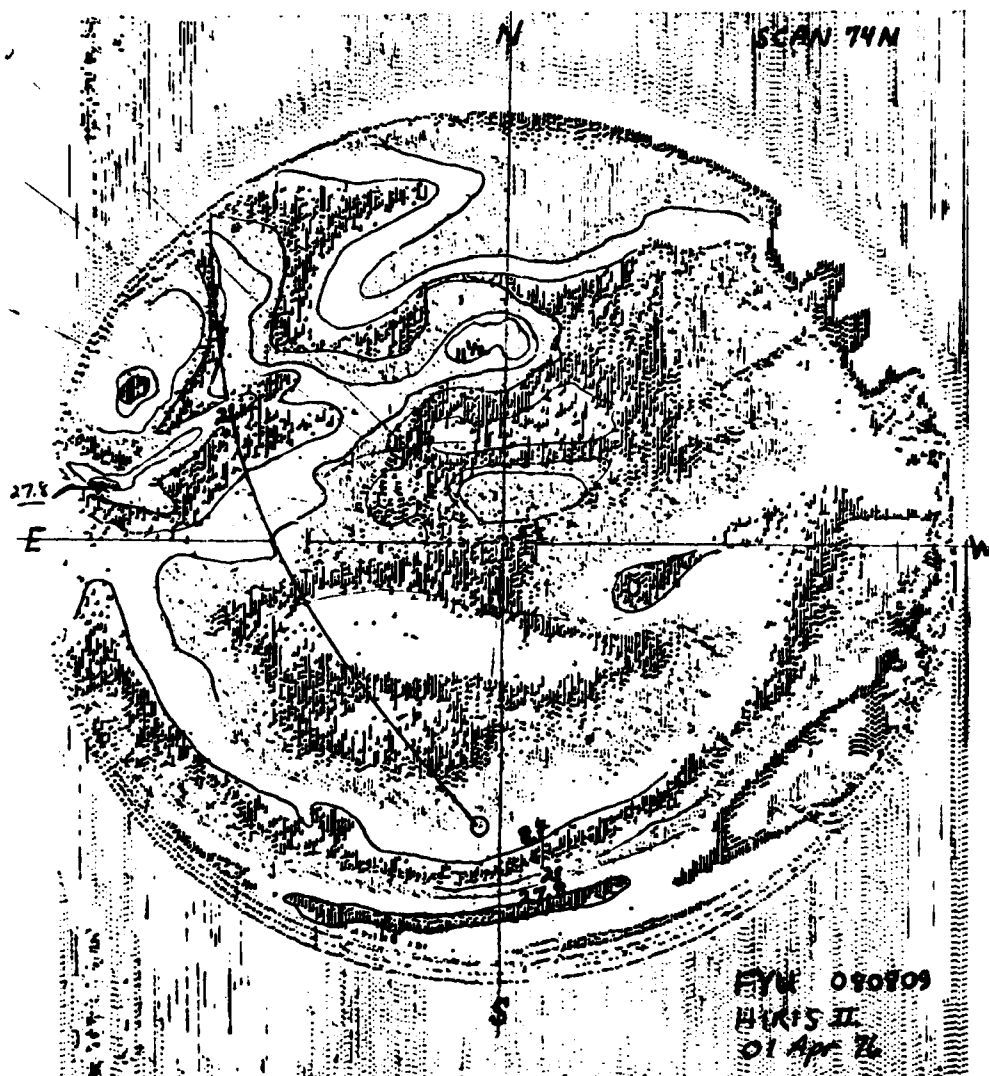
Figure 8. Equi-density contour plot from the FYU all-sky frame at
169 sec after launch of HIRIS II. Absolute auroral bright-
nesses in units (2.9 x N_2^+ 4278 Å) kR were assigned to the
contours using the FYU meridian photometer data, without
correction away from the meridian for vignetting by the lens
(10% at $40°$ zenith angle, 20% at $60°$) or atmospheric scatter-
ing. These corrections were applied in the final calculation
of column intensities in Fig 7.

The 4278 Å transmissions after buildup is taken into account are 0.61, 0.70 and 0.65. The error in the total power input in Fig 7 is expected to be greater than that for the previous four scans because of the uncertainty in altitudes of peak energy deposition and in scaling intensities from the all-sky photographs, and the larger correction for buildup in the direction of weaker, more distant emitting regions. A reasonable estimate of error in the scan 74 inputs is + 85%, - 60%.

Scan 150 N (84.0 km)

The all-sky photographs and meridian photometer data show that the sky brightness distribution changed slowly after about 250 sec (refer to Fig 58 of Ref 5). We therefore applied to scan 150 (273 sec) the emission rate profiles derived in Ref 1 for scan 125, 34 sec earlier. This simplification is further justified by the fact that little particle-energy input is present during the first half of the scan, as the instruments points between 12.2° and 4.7° below the local horizontal from 84 km altitude. (The earth's curvature would, however, allow auroral excitation several hundreds of km to the north to come into the field when the depression angle is less than 9°; such excitation is for all practical purposes not measurable from the ground station.) Later as the rocket's elevation angle increases above about $+1^\circ$, the northern-most arc in the photographs, at ~ 185 km horizontal range (3 N in Fig 13 of Ref 1), comes into view. The total 3914 Å-band column emission rate, calculated applying the corrections from scan 125 derived in Ref 1, is in Fig 7. The average power inputs (Table 3) should be considered lower limits since precipitation far north of FYU may be contributing.

COMMENTS

Figure 9 summarizes the total 3914 Å column emission rates (corrected for scattering) within HIRIS II's field during the six near limb-viewing scans. As previously noted, the strong variation with

43
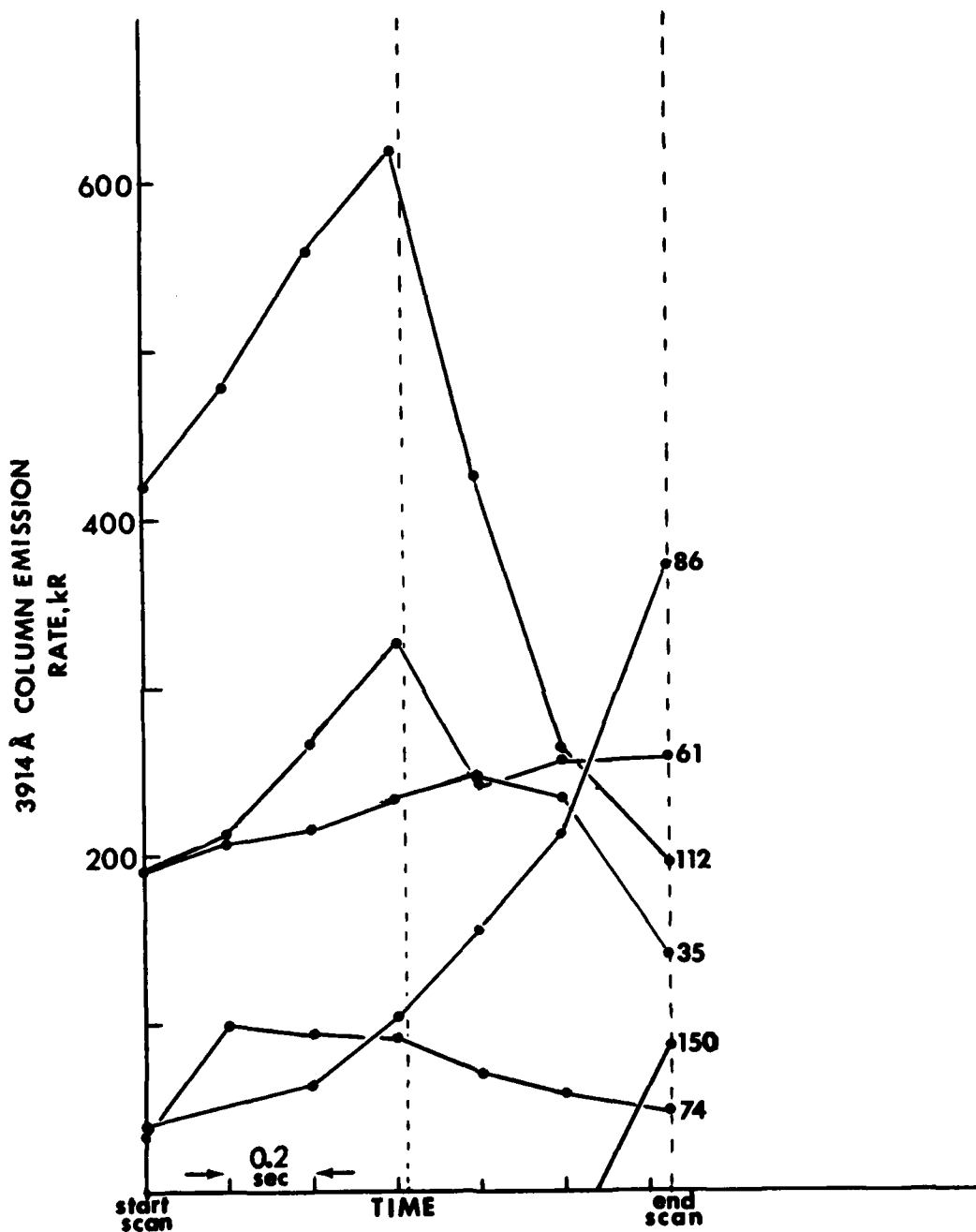
Figure 9. Power inputs within HIRIS II's field during the six limb-viewing scans.

time results from the large range of altitudes over which the projection of the instrument's field intercepts the model particle-energy deposition profiles. In some cases this variation causes significant differences in average power input between the first and second halves of an interferometer scan (1:3.3 in scan 86).

Table 1 summarizes these inputs and those for the three spectrum scans reported in Ref 1 .

As noted, these results are subject to errors from various sources. We estimate the overall accuracy of Table 3's average power inputs to be about + 75%, - 50% (perhaps somewhat worse for scans when HIRIS II was pointing NW).

SECTION 3

ASSESSMENT OF DATA FROM THE AURORAL DYNAMICS PROGRAM

INTRODUCTION

HAES rockets IC 807. 15-1 (auroral measurements payload) and
IR 807. 57-1 (auroral energetics payload) were successfully launched
from Poker Flat Research Range, AK on 26 Oct 78 at 0916:31 and
0929:00 UT. Two further rocket vehicles scheduled for the Auroral
Dynamics Program, one (IC 807. 15-2) intended to take radiometric
data from higher altitudes in the energetic particle-excited volume
toward which IC 807. 15-1 was fired and one (IC 806. 35-1) designed to
release a self-luminous chemical trail for tracing the atmospheric
wind field, failed to reach operational altitude. The purpose of the
coordinated series of rocket probes was to provide information about
the space and time dependence of SWIR emissions that result from
energy input into the upper atmosphere by precipitating charged
particles.

The auroral measurements payload consisted of a liquid nitrogen-
cooled dual channel radiometer sensitive over $\sim 0.2 \mu$m-wide bands
centered at 2.7 and 4. 3μm, and two narrow-band photoelectric photo-
meters for segments of the N_2^+ (0, 1) First Negative Band (near 4278 Å
and 4259 Å) whose intensity measures the column energy deposition
and rotational temperature of N_2. The instruments all had 5° full
angle circular fields of view, which were coaligned along the
rocket's long axis. The auroral energetics payload consisted of a series
of sensors designed to characterize the auroral ionosphere, listed in
Ref 11; among these were axially-pointing photometers for 3914 Å
(N_2^+ First Negative band) and 5577 Å (OI ^{1}S-^{1}D transition). The
radiometer-equipped rocket, launched first, penetrated an intense
isolated auroral arc, as shown in the all-sky montage, Fig 10. The
arc form had moved north of PKR when the second rocket was launched
$12\frac{1}{2}$ min later (Fig 11). The H-, D-, and Z-component magnetograms
from College, AK starting $5\frac{1}{2}$ hr before the Auroral Dynamics launches
are in Fig 12.

Figure 10. Visible auroral radiance distribution (all-sky photographs from Poker Flat) before and during flight of Nike-Hydac rocket IC 807.15-1. The radiometers and photometers point northeast, at 20°-35° zenith angle on upleg and to 100 km downleg altitude. Times are indicated in seconds after launch.

47
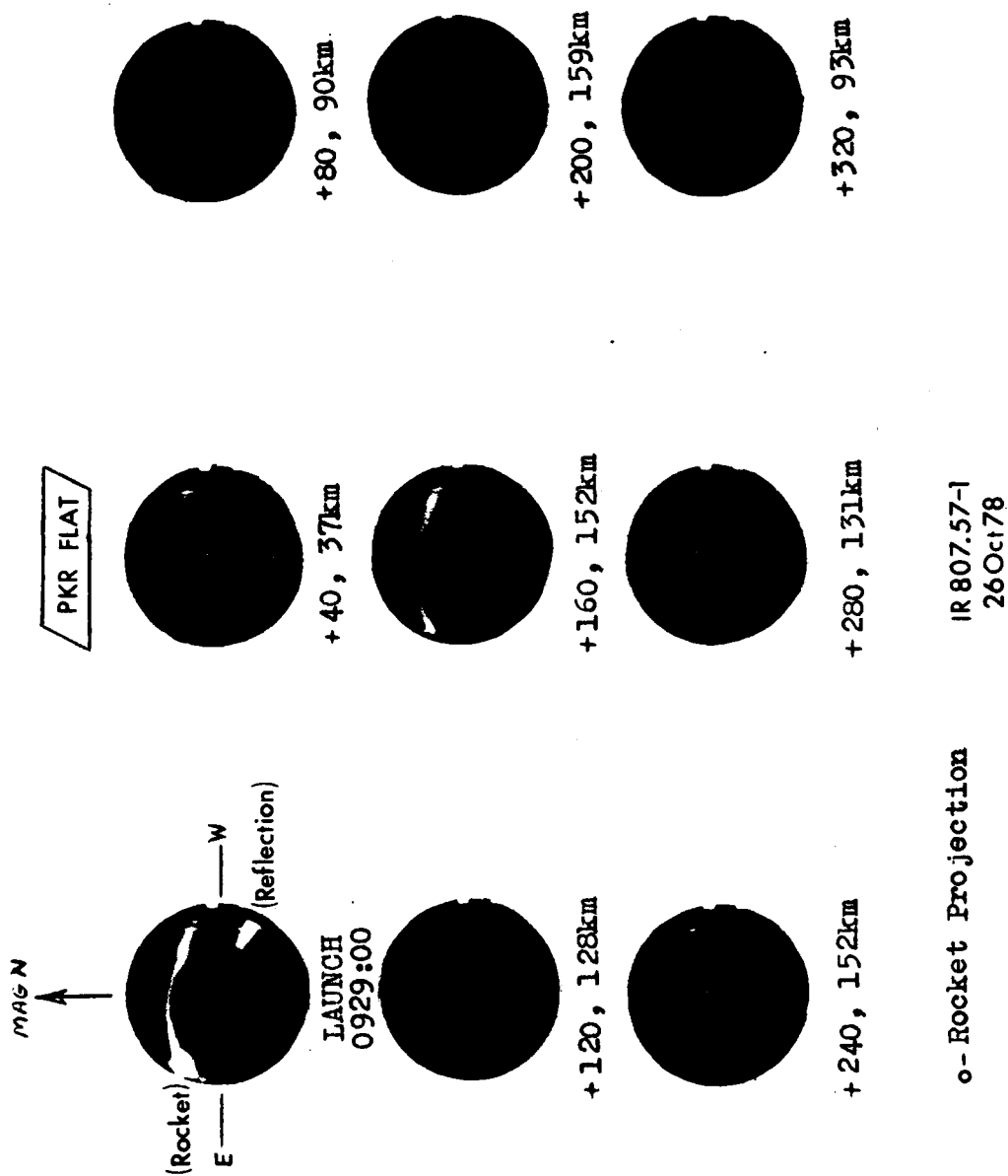
Figure 11. Visible auroral radiance distribution from Poker Flat during flight of Nike-Hydac rocket IR 807.57-1.
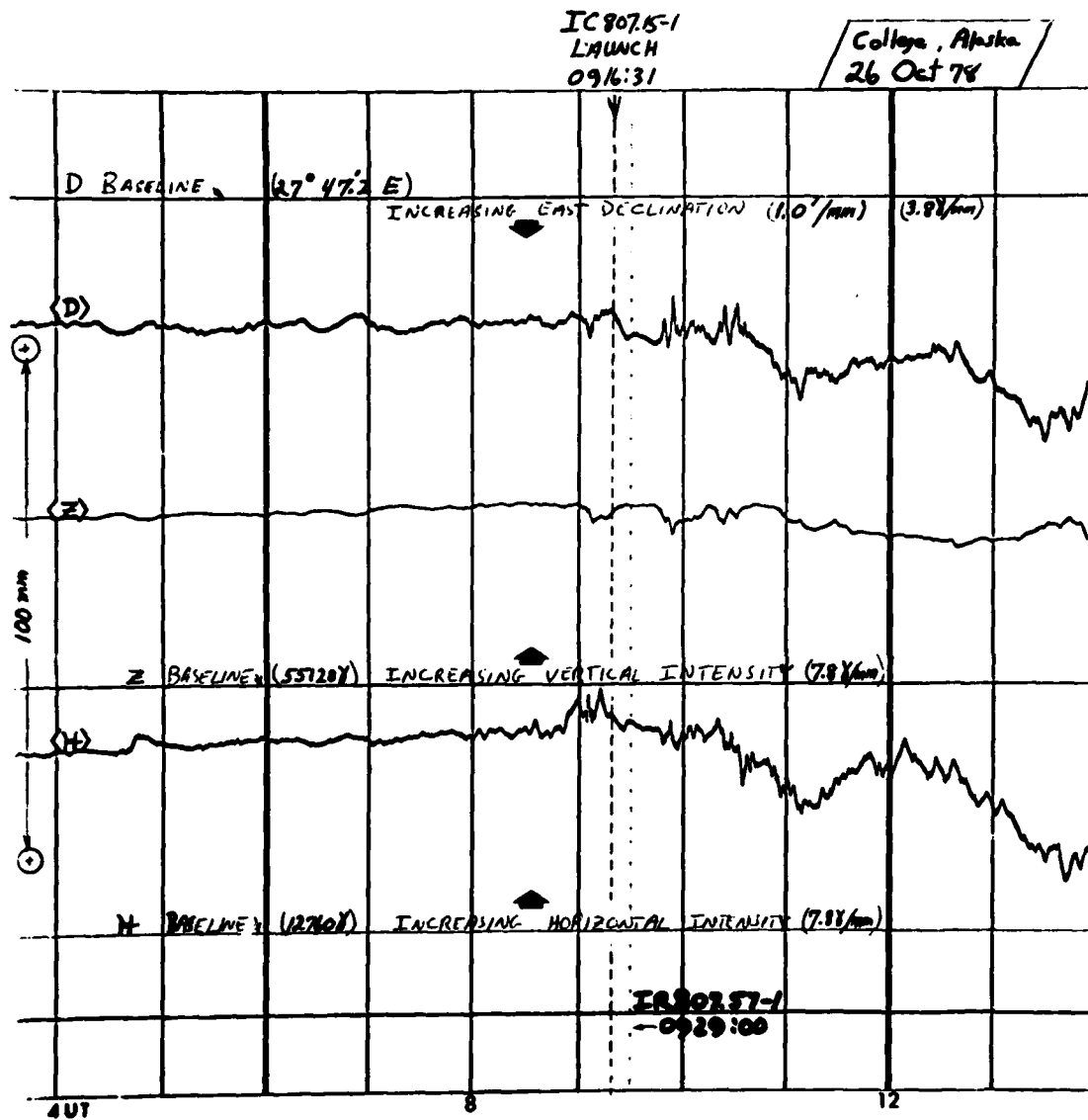
Figure 12. H-, Z-, and D-component magnetograms from College, AK between 0400 and 1400 UT, 26 Oct 78. 100 mm deflection on the original chart records is marked on the left.

In this Section we 1) present data taken by ground-based instruments on the position and intensity of energetic particle bombardment, and locate the emitting volumes with respect to IC 807.15-1's instrument's fields of view; and 2) evaluate the rocket measurements of radiance in the 2.7μm wavelength band. Earlier evaluations of the 2.7 and 4.3μm data, with raw altitude profiles, are in Ref 10 (pages 67 and 329 respectively).

ARC-MEASUREMENTS ROCKET GEOMETRY

Fig 10 shows the development of the visible aurora starting at $20\frac{1}{2}$ min before the first rocket was launched, as seen from Poker Flat. The trajectory plane is at an azimuth of 17° W of geomagnetic N (12° geographic). The projection of the rocket with respect to the optically-thin, "tilted" emitting volume is shown; note that the rocket is not always at auroral altitude. Its instrument fields are coning about a north-east-pointed axis, as shown in the first frame of Fig 10 and in Fig 13 (Ref 10 presents graphs of pointing elevation and azimuth).

Approximately 12 min before liftoff of IC 807.15-1 a narrow arc intensified just south of PKR (at 10° zenith angle). The form then broadened and moved slowly northward, becoming relatively stable near 40° zenith angle (95 km horizontally from PKR) 60 sec before launch. Its position and maximum intensity during the rocket flight is illustrated in Fig's 13 and 14.

The location of the arc's "center" after -100 sec was taken from the zenith angle of maximum 5577 Å surface brightness measured by the meridian scanning photometer at PKR (Ref 12), as no data for triangulation are available from Fort Yukon. For earlier times the PKR images were used. The altitude of maximum energy deposition rate was taken as 110 km, which would result from a 4-keV characteristic electron energy (Section 2). This is the altitude of maximum electron density measured in the single elevation scan by the Chatanika radar, which crossed the arc region between $\sim$ 320 and 400 sec
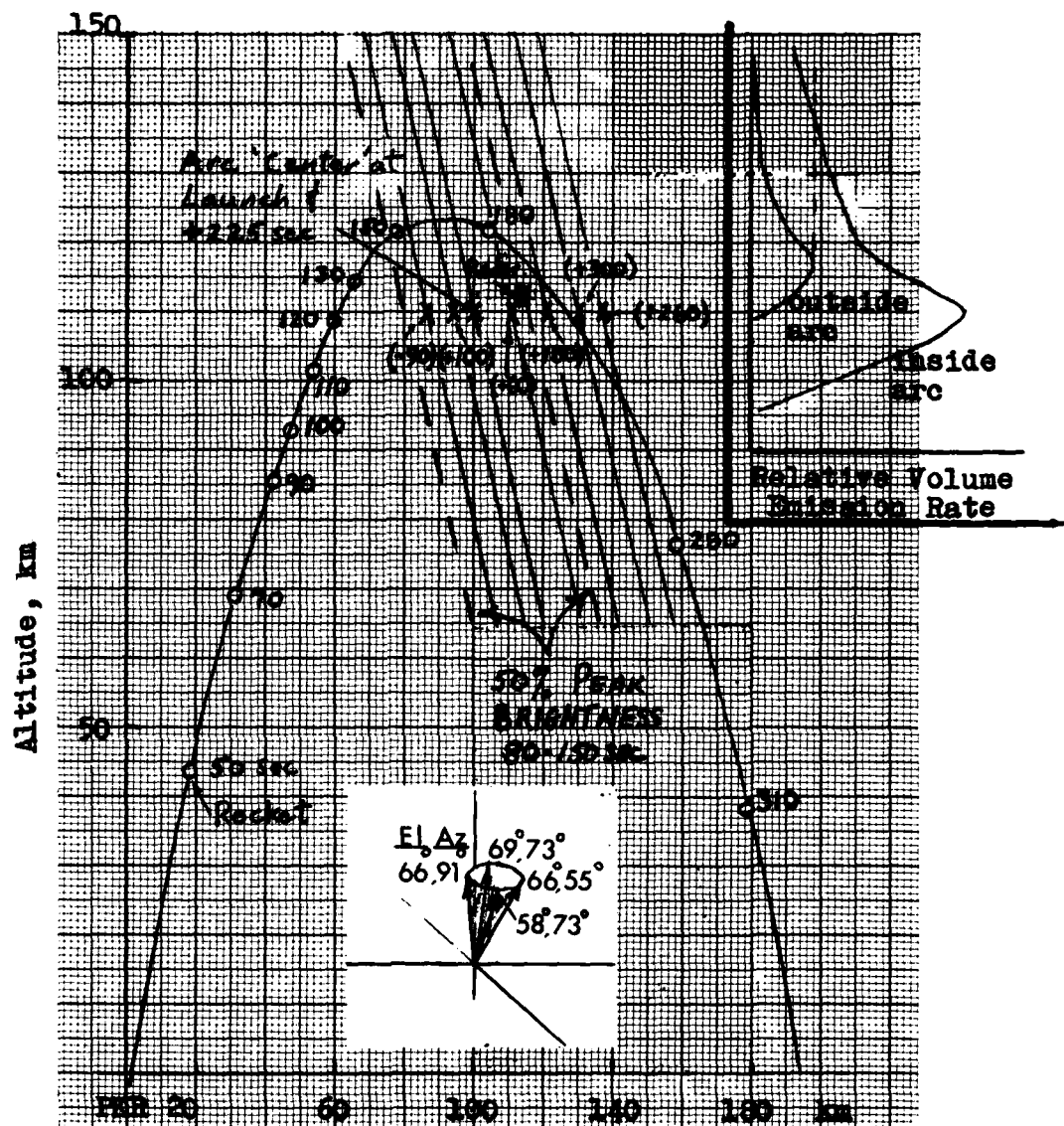
Trajectory Plane Projection

Figure 13. Trajectory plane projection of IC 807.15-1's flight path ($\sim 17^\circ$ W of magnetic N) and the arc's "center." The arc is again located from the zenith angle at which its surface brightness is a maximum, with 110 km altitude assumed. Location of maximum electron density measured by the Chatanika radar near 375 sec is also shown. The dashed line represents the region of half-brightness as projected to PKR during most of the upleg data segment. The inset at upper right indicates how weak precipitation S of the arc contributes to the photo-meter-radiometer signal. The isometric plot at the bottom illustrates the rocket instrument's range of pointing angles.

51
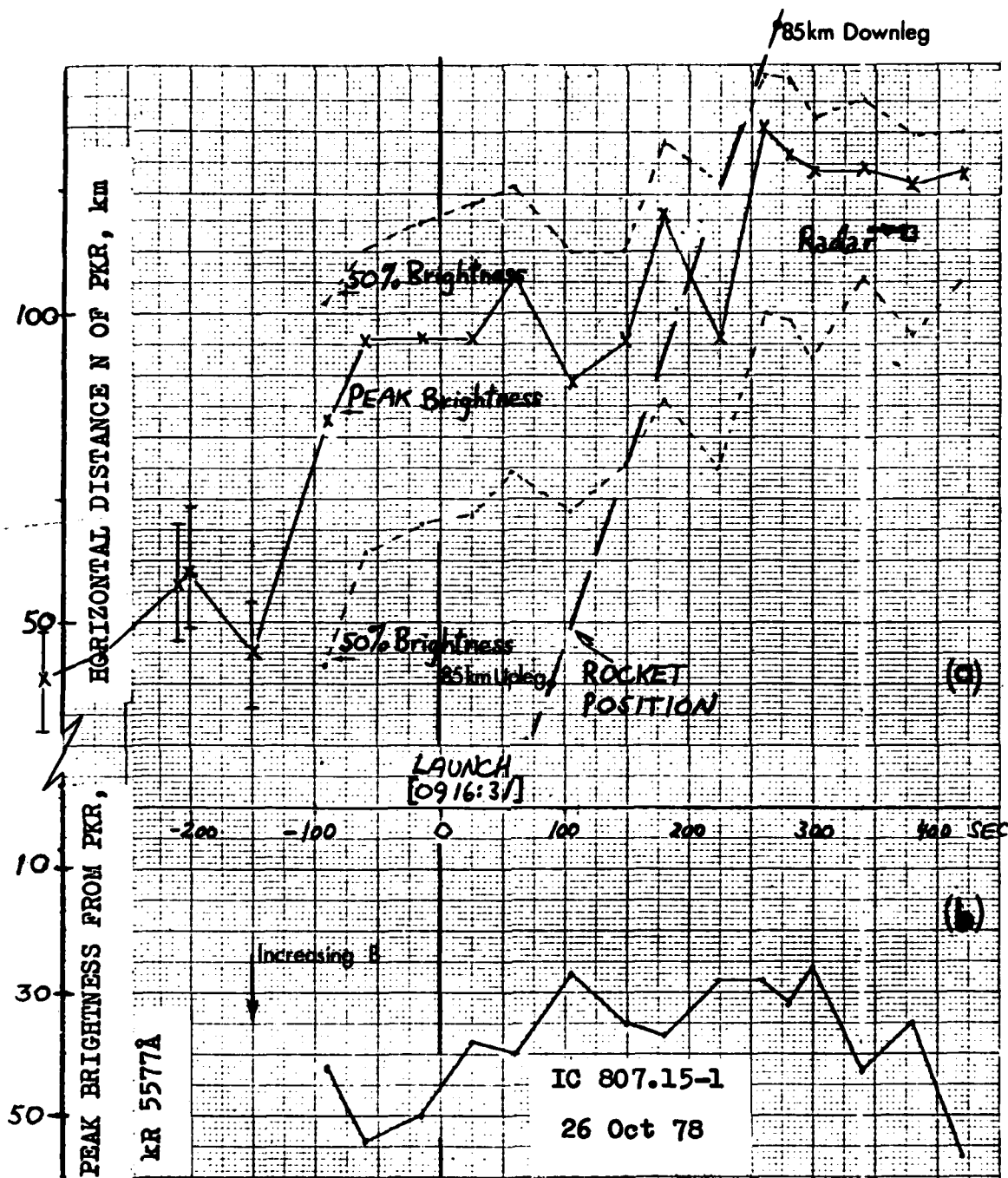
Figure 14. Horizontal distance magnetic north of PKR of the arc's
"center" and half-maximum-brightness points (a),
and peak 5577 Å radiance (b) during flight of IC 807.15-1.
As no meridian photometer or photographic data from
FYU are available, the altitude of peak volume emission
rate was estimated from the mean intensity as 110 km. The
location of the arc before -100 sec was determined from
the PKR 35 mm all-sky photographs, and after -100 sec
from the meridian photometer scans. The position of
maximum electron density measured by the Chatanika radar
facility near 375 sec is also shown.
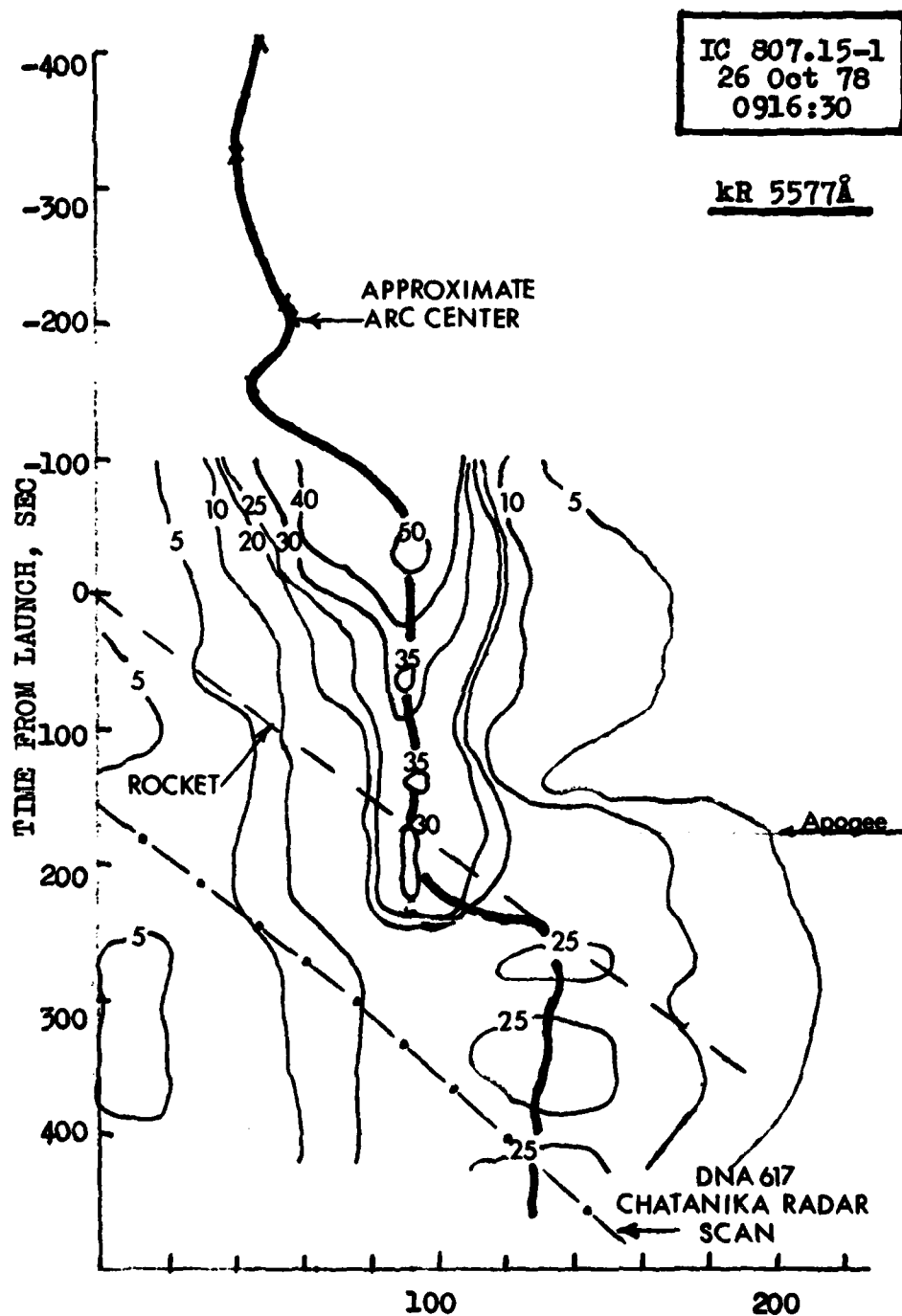
Figure 15. Time-range contour plot of radiances at 5577 Å before
and during flight of IC 807.15-1, which are proportional to
energy input rates. The dotted line is the 110-km altitude
intercept of the Chatanika radar's meridian scan.

after launch (Ref 12).   In this segment of the meridian-plane incoherent scatter radar scan, made between 11 sec (eℓ 125°) and 479 sec (eℓ 30°), the arc center was 112 km N of PKR, as marked in Fig's 13 and 14.

Near launch the arc was relatively stable at 95 km N, and slowly decreasing in 5577 Å brightness. It moved generally northward during the data-taking segment, and its intensity held constant to within ± 20%.   The rocket, whose horizontal velocity was 0.6 km/sec, crossed the arc center's field line just after it reached apogee, near 200 sec after launch.

Relative positions of the rocket and arc are shown in the trajectory plane projection, Fig 13 .   The rocket body was precessing as shown, with the axially mounted instruments scanning on a cone of about 15° opening angle with axis at ~60° elevation, 40° geomagnetic azimuth until 93 km on downleg (where it began to lose stabilization).   Thus the radiometer and photometer fields intercept the particle-irradiated air volumes over a wide range of altitudes.   (We return to this important point shortly.)

A time-range contour plot of the zenith fluorescent radiances, which are proportional to the column energy input, is in Fig 15.   The plot was compiled from the Poker meridian photometer traces, with the assumptions that the particle excitation all takes place at 110 km and that van Rhijn enhancement away from the zenith direction (radiance gain due to increased path length through the emitting volume) is compensated by atmospheric scattering loss and thus can be neglected. From Fig 15 the predosing in near-vertical columns extending down to ~95 km can be calculated   and, with the aid of model altitude profiles of energy deposition, estimated for columns above the rocket.

ARC-ENERGETICS ROCKET GEOMETRY

The visible auroral radiance distribution during flight of the

54
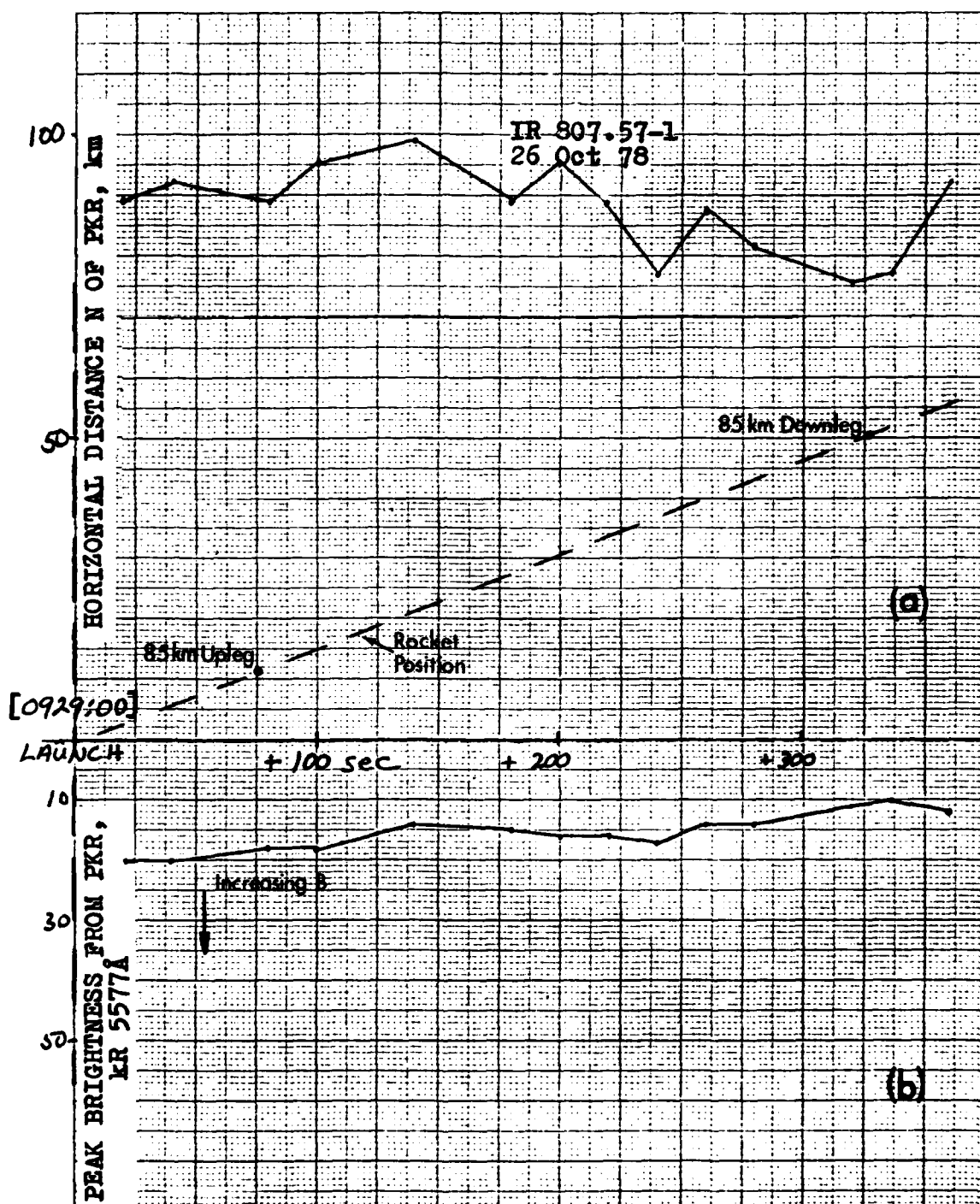
Figure 16 . Horizontal distance magnetic north of PKR of the arc's "center"(a), and peak 5577 Å radiance measured by the meridian-scanning photometer at PKR (b) during flight of IR 807. 57-1.

second rocket (IR 807.57-1) is in Fig 11. At the time of launch (0929) the arc had moved back closer to PKR (it was 90 km north) and weakened slightly (to 20 kR 5577 Å). As Fig 16 shows, its position and intensity stayed nearly constant throughout the data-taking segment of the flight.

The second rocket's shallow trajectory (62 km ground range, 160 km peak altitude), did not allow it to reach the region of intense particle precipitation; at 85 km on downleg the horizontal range to the arc center was 25 km. Its near-zenith pointing photometers' fields therefore intercept the arc at altitudes well above those where most of the energy is deposited. (IR807.57-1 carried no infrared-sensitive radiometers.)

PRELIMINARY ASSESSMENT OF NO OVERTONE PHOTON YIELD

Altitude profiles of the ratio of 2.7μm/3914 Å photon emission rates on upleg and downleg of IC 807.15-1 (from the radiometer and photometer profile data in Ref 14) are shown in Fig 17. The 3914 Å-band intensities were as usual taken as 2.9 x the measured 4278 Å intensities. The 2.7μm radiometer's 2.636 - 2.859μm FWHM covers 60% of the expected emission in the NO $\Delta v = 2$ sequence, as derived in Ref 10. Ratios in Fig 17 have not been corrected for the out-of-band N_2^+ First Negative and NO overtone spectral components, pending receipt of the detailed instrument sensitivities. This correction is expected to change the ratios in Fig 17 by less than 20%.

The measured radiations originate from a range of altitudes above the rocket, as illustrated by the arc-rocket separations, instrument pointing angles, and model energy deposition altitude profiles in Fig 13. Note (upper right) that particle precipitation along field lines closer to the rocket platform – that is, south of the isolated arc – also contributes to the column-integrated emission measured on upleg. The maximum column energy inputs measured on upleg from the rocket are about a factor two below those measured from PKR

56
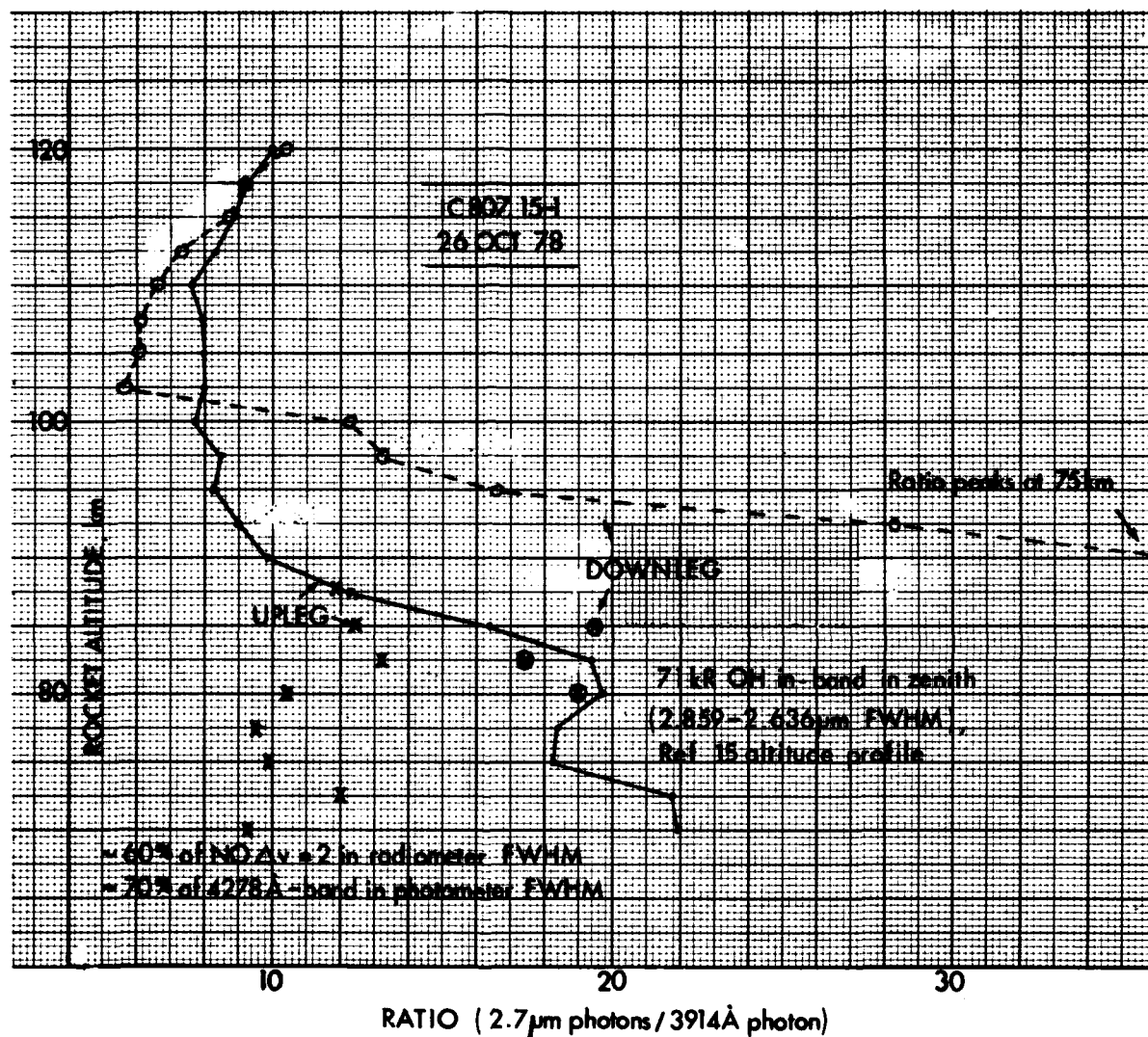
Figure 17. Altitude profiles of 2.7μm/3914 Å photon ratios from upleg
and downleg of IC 807.15-1.   3914 Å column intensities
were taken as 2.9 x 4278 Å intensities. The radiances
have not been corrected for the fraction of expected
sequence or band emission within the instrument FWHM;
refer to the text. The points labeled x and ⊕ have a
correction for OH fundamental-band airglow, also
described in the text.

(corrected for atmospheric scattering), which is consistent with the projections shown in Fig 13.

An effective altitude to which each photon ratio refers – or at a minimum, a weighted range of altitudes – can be derived from the volume emission rate distribution in the upper atmosphere. This distribution is calculated following the procedure applied to HIRIS II in Section 2 . For most accurate results, the electron density profiles measured by the Chatanika incoherent-scatter radar, which was operating in elevation-scan mode in the geomagnetic meridian plane (17° in azimuth from the trajectory plane), should be applied along with the meridian photometer data, since the sky brightnesses near the arc have a large component from scattering by the lower atmosphere (as is shown in Section V of Ref 5). Hence we have posponed calculating the energy deposition profiles within the photo-meter's field of view – which involves considering the three-dimensional geometry of the arc, as the instrument fields have a substantial east-ward-pointing component – pending receipt of the reduced data from the radar group.

At the lower downleg altitudes, after the rocket crosses the arc region, the radiances are about an order of magnitude less than on upleg. The photon ratios are therefore subject to greater uncertainty, particularly below ~ 90 km where OH vibrational-fundamental (Meinel) band airglow radiation begins to contribute to the 2. 7μm signal. The model hydroxyl spectrum in Ref 1 predicts a zenith night-glow intensity of 71 kR within the radiometer's FWHM when the rocket is below about 80 km. Results of a correction for this excess signal, applying the low-v OH emission altitude profile (model A) from Ref 15 and the appropriate van Rhijn factor, are shown in Fig 17.

This correction can be improved by using the independent measurements of hydroxyl airglow column intensity from Poker Range (Ref 14). The results, however, are quite sensitive to the OH profile

adopted. Since the rocket axis pointed at decreasing elevation angles below 93 km on downleg, and away from the isolated arcs, the corrected air fluorescence-associated emission becomes even more sensitive to the absolute OH profile; hence the higher-than-expected photon ratios on downleg. The mean ratio when the instruments are looking at the particle-irradiated volumes from below ~ 90 km is very close to the value reached above 115 km rocket altitude.

Both photon ratio profiles indicate a minimum in 2.7μm-band yield near 105 km rocket altitude. The variation is qualitatively similar to that measured by the essentially horizontally pointing 2.7μm radiometer on A18.219-1 (Fig 47 of Ref 5), which scanned a narrow arc from co-altitude. A minimum in 2.7μm photon yield near 100 km is predicted by calculations of collisional deactivation of $NO^{\ddagger}$ by atomic oxygen (Ref 16), and in fact quenching by O is a major issue in prediction of the sky background from this molecule under nuclear-disturbance conditions. We plan to further evaluate the altitude dependence of effective yield of 2.7μm-band photons -- most of which are believed to come from NO $\Delta v = 2$ transitions -- using the O-concentration profile that was measured from IR 807.57-1 and the altitude of energy deposition calculated as described above.

Taking from Fig 17 an average of 8 2.7μm photons per 3914 $\overset{\circ}{A}$ photon measured between 95 and 110 km rocket altitude, 60% of the NO overtone sequence within the radiometer's FWHM and 70% of the 4278 $\overset{\circ}{A}$ band within the photometer's FWHM, and $20\frac{1}{2}$ ion pairs produced per 3914 $\overset{\circ}{A}$ photon emitted (Ref 5), we calculate an average "equilibrium" NO-sequence yield of 0.6%. This preliminary figure, which applies to the emitting column as viewed from below, is in good agreement with the 0.4% to 0.7% measured from the aircraft (Ref 1 and Section 1), and also with the "average" from A18.219-1's side-looking 2.7μm radiometer.

RECOMMENDATIONS

Measurements of the altitude profile of effective NO vibrational overtone yield in natural particle-excited air have more accuracy when the radiometric instruments are pointing at low elevation angles than toward the zenith, as the effective altitude of emission is better defined. The hydroxyl airglow profile, monitored with an onboard 1.7μm-band radiometer (as on the aircraft, Ref 1) would further improve the data on 2.7μm chemiluminous yield. Power input could be more precisely defined by limiting the scan of one of the meridian photometers (at present three independent systems are available at PKR) to a narrower range of elevation angles, thus providing more frequent sampling of the radiance distribution in the auroral region important to the rocket measurements.

SECTION 4

A COMPARISON OF AIRCRAFT PHOTOMETER AND INCOHERENT-SCATTER RADAR MEASUREMENTS OF PARTICLE ENERGY INPUT PROFILES

PURPOSE

To determine altitude profiles of energy deposition in particle-irradiated air whose SWIR emission was being measured from the AFGL/DNA KC-135 aircraft, we coordinated the pointing of the DNA 617 radar at Chatanika with some of the Mar 76 flight trajectories. This Section reviews the results of this coordination effort (which is described in Section VI of Ref 5), and compares an auroral-excitation profile determined from the ratio of auroral feature intensities (Appendix II of Ref 5) with some determined from the free electron density distribution measured by the incoherent-scatter radar.

OVERLAP OF INSTRUMENT FIELDS

A direct comparison of radar and photometric altitude profiles can be made when the instrument beams intercept the same volume of auroral ionosphere. Additionally, radar measurements on regions of equal surface brightness that are not too distant in space and/or time from the radiometer's field, can be considered applicable to the SWIR chemiluminescence yield data. Simultaneous measurements on an arc some tens of km in longitude from the aircraft would be in this category, as it is generally accepted that the distribution in energy of the incoming electrons has only a small variation in the E-W direction.

In practice, these overlap conditions were rarely achieved on regions of intense particle precipitation (IBC $\gtrsim$ II aurora). This is due in large part to the impracticality of reprogramming the radar's antenna motion to "track" the aircraft fields. Thus the common sampling (Fig 74 of Ref 5) has a short duration, at an interval long compared to the characteristic variation times of auroral energy input, a point that we will illustrate shortly. Furthermore the radar facility was available

61
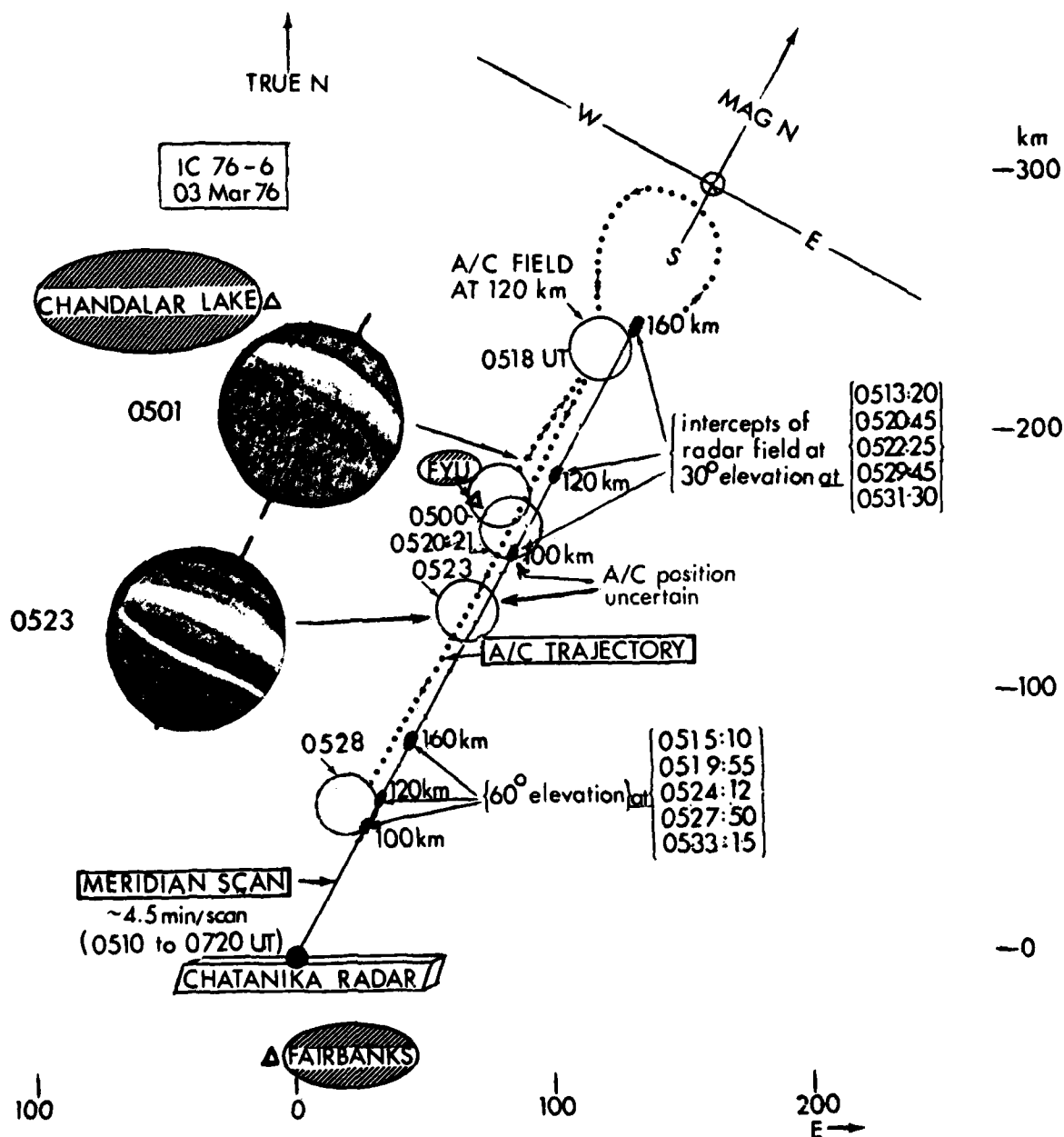
Figure 18 . Plan view of geomagnetic meridian-scanning radar and aircraft-
instrument fields in a segment of flight IC-76-06 (03 Mar 76).
The open circles are the intercepts of the zenith-pointing radio-
meter- and-photometer's 10° field of view at 120 km altitude,
and the smaller ovals are the intercepts of the elevation-
scanning 0.6° radar beam at the three altitudes indicated. A
photometer with 2° circular field is coaligned with the 10° air-
craft instruments. The two all-sky photographs show that the
arc forms are essentially uniform over the E-W separation
of the instrument beams.
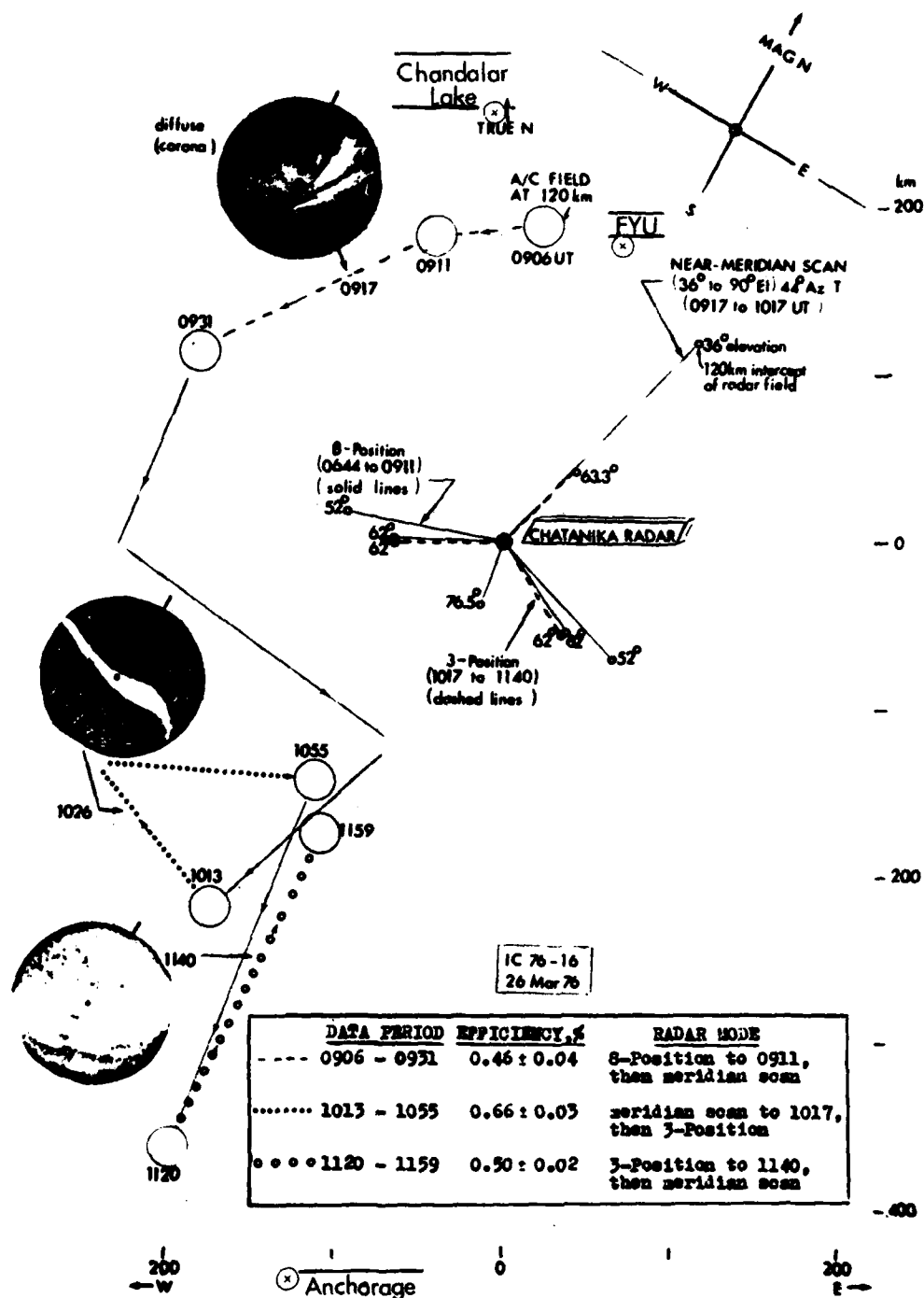
Figure 19. Plan view of radar and aircraft-instrument fields in the high-signal/noise SWIR data segments of flight IC-76-16 (26 Mar 76). Beam intercepts at 120 km altitude are shown. The radar was operating in both elevation-scanning and azimuth-sampling modes during the flight. The all-sky photographs show that measurements from the aircraft would not refer to the same particle energy input profiles as those from the radar near Poker Range.

Figure 20. Smoothed contour plot of electron density in the meridian plane through Chatanika, compiled from a zenith-to-30° elevation scan between 0517:05 and 0521:33, 03 Mar 76. The all-sky photographs of the aurora in Fig 22 cover the time period between 61.5° and 16° elevation angle.
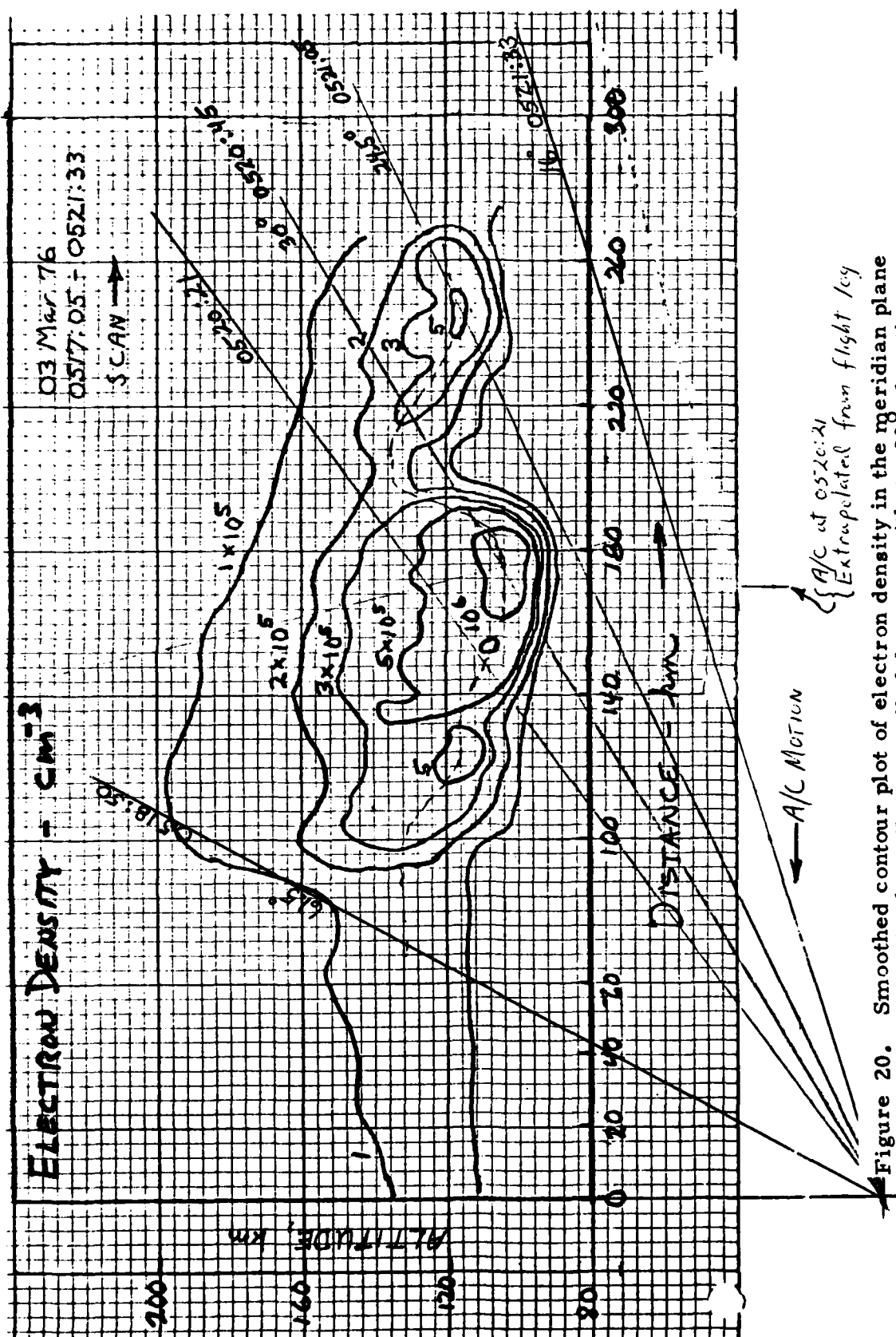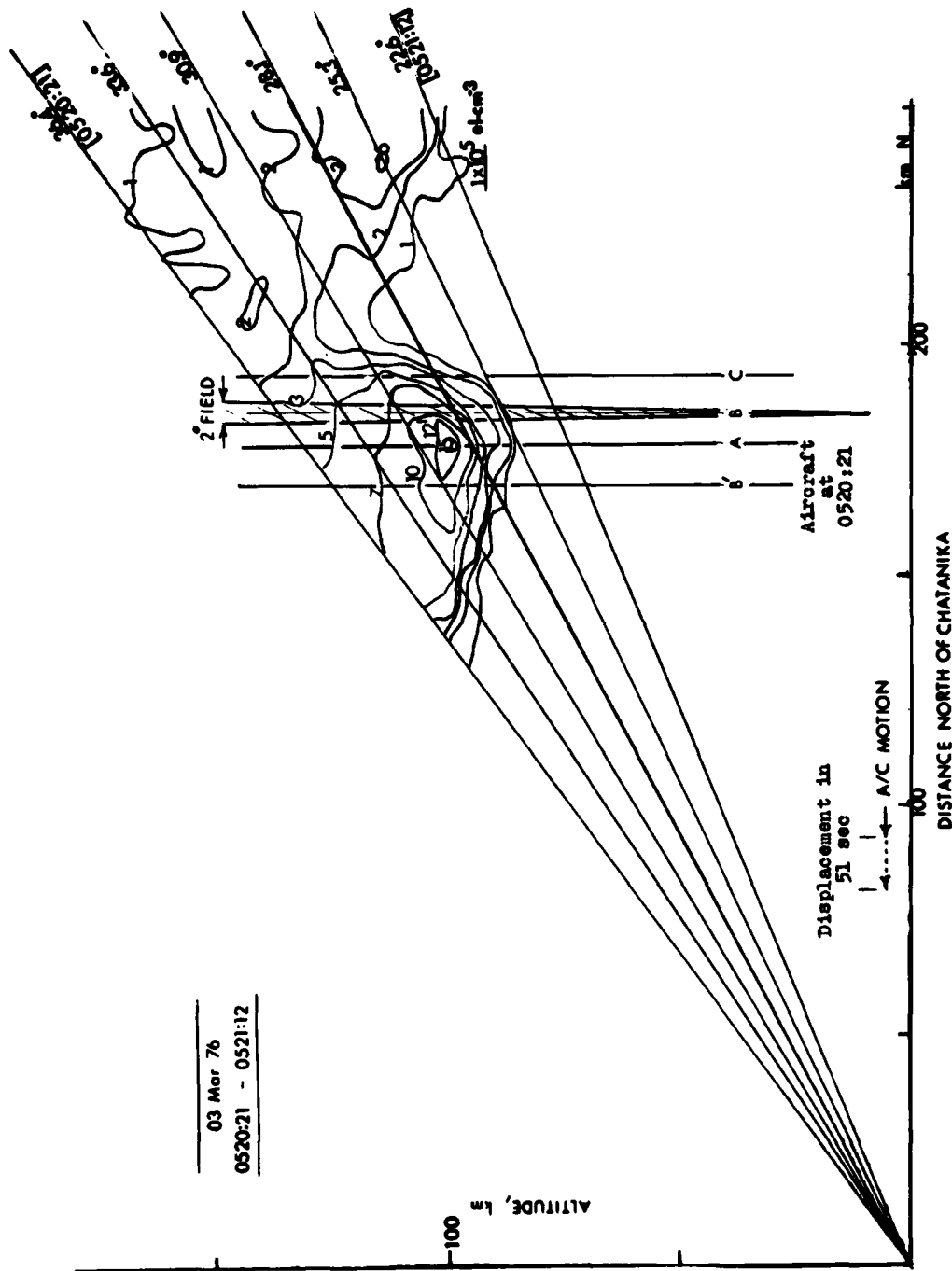
Figure 21. Meridian-plane electron density contour plot, compiled from the computer listing for 0520:21 - 0521:12, 03 Mar 76. At 0520:21 the aircraft is at B', apparently 10 km S of the electron density peak, which is measured near 0520:45.

only over a limited flight period, as its prime mission was support of rocket investigations (it measured ionospheric winds and electron densities near the probed volumes in the long pre-launch periods, during which the aircraft was excluded from Poker Range for safety reasons).

Table 8 of Ref 5 lists the segments of the flights in which the field viewed the same, or similarly particle-irradiated, air volumes. To determine when these periods coincide with sufficiently intense auroral particle precipitation for high-signal/noise SWIR data, we reviewed the radiometer and photometer records and the all-sky photographs from the aircraft, referring them to the navigator's logs of its position. The best coordinated results are in the 03 Mar mission, illustrated in Fig 18.

Fig 19 shows a similar projection during the three segments of the 26 Mar flight that provided good SWIR chemiluminescence yield data. The radar, which was alternating between meridian-scanning and azimuth-sampling operation modes (to measure winds and electric fields), did not enter the aircraft radiometer's 10° field or cross "spatially-stable" forms whose SWIR emission it measured. Not drawn into Fig's 18 and 19 is the 2° circular field of the aircraft photometer that determines altitudes of peak energy deposition rate, whose optic axis is coaligned with the radiometer's to within $\pm 1^\circ$ (estimated).

ENERGY DEPOSITION PROFILES

As the plan view in Fig 18 shows, the radar's 0.6° beam crosses the radiometer's field at auroral altitudes near 0521. The meridian-plane projection of the radiometer's pointing into the particle-irradiated region is in Fig's 20 and 21, which are contour maps of ionospheric electron density measured in the $16\frac{1}{2}^\circ$/min elevation scan that spans this time (Ref 17). (The plot for the full $4\frac{1}{2}$ min S→N scan was drawn by the radar group; we redrew the contours at higher resolution (in Fig 21) from a computer listing provided for 0520:21 - 0521:12.) All-sky views from the aircraft while the antenna's elevation was
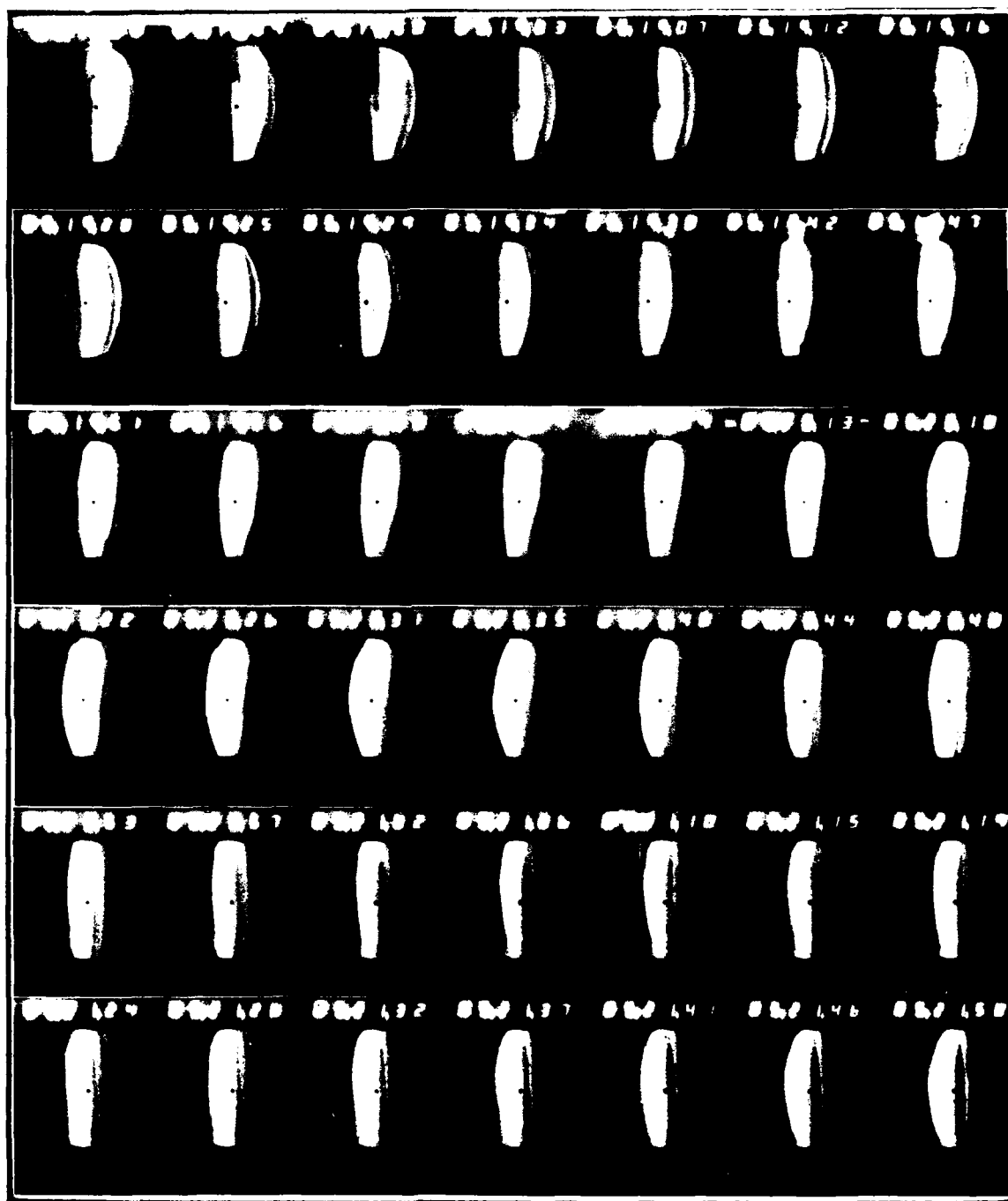
Figure 22. All-sky photographs (160° field) of the aurora from the
aircraft during the $61\frac{1}{2}^\circ$ to 16° segment of the radar
elevation scan in Fig 20. The aircraft is moving toward
the 3 o'clock position at approximately 1/10 degrees of
zenith angle/sec.

67

between $61\frac{1}{2}°$ and $16°$ are in Fig 22. Zenith intensities in the 4278 Å band sampled each 24 sec during the radar scan by the narrow-field aircraft photometer are in Fig 23.

The maximum 4278 Å intensity is $14\frac{1}{2}$ kR, at 0520:21. The aircraft's position at this time, interpolated after correcting the navigator's log (p 131 of Ref 6) for what appears to be a transcription error, is indicated on Fig's 20 and 21. (We shifted the entry labeled 0518 to 0513, which makes the interval between latitude-longitude fixes consistent with that otherwise taken and with the usual aircraft ground speed of 0.22 km/sec.) Radiometrically-calibrated microdensitometer traces of the 4-sec all-sky exposure starting at 0520:22 place the aircraft about 45 km S of the brightest auroral region, which is ~ 23 kR 4278 Å (in the projection to the aircraft, normalizing the film densities to $14\frac{1}{2}$ kR in the zenith; Fig 24). Thus between 0519 and 0522 the zenith-pointing aircraft instruments have not measured in the direction of the highest auroral radiance at 0520:22 - :26.

In the contour plot (Fig 21), on the other hand, the aircraft is only 10 km S of the latitude of the peak electron density. This apparent anomaly is most likely due to the fact that the contour map is not a "snapshot," but rather a scanning-image compiled over a period of ~ 1 min, during which the electron densities can be changing. The arc system has in fact moved somewhat southward before the radar beam sweeps down to intercept what is then its maximum electron density, as is indicated in Fig 22.

Since there is some inherent ambiguity in the data from the radar's elevation scan, we computed altitude profiles of electron production rate at four meridian-plane positions in what is assumed to be a constant auroral ionosphere. These are compared in Fig 25 to the profile at 0520:21 determined from the N_2^+ 4278 Å and OI 6300 Å
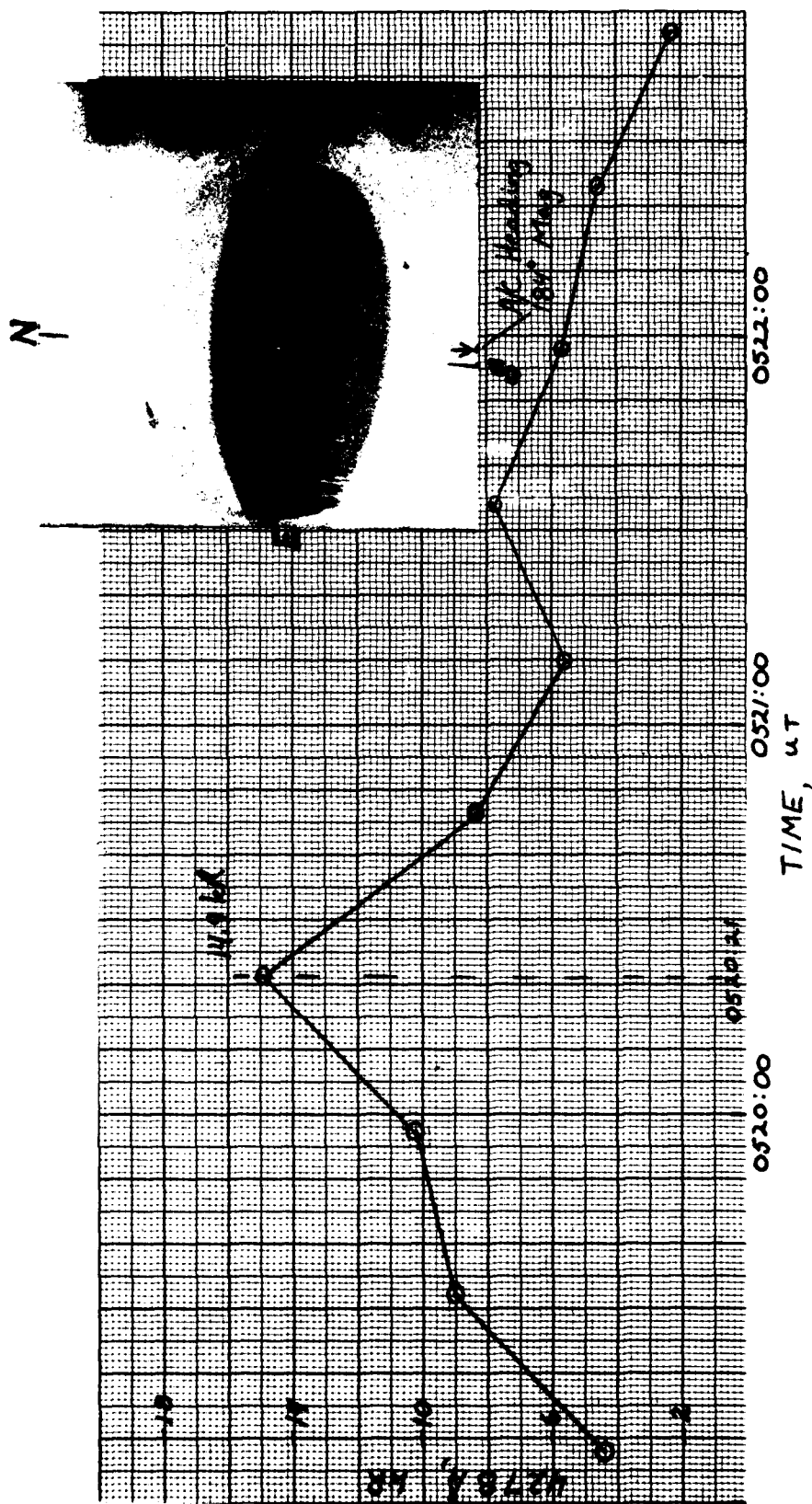
Figure 23. Zenith brightnesses measured by the aircraft's 2°-field 4278 Å photometer near the time of the spatially-coordinated radar elevation scan. The all-sky photograph from the aircraft at the time of maximum signal is in the inset.
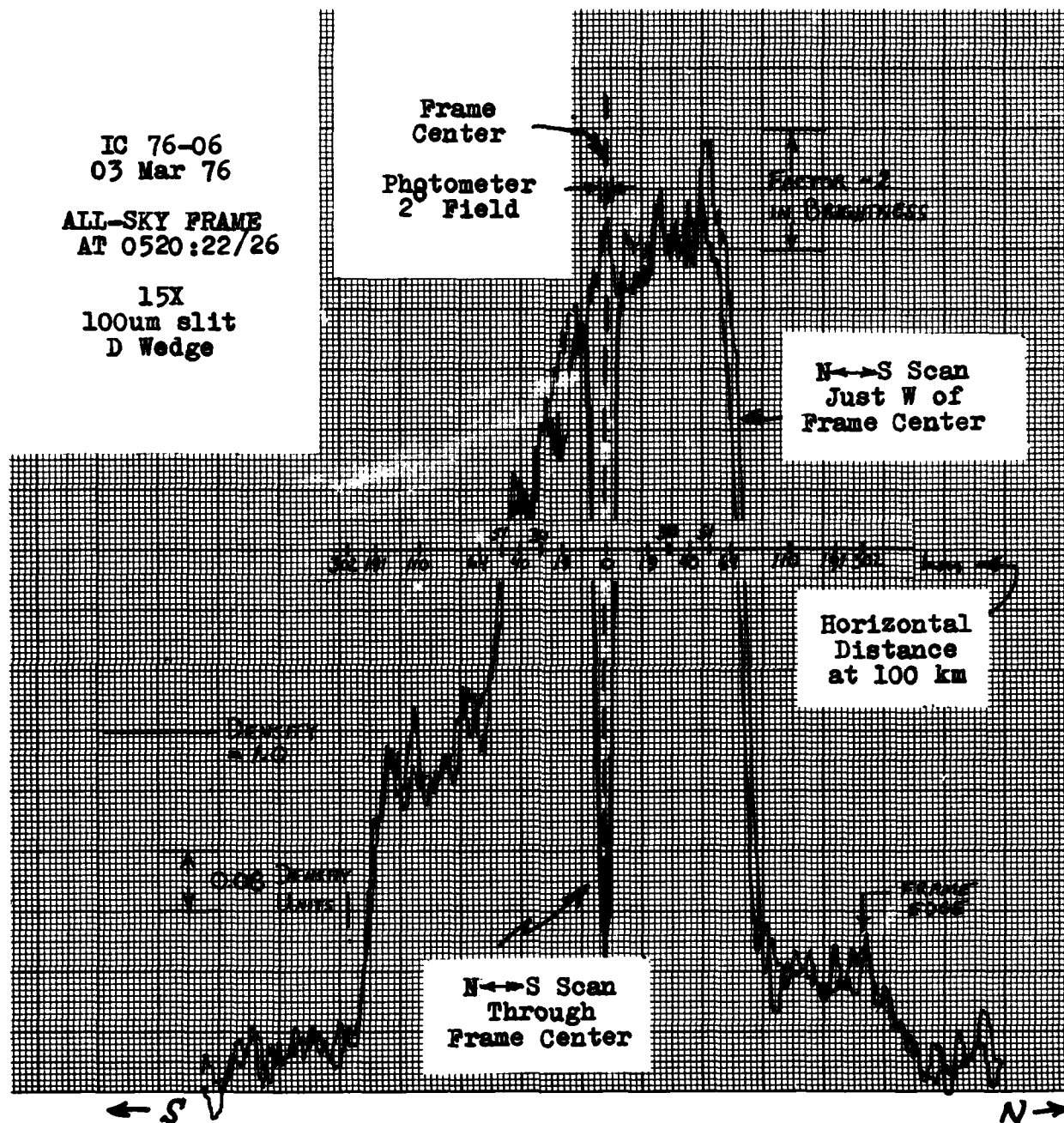
Figure 24. Microdensitometer scans across the 0520:22-:26 all-sky frame in Fig 23. The aircraft's zenith photometer is pointing about 45 km south of the brightest region of the arc (in the projection to the aircraft).
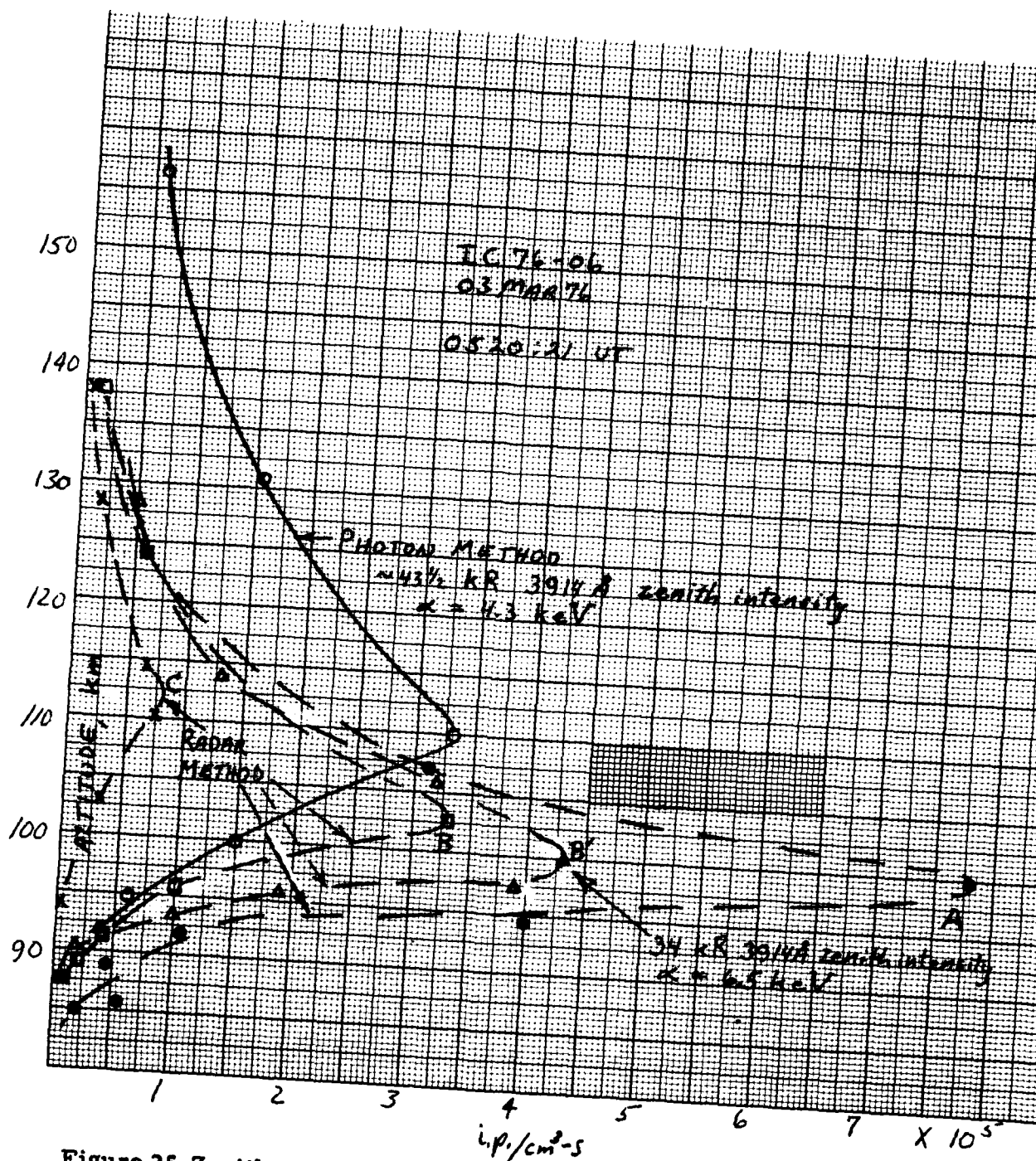
Figure 25. Zenith profiles of the volume rate of production of ionization by precipitating electrons near 0520:21, as determined by the photometric method and from the radar backscatter data. Locations of the vertical cuts through the contour plot of electron density are in Fig 21.

zenith column intensities. The two spectroscopic parameters give the altitude and magnitude of the peak in rate of production of ion pairs; this point normalizes a canonical profile shape that would result from a Maxwellian incident electron distribution with characteristic energy α (the energy at the peak of the differential spectrum). We used the altitude-dependent recombination rate coefficient from Ref 18 in converting the electron densities from the incoherent-backscatter intensities to rates of production of electrons.

DISCUSSION

The zenith profile at the aircraft's position B'derived from the radar's elevation scan has a somewhat higher maximum than the photometric profile, at 10 km lower altitude. It also has a narrower halfwidth,so that the column-integrated ion pair production rate (marked in Fig 25), or total flux of incident energy, comes out some 20% lower. The variability among the four profiles within 15 km of the maximum electron density indicates the importance of locating accurately the volume of SWIR-emitting ionosphere to which the radar data apply.

Each of the two methods for assessing energy deposition altitudes has inherent sources of systematic error, which are reviewed in Appendix II of Ref 5 . Simultaneous measurements over a period of 1-1/3 hr from Chatanika, with both the radar and a groundbased photometer pointing up the geomagnetic field line at the same ionosphere volume (Ref 19), indicate reasonably good average agreement between the α's determined by the two methods. The spread in the cross-correlation plot is comparable to the difference found in this single comparison between an aircraft-based zenith photometer measurement and a radar measurement compiled from incoherent backscatter returns from a series of (high) zenith angles.

In conclusion, the results from the Mar 76 flight series show that the restricted geographical region of the incoherent scatter

radar measurements, the low effective common sampling time (and rate), and the inherent ambiguity (time-space mix) of electron concentration profiles from elevation scans, limit the application of radar data in interpreting measurements from aircraft of SWIR radiation from the upper atmosphere.

SECTION 5

AIRCRAFT MEASUREMENT OF PARTICLE-EXCITED SWIR EMISSION FROM THE SUNLIT ATMOSPHERE

INTRODUCTION

At latitudes above about 60° subsonic jet aircraft are able to fly patterns that hold the solar elevation constant for several hours, while remaining within the auroral oval. When the sun's depression angle is less than $10 - 11^{\circ}$ it illuminates the atmosphere at altitudes where precipitating charged particles deposit their energy (as we will show). When it is greater than $7 - 8^{\circ}$ the near-zenith background intensities that result from Rayleigh scattering of solar photons are less than the visible fluorescent intensities excited by these particles, and even at smaller depression angles the accompanying short-wavelength infrared chemiluminescence is measurable with good signal/noise (as we will also show). Thus by maintaining the solar elevation within a range of a few degrees SWIR photon yields from the sunlit auroral ionosphere can be determined.

AFGL's IR/Optical Flying Laboratory NKC-135 55-3120 flew evening and morning twilight missions for this purpose in Alaska and eastern Canada in Sep 77, Apr 79, and Sep 79. These flights represent the only DNA attempt to assess the relationship between SWIR output and energy input in the solar-illuminated upper atmosphere. The auroral activity encountered was at most times weak, and the data from the 1979 series – which are the most promising – have not yet been processed by the experiment group into a form optimum for further assessment. In the 1977 flights the zenith-pointing photometers and radiometers made good measurements of the intensity of scattered radiation at several wavelengths between 0.39 and 2.9μm when the sun was a few degrees below the sea-level horizon. In this Section we present these results, and address the question of what information about the SWIR sky backgrounds excited by nuclear explosions can be derived from radiometric measurements on the "daytime" particle-irradiated atmosphere.

74

SOLAR ILLUMINATION OF THE UPPER ATMOSPHERE

Near 60° latitude the sun's elevation dips below -8° in the period between a month before the autumnal equinox (21 Sep) and a month after the vernal equinox (21 Mar). In the spring and summer the maximum solar depression angle decreases with increasing latitude, so that the sun remains too near the horizon to allow air fluorescence to be measured with a high ratio of signal to scattered-light background. AFGL/OPR has developed programs for calculating the generally-northwest (evening twilight in the northern hemisphere) or southwest (morning twilight) flight trajectories that maintain near-constant solar elevation while staying within the $Q = 3$ auroral oval in airspace permitted to USAF craft (Ref 20). Contrary to intuition, some of these flight paths can actually be toward the northeast. We note also that aircraft trajectories that emphasize previous exposure of the upper atmosphere to sunlight can also be designed.

Fig 26 (Ref 20) shows that the solar elevations(computed in real time from the navigator's statement of aircraft latitude and longitude) during three flights $1\frac{1}{2}$ weeks before the 1977 autumnal equinox were held within $\pm 1^{\circ}$ for up to 3 hr. The accuracy of navigation needed can be estimated from the rate of change of elevation near twilight at a ground point at 65° latitude, 10 min per degree. As noted, particle precipitation was too weak during the periods that auroral altitudes were sunlit in these flights and in the twilight-transition flights of 06 and 16 Sep (discussed later) to produce useful SWIR chemiluminescence data.

The sun-solid earth-refracting/absorbing atmosphere geometry and the so-called "heights" of solar illumination are shown in Fig 27. (The depression Θ is defined as the angle of the center of the solar disk below the horizontal at the earth's surface.) "Double standard [atmospheric] refraction" refers to minimum direct illumination, by radiation from the upper limb that has just grazed the hard earth's surface (Ref 21, from which Fig 27 is adapted); that is, the

75
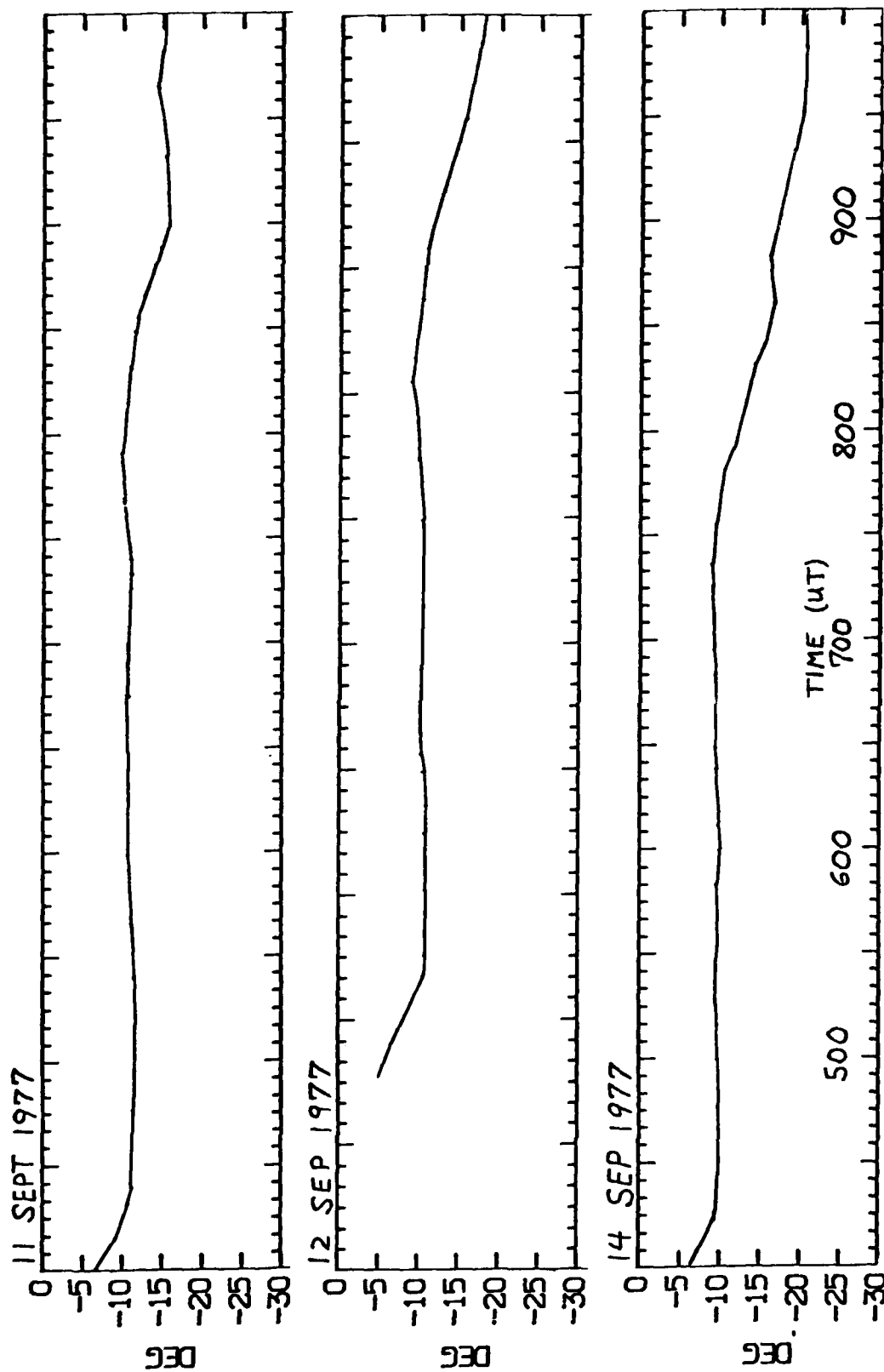
Figure 26. Solar depression angle maintained during three 1977 aircraft data flights from Eielson AFB, AK. Alaska Standard Time = UT −10 hours.

76
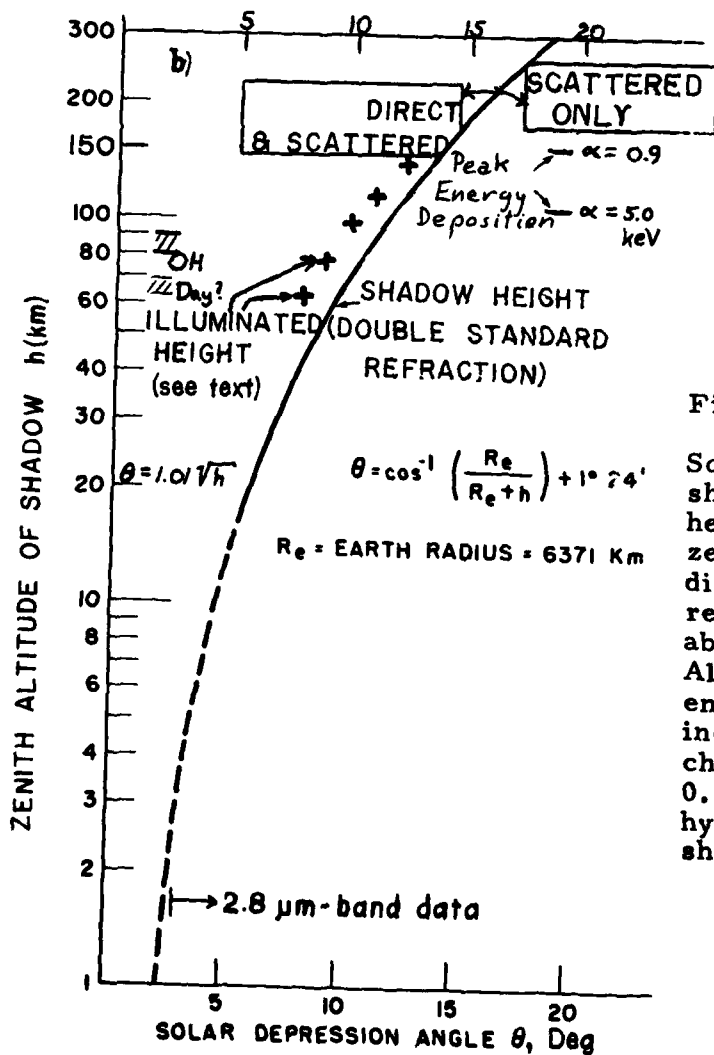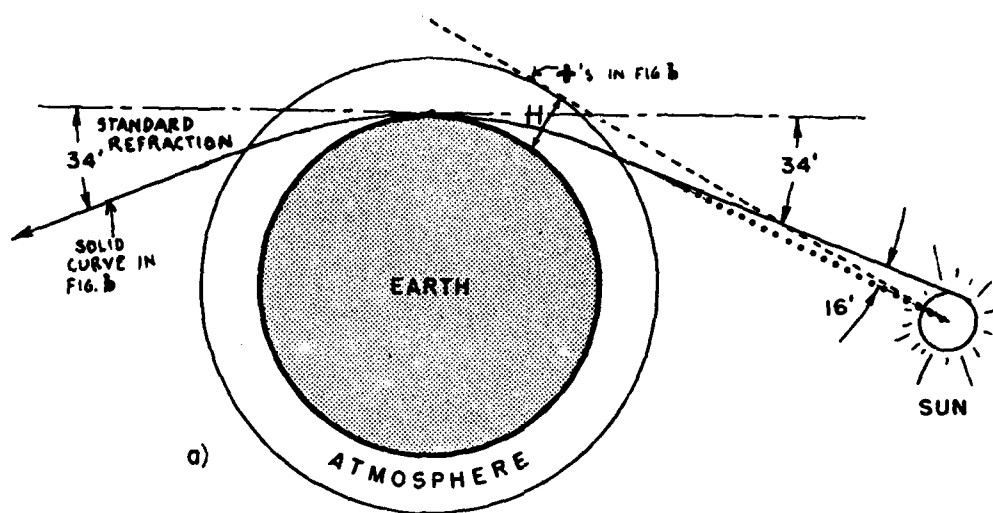
Figure 27

Solar ray paths (a) and shadow and illuminated heights in the observer's zenith (b). Some direct solar radiation reaches all altitudes above the solid line. Altitudes of maximum energy deposition by incoming electrons with characteristic energies 0.9 and 5.0 keV, and of the hydroxyl airglow, are shown.

solid curve in Fig 27 plots the earth's shadow height at the observer's zenith. When $\Theta = 9°$, for example, a small amount of direct irradiation from the limb reaches altitudes as low as 53 km. This strongly-attenuated direct beam would produce an irradiance near its exit point considerably smaller than that from scattered solar photons (recall that the solar disk is dim and red at the horizon; the transmission of the doubly-refracted beam is the square of this small single-path transmission).

The higher-lying series of points marked with +'s give a more appropriate measure of the altitude in the observer's zenith above which solar photons impact ionosphere chemistry. These altitudes, calculated as described below, refer to shorter wavelength radiation from the center of the disk (16 arc min below the limb), which is strongly outscattered by air molecules and/or absorbed by atmospheric ozone. Most of the attenuation occurs within a few km of the point of closest approach to the earth's surface (H in Fig 27). The correction for refraction of the beam decreases as the height of this point increases.

The altitude at which 50% of the ~horizontally-directed photons are transmitted through the 1966 U.S. Standard Atmosphere is 70 km at 2380 Å, 45 km at 3050 Å, and 34 km at 3400 Å (Ref 22). It is worth noting that the difference in this "screening height" in km for rays leaving the top and bottom of the solar disk, is approximately equal to Θ expressed in degrees. The illuminated heights h shown by +'s in Fig 27 were derived by adding a "mean" 50% screening height H = 45 km to the earth's 6371-km radius and neglecting atmospheric refraction ($h = 0.98\,\Theta^2$). Since h changes very slowly with H and thus with wavelength, the results in Fig 27 should apply well into the vacuum ultraviolet.

The interpretation of this numerical relationship $h \approx \Theta^2$ — which is in fact commonly applied in upper-atmospheric investigations — is as follows. At altitudes $\geq$ h a substantial fraction of the solar

78

spectrum down to the short wavelengths expected to influence aero-
chemistry is transmitted to the particle-irradiated atmosphere in
the aircraft's zenith. According to this definition, when $\Theta = 9^\circ$ air
above 79 km is "solar illuminated".

The altitudes of maximum energy deposition when the incoming
electrons' spectral distribution has characteristic energies (as defined
in Appendix II of Ref 5) of 0.9 and 5 keV are marked in Fig 27b.
As the characteristic energy α usually lies within this range –
see Fig 4 of Ref 1 –, most strongly-irradiated air can therefore be
considered solar-illuminated when the solar depression angle is less
than $10\frac{1}{2}^\circ$. The 80-90 km altitude from which the hydroxyl nightglow
arises is also shown; the dayglow is reported (Ref 25) to have a com-
ponent centered at ~ 20 km lower altitude.

RADIANCE BACKGROUNDS

We present here zenith-sky radiance data from the 1977 flights
(Ref 20), selected to provide working measures of the twilight back-
ground against which the aircraft's photometers and radiometers
measure air fluorescence and chemiluminescence. It should be pointed
out that no special effort was made to reconfigure the instruments
to maximize the ratio of particle-excited signal to scattered-
continuum noise. With the help of models of the spectrum and polar-
ization of scattered sunlight these field data can be interpolated to
other wavelength bands, and used to assess the improvement in
signal/background realizable by isolating a single linear polarization
component and narrowing the bandpass of the photosensor to best
isolate the emission feature.

Column energy deposition by ionizing particles is effectively
(and conventionally) measured from the intensity of visible air fluor-
escence, in particular the First Negative bands of N_2^+, in which are
emitted 1/3 of all the collisionally-excited photons at wavelengths
between 3900 Å and 6899 Å. The spectral radiance of the sky from solar
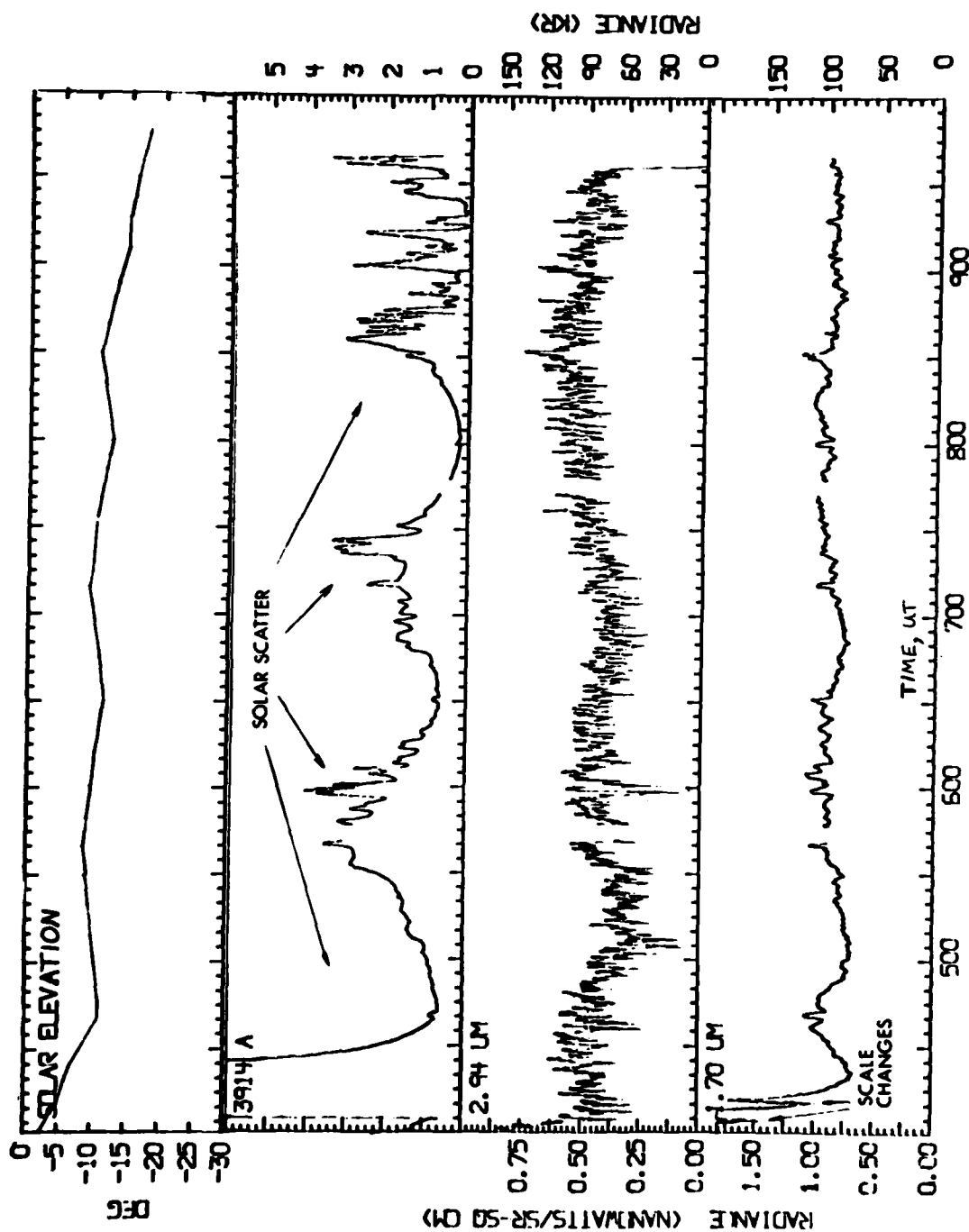
Figure 28. Zenith-sky radiances and solar depressions in the 06 Sep 77 flight.
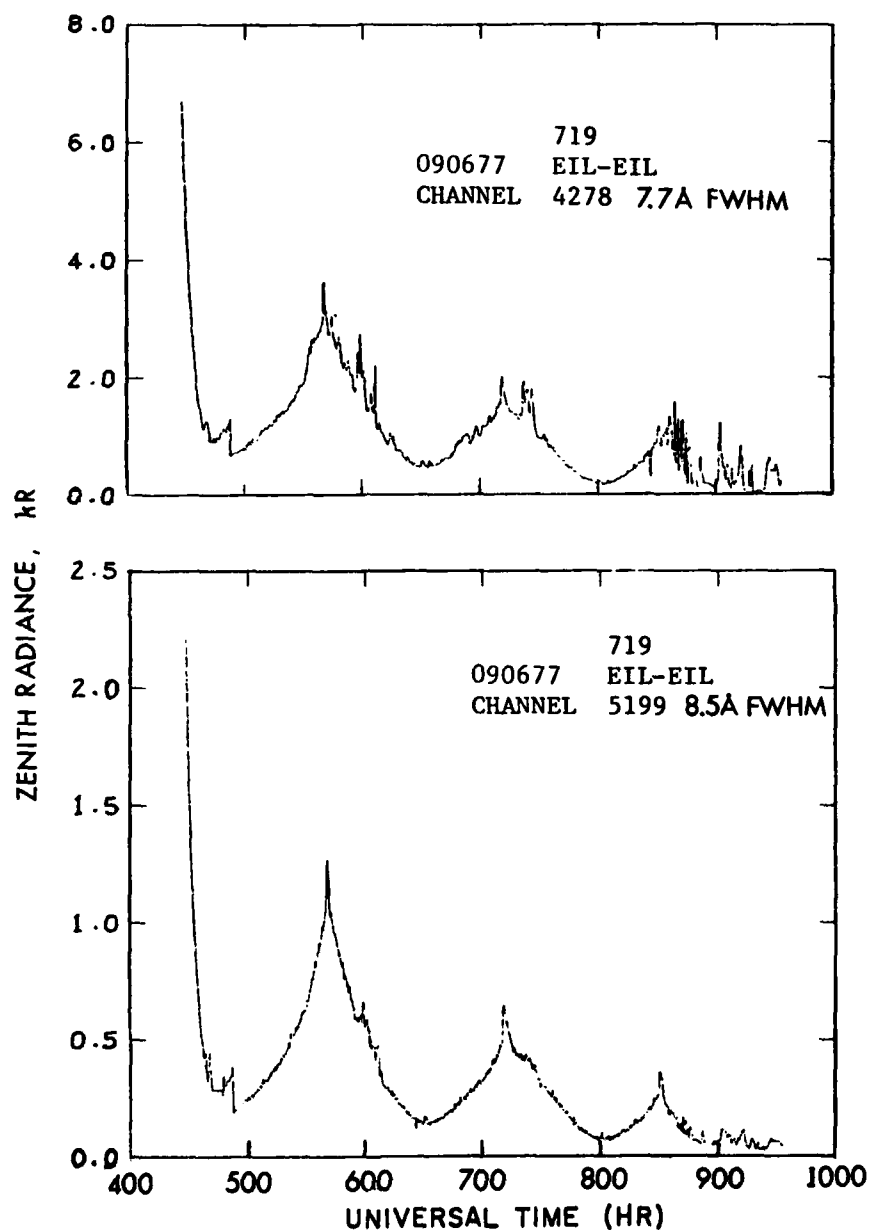
Figure 29. Zenith-sky radiances near 4278 Å and 5199 Å at small solar depressions, measured in the 06 Sep 77 flight. As the filter photometer data are reduced with the assumption that the signal is due only to auroral-feature radiation, the absolute radiance values should not be directly compared.

81

scattering is much greater at these short wavelengths than in the infrared, as the aircraft data in Fig 28 show. Thus at small solar depressions measurements of energy input based on the N_2^+ (0, 0) band with head at 3914 Å or the (0, 1) band at 4278 Å are likely to be subject to larger error than measurements of chemiluminous output in the band centered at 2.9μm or hydroxyl airglow near 1.7μm.

Fig 29 shows zenith radiances measured in narrow bands at 4278 Å and 5199 Å in the same time period by the aircraft's wavelength-cycling photometer (Appendix I of Ref 5), which samples each once per 24 sec. The readings are clearly due to a mix of solar scattering continuum and shorter-period line or band emission. Since the photocurrent data were reduced under the assumption that all the incoming radiation is in the auroral feature (P and R branches of the 4278 Å N_2^+ First Negative band, and 5198.7 - 5200.5 Å NI $^2D - ^4P$ doublet), a simple correction is needed to make the smoothed ordinates in the four peaks quantitatively represent the continuum spectral radiances. Absolute brightnesses of the scattered sunlight between 3466 Å and 6315 Å can be derived from the data in Fig 4 and from the eight other photometer channels (not shown).

Fig 30 compares such zenith-sky continuum radiances measured at 3914 Å (by the aircraft's single-channel photometer) with values at 4000 Å calculated from the theoretical model in Ref 23 (Monte Carlo multiple scattering of 4000 - 7000 Å photons, spherical-shell refracting molecular + ozone atmosphere, zero-albedo earth). The solar spectral irradiance needed for the calculation was taken from Ref 24. The predicted radiances at sea level in a particulate-free atmosphere fit the measured radiances at aircraft altitude very well down to $9°$ solar depression (the angle beyond which no further results from the scattering model are presented, and thus its presumed limit of validity).

A sharp minimum in the sky radiance near 6000 Å (factor of ~ 3 at $6°$ solar depression), which is due to absorption by O_3 in the Chappuis bands, is predicted by the computer model. This minimum

82
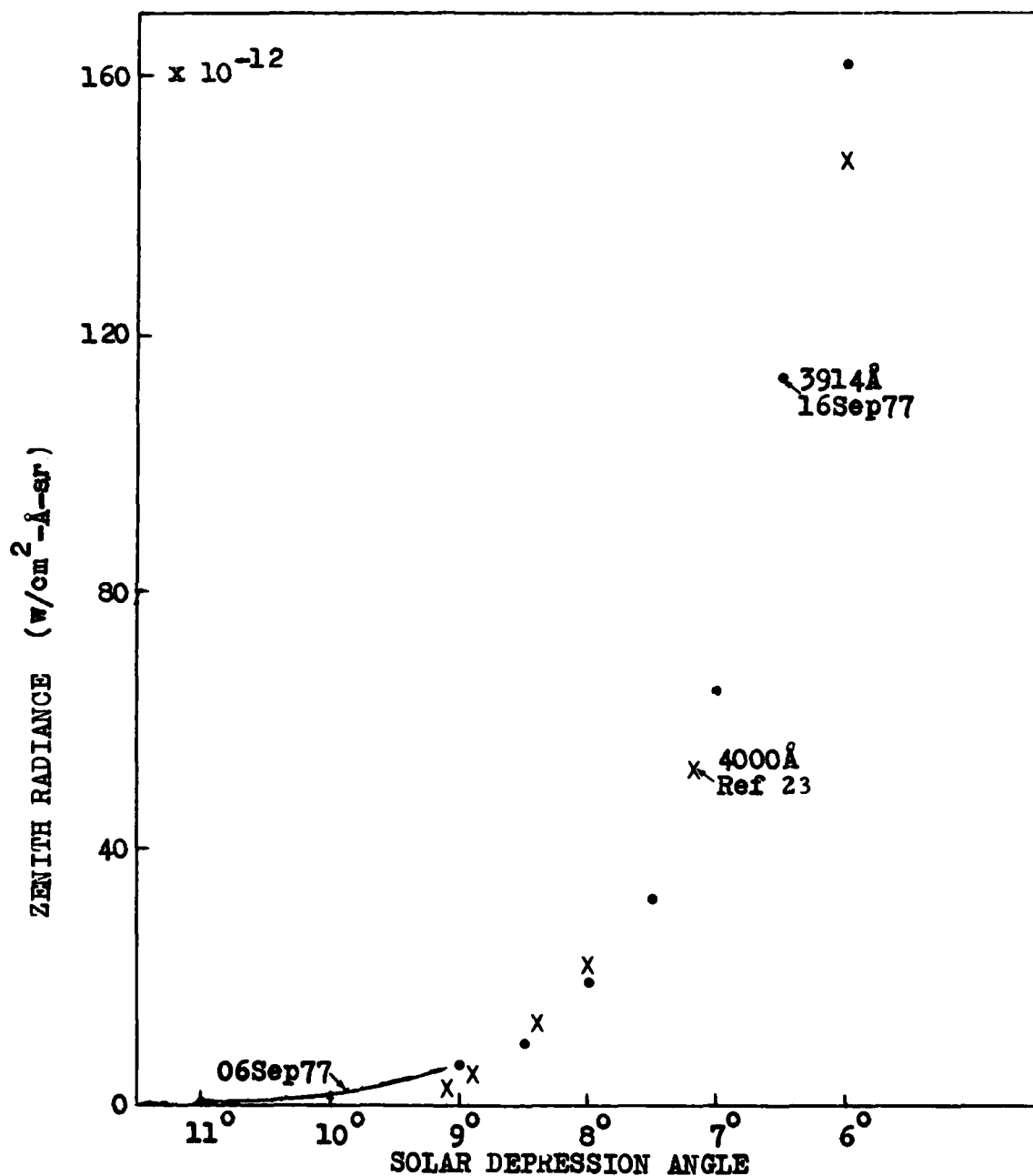
Figure 30. Zenith spectral radiances measured from the aircraft at 3914 Å and predicted (by Ref 23's clear-atmosphere model) from sea level at 4000 Å.
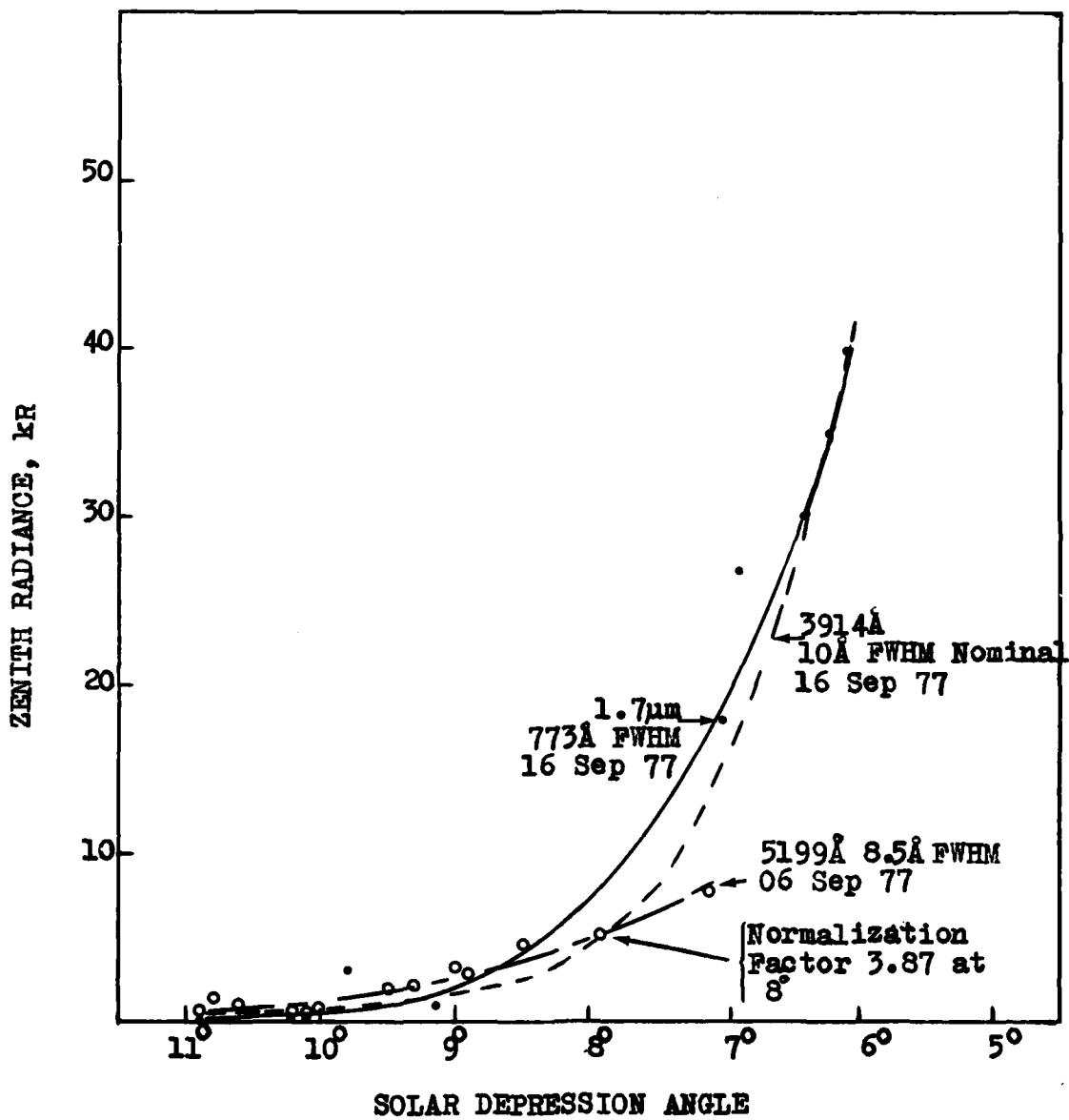
Figure 31. Twilight zenith radiance in bands centered
at 3914 Å, 5199 Å, and 1.7μm.

indicates the strong impact of even weak (< 5%) vertical-column absorption on the twilight radiance. The effect, whose cause is the long horizontal path length of the downward-scattered photons, is likely to be of importance in the short-wavelength infrared, through which extend wings of water and carbon dioxide absorption bands.

Fig 31 compares the dependence on solar depression of the zenith radiances measured by the $1.7003 \pm \frac{1}{2}$ $0.773\mu m$ (FWHM) radiometer and $0.3914 \pm \frac{1}{2}$ $0.001\mu m$ photometer. The radiometer, which is designed to monitor the intensity of airglow in the hydroxyl vibrational overtone sequence, is sensitive to branches of the (5, 3) and (6, 4) bands, with little contamination by air fluorescence. As can be seen from Fig's 28 and 31, this instrument provides useful OH emission data until Θ reaches $6\frac{1}{2}^{\circ}$. At this solar depression the illuminated altitude is well below even the lower hydroxyl-emitting layer reported from the SPIRE limb-scan data (Ref 25).

The spectral sensitivity of the 3914 Å photometer provides useful results to about $7\frac{1}{2}^{\circ}$ depression, where in-scattered sunlight contributes 13 "equivalent" kilorayleighs. As this background usually varies slowly and predictably, 2 - 3 kilorayleighs of air fluorescence can be measured with good accuracy. The error in these particle-energy inputs can be reduced with the help of continuum-radiance data from the 5199 Å photometer (compare Fig's 28 and 29), or better still, from the filter photometer sensitive near 5312 Å, where the air fluorescence component is extremely weak. Experience has shown (Section 1) that 3914 Å fluorescence intensities $\gtrsim$ a few kR accompany adequately high ratios of chemiluminous signal to $\sim$ 100-kR hydroxyl background in the $2.8\mu m$-band radiance data taken from below the two emitting layers.

The low light level video camera (Ref 1), which can be operated with a filter bandpass as low as 20 Å, would be expected to provide useful energy input distribution maps when $\Theta > 8\frac{1}{2}^{\circ}$. Its performance through twilight can be more accurately assessed from the tape records from the 1979 flights.

The model of Ref 23 predicts that the polarization of the scattered light from the vertical is $\geq 90\%$ when $\Theta \lesssim 9°$. Thus a linear polarizer in the optical system would reduce the zenith sky background by a factor somewhat less than 19 while attenuating the unpolarized auroral signal by a factor 2. Isolating a single polarization would decrease the solar depression angle of useful energy-input and hydroxyl background measurements to $5\frac{1}{2}°$ and $5°$ respectively. A polarizer would also improve the twilight video data, as most of the predosing originates within a few degrees of the radiometer's field of view; we estimate that the video system could operate effectively at $\Theta = 6\frac{1}{2}°$.

Despite the broad ozone-absorption minimum in twilight background at longer wavelengths, the N_2^+ 3914 Å band would appear to provide the best discrimination of air fluorescence from aircraft altitude. (Instrument sensitivity varies little over the visible.) No strong molecular band that provides a reliable indication of energy input lies in the region of O_3 absorption, and the OI 5577 Å line is somewhat questionable because of its collisional quenching at the lower auroral altitudes (and has other interpretation difficulties). Quenching and lower photocathode efficiencies make the aurora's near-infrared features — mainly N_2 First Positive and N_2^+ Meinel bands — less effective indicators of energy input at twilight. A further improvement in signal/background in the 3914 Å band results from the local minimum in solar spectral irradiance, which is only $\sim 60\%$ as high as at 4278 Å and 5577 Å (Ref 24).

At $2.83 \pm \frac{1}{2}$ 0.213 μm, no increase in zenith sky radiance was detectable even when Θ was as low as $3\frac{1}{2}°$ (in the 06 Sep 77 mission) or even $3°$ (in a sunrise test flight, 03 Mar 76). At these depressions the aircraft platform itself is directly illuminated by visible sunlight (Fig 27). Since the Rayleigh scattering crossection is very low at this long wavelength a single-scatter model might be expected to predict the zenith radiance, particularly when $\Theta < 6°$ (refer to Fig 11 of Ref 23). However, the atmosphere's attenuation over sections

86

of the radiometer's bandpass would make such a simple calculation unreliable. In any case the issue of 2.8μm scattering background is moot as far as the aircraft platform is concerned, because the smallest solar depression at which SWIR chemiluminescence yield can be reliably measured is determined by errors in the photometrically-measured energy input rates.

CHEMILUMINESCENCE IN THE SUNLIT ATMOSPHERE

We see, then, that the instruments currently on the aircraft can effectively measure particle energy input, hydroxyl fundamental and overtone airglow, and 2.8μm-band chemiluminescence when the radiating air volumes are sunlit.

Principally, these measurements provide a direct simulation of the SWIR background enhancement from daytime nuclear explosions. In a broader sense, the data bear on two infrared sky-background issues: the aeronomy of nitric oxide overtone, and perhaps other, (Ref 26) emissions near 2.8μm following excitation-ionization of air; and the earth limb background in the absence of particle precipitation, which results principally from hydroxyl vibrational emission.

The current models of excitation and quenching of $NO^{\ddagger}$ do not explicitly consider the effect of sunlight, for the reason that neither the concentrations or excitation states of the reacting chemical species are believed to be directly altered by absorption of solar photons. That is to say, laboratory and airglow-aurora investigations have so far identified no effects of photo-excitation in the set of reactions thought to lead to vibrationally excited NO (see, for example, Fig 3 in Appendix I of Ref 1). One way to ensure that no photo-excitation process has been omitted — that is, to "verify" the code model — is to compare directly the daytime and nighttime SWIR yield and characteristic growth and decay time (and when the interferometric spectrometer is installed on the aircraft, the emission spectra).

Changes in composition of the ambient atmosphere represent a second and quite independent potential source of differences in 2.8μm-band emission and correlation with energy input. For example a change in the altitude profile of atomic oxygen has several effects on the atmosphere's effective yield of vibrational radiation from NO, as

- $NO^{\ddagger}$ is quenched by O [or radiates]
  (Section 3)

- N^2D is quenched by O [or reacts with O_2 to form $NO^{\ddagger}$]

- N_2^+ reacts with O (to produce N^2D) [or with O_2, in which case no N^2D atom enters the reaction chain]

- $N_2 (A^3\Sigma)$ reacts with O (perhaps to produce $NO^{\ddagger}$)[or with NO (perhaps to excite NO (A), which radiates to produce $NO(X)^{\ddagger}$, or radiates (principally)].

(- In addition, $N_2^{\ddagger}$ reacts with O^+ to produce N^2D + NO^+ (which usually results in a second N^2D atom [or with O, O_2, and CO_2].)

Although photochemical reactions cause only a small diurnal variation in the O-atom concentration in the lower thermosphere, some changes due to turbulent and diffusive mixing are expected to occur (Ref 27). (The [O] profile of course also varies with latitude, K_p, solar cycle, and other geophysical parameters.) The OPTIR/QCHEM aeronomy code maintains a library of model atmospheres. Should calculations employing plausible models of ambient species concentrations fail to fit the daytime measurements, a deficiency in the aerochemical code is implied.

The $\underline{OH}^{\ddagger}$ vibrational-fundamental airglow dominates the earth's limb background near 2.8μm at tangent altitudes above ~ 30 km by

night and ~60 km by day. Atmospheric nuclear bursts excite gravity waves that alter the spatial radiance structure of the emitting hydroxyl layer(s), both directly and by enhancing the downward advection of O atoms (which attach to O_2 to form O_3, which in turn reacts with H to produce $OH^{\ddagger}$). Aircraft measurements provide an opportunity to determine the natural variability and structure of the daytime OH-fundamental SWIR background, much of its emission spectrum, and its twilight-transition properties (which provide critical information on the excitation-deexcitation mechanisms).

SUMMARY

Air at altitudes at which auroral electrons deposit energy can be considered sunlight-illuminated when the solar depression angle is less than $10\frac{1}{2}^{\circ}$, and the hydroxyl airglow layer(s) when it is below 8°. AFGL's present NKC-135 aircraft instruments are capable of measuring zenith column energy input rates with good (signal)/ (scattered-light noise) when the solar depression is greater than $7\frac{1}{2}^{\circ}$, and hydroxyl overtone emission when it is above $6\frac{1}{2}^{\circ}$. Atmospheric-scattering theory indicates that these limiting depression angles could be lowered about $1\frac{1}{2}^{\circ}$ by linear polarizers in the photometer and radiometer optical systems. However, since the sky background radiances increase very strongly with solar elevation (Fig's 30 and 31), tailoring of instrument passbands is unlikely to result in substantial further improvement. Chemiluminescence near 2.8μm in the hydroxyl fundamental, nitric oxide overtone, and whatever other molecular band systems may be excited in the upper atmosphere, is readily measurable even at solar depressions as low as $3\frac{1}{2}^{\circ}$.

Column intensities (and spectra) of these radiations from the sunlit high atmosphere can be measured over the period of hours that the aircraft has been shown to be able to hold the auroral-latitude solar elevation within the necessary few degrees.

Unfortunately, particle precipitation was too weak during such measurement periods in 1977 to result in useful SWIR chemiluminescence data; the records from flights in 1979 are not yet ready for assessment. Direct comparison of daytime and nighttime infrared yields, grow-in and decay times after particle irradiation, and spectra would serve to validate the current aerochemical models' implicit assumption that sunlight (or bomblight) photons play no part in the processes that produce vibrationally-excited NO molecules. In addition the daytime and twilight-transition spectral radiance and natural spatial-temporal structure of the OH airglow, which in the absence of particle precipitation is the dominant earth-limb background in the 2.8μm band, can be systematically determined from the aircraft platform.

SECTION 6

2.7μm-BAND RADIATION PROFILES ON UPLEG OF A18.219-1

INTRODUCTION

We document here the altitude profiles in the 2.43 - 3.11μm (FWHM) wavelen_th band from the side-viewing radiometer on upleg of ICECAP multi-instrumented rocket A18.219-1 (25 Feb 74). These data have not been previously addressed because they are noisy below 92 and (at some azimuths) above ~105 km, and are less correlated with the simultaneously-measured air fluorescence than the similar azimuth-elevation scan data from downleg (Ref 5). A description of the auroral ionosphere into which the rocket was launched appears in Section II, and a set of all-sky photographs in Section III, of Ref 5 ; the major features were an IBC III arc some 75 km north of Poker Flat and an IBC II arc near the Poker zenith (Fig 27 of Ref 1).

Our earlier evaluation of the 2.7μm downleg radiances showed that they had reasonably good average correlation with the 3914 Å fluorescent intensity. From the slope of the best-fit line we derived a mean energy efficiency of 0.6% (assuming the radiation to be the nitric oxide overtone sequence with an "AFGL" vibrational distribution). This chemiluminous yield is consistent with those from the aircraft radiometry data (Section 1). On upleg the photon ratios and apparent efficiencies are considerably higher, as we will show. Some of the excess SWIR signal toward the north may be related to the artefact that eventually causes the intense off-scale spike near 340° geo-magnetic azimuth (above 111 km rocket altitude), whose properties are described in Section 4 Ref 1.

SIDELOOKING ALTITUDE PROFILES

Altitude profiles of 2.7μm- and 3914 Å-band column intensities at 30° azimuth intervals are plotted in Fig 32 . The azimuths have been corrected for the 90° shift identified in Section I of Ref 6.

91
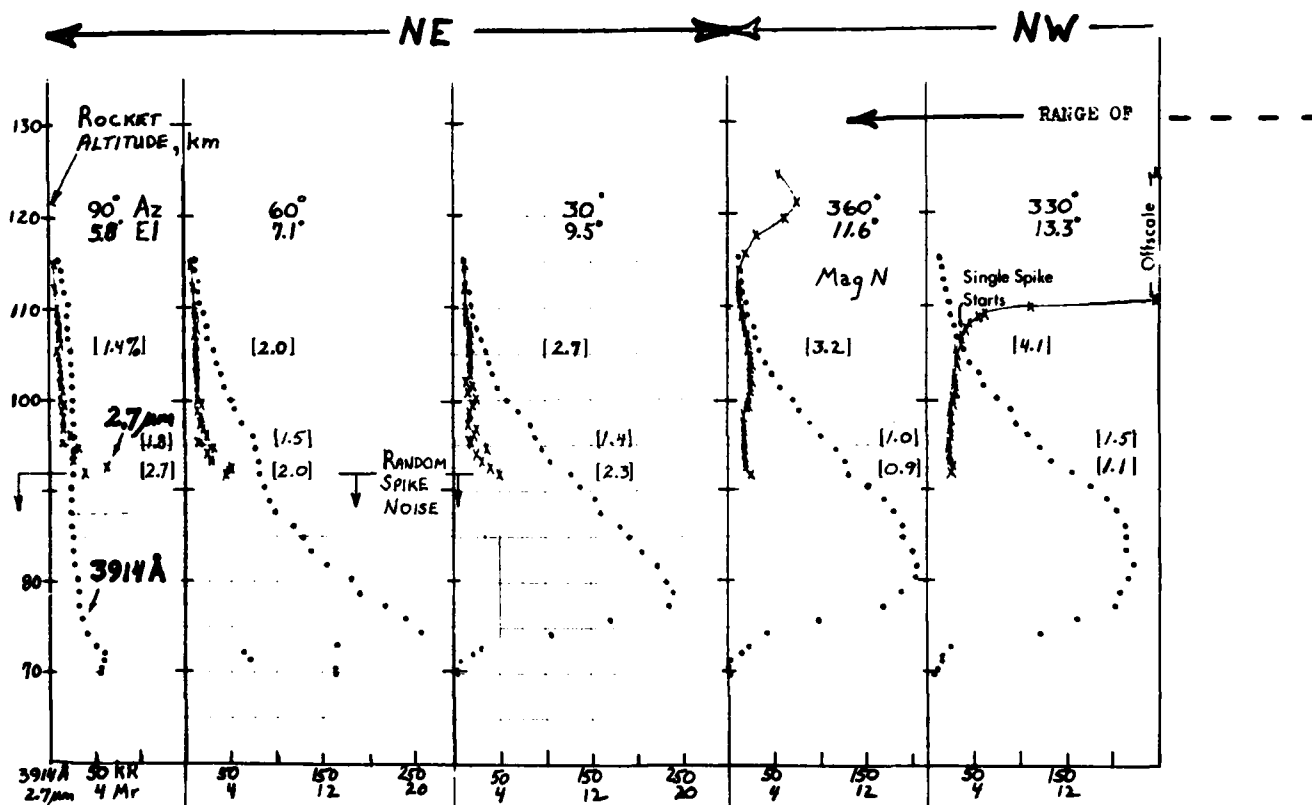
Figure 32. Altitude profiles of 2.7μm and 3914 Å-band radiances measured at 30° intervals on upleg of A18.219-1. The bracketed numbers refer to apparent yields of NO overtone radiation at 105, 96, and 92 km (no background correction has been applied).

Up to 92 km the 2.7μm data trace has numerous erratic narrow (~10° az) noise spikes similar to those superposed on the 4.3μm radiometer traces (Section 4 of Ref 1). We have not attempted to plot radiances below this altitude, as the cumulative effect of these closely-packed pulses is to raise the baseline. The dependence on altitude of the azimuthal distribution of 3914 Å radiance is similar to that measured by other ICECAP multi-instrumented rockets; that is, the trace from the coaligned air fluorescence photometer is shaped

AD-A089 724   PHOTOMETRICS INC LEXINGTON MA   F/G 4/1
                FURTHER ASSESSMENT OF INFRARED DATA FROM AIRCRAFT AND ROCKET PR--ETC(U)
                NOV 79   I L KOFSKY, D P VILLANUCCI   DNA001-79-C-0013
UNCLASSIFIED   PHM-05-79   DNA-5127F   NL

END
DATE
FILMED
11-80
DTIC

MICROCOPY RESOLUTION TEST CHART

NATIONAL BUREAU OF STANDARDS-1963-A

SW   SE

SPIKE AZIMUTHS ⟶

300°   270°   240°   210°   180°   150°   120°
14.5°   13.3°   12.5°   10.8°   8.2°   6.3°   5.5°

[7.2]   [14.7]   [8.5]   [2.6]   [2.2]   [2.0]   [1.7]

[1.4]   [8.2]   [4.2]   [3.4]   [3.9]   [4.7]   [2.8]
[1.5]   [3.1]   [6.7]   [6.2]   [7.2]   [8.8]   [5.7]

SCALE
CHANGE

50 RR 150 250   50   150   10   30   10   30   10   30   10   30   10
4 Mr   12   20   4   12   4   12   4   12   4   12   4   12   4
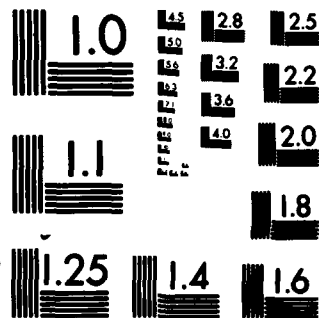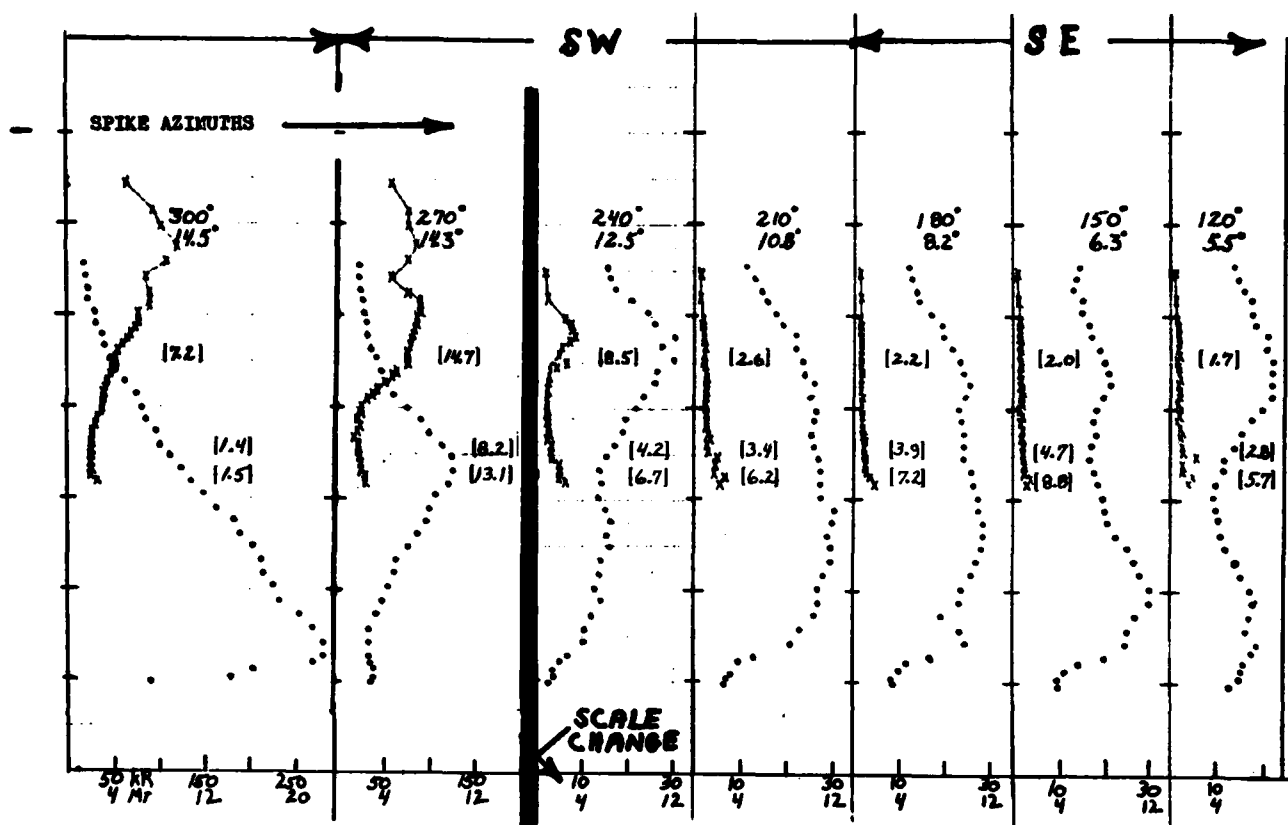
Figure 32 (continued)

like previous such traces and is consistent with the ground based
photometry of the auroral distribution.

Above 92 km the SWIR emission shows some tendency to follow
the energy input. As the radiometer's field sweeps toward 330°,
spurious emission from a visible light-absorbing object overlies the
2.7μm signal above ~ 105 km rocket altitude, and saturates it above
110 km (see Fig 22 of Ref 1). The less intense "skirt" of
the strong 30°-wide pulse is detectable between about 270° and 360°
in azimuth. This north-lying artefact remains present in the scans almost
up to apogee.

Energy efficiencies derived from the column intensity ratios at
92, 96, and 105 km rocket altitude (again taking vibrationally excited

93

NO as the only emitting species) are shown in brackets on Fig 32.
No adjustment has been made to the data except for a correction for
the small (~12%) fraction of NO overtone sequence at wavelengths
longward of the radiometer's bandpass (Section II of Ref 5). These
SWIR-band efficiencies are 2 to 20 times higher than the average
measured on downleg, even in directions away from the radiating
artefact (that is, toward the south).

DISCUSSION

The 2.7μm-band altitude profiles on upleg are much less
correlated with the simultaneously-measured power inputs than on down-
leg, and the apparent yields are all well above the currently-accepted
"equilibrium" value. These photon ratios are unexpectedly high even
in directions away from the data-contaminating object, as Fig 32
shows. The high readings are more consistent with a change in
sensitivity of the radiometer than with a dc offset, as the signal level
on upleg becomes as low as that on downleg at altitudes above about
140 km. In any case, as is brought out in Fig 32, the 2.7μm data
set from upleg of A18.219-1 has so much internal inconsistency that
little or no confidence can be placed in the apparent SWIR chemilumin-
escence efficiencies.

SECTION 7

PRELIMINARY REPORT ON AIRCRAFT MEASUREMENTS OF OPTICAL/IR AFTERGLOWS FROM A MAJOR IONOSPHERE PERTURBATION

PURPOSE

The Atlas-Centaur rocket that launched NASA's High Energy Astrophysical Observatory-C on 20 Sep 79 exhausted 15 tons of H_2O and H_2 at altitudes between 212 and 501 km. These molecules caused a sharp reduction in the F-region's electron density over hundreds of km perpendicular to the 1900-km release trail, as had been previously observed (Ref's 28,29) and expected (Ref's 30, 31,32,33). Ref 34 reviews briefly the phenomenology of such injections of species that react rapidly with the upper atmosphere's O^+ ions, and gives data on HEAO-C's launch window and trajectory and an outline of the planned program of diagnostic measurements. A series of similar but smaller releases of reactive gases over ionosphere observatories from Space Shuttle is planned (Ref 35).

In early 1976 PhotoMetrics pointed out (Ref 36) that these large "holes" might be unstable against developing spatial irregularities of the scale that degrades performance of satellite communication links by causing signal phase and amplitude scintillations. Therefore molecular gas releases, much like the electron-overdense barium-ion clouds of DNA's STRESS program, could provide simulataion data on the dynamics of formation and decay of such F-region irregularities, which also are expected to be generated by atmospheric nuclear explosions. This issue has since received considerable theoretical attention, and in fact one DNA-sponsored code model (Ref 37) predicts that the large-scale disruption of the ionosphere's vertical density distribution will result in small-scale spatial structure when the geomagnetic field's direction is perpendicular to the buoyant rise of the electron-underdense region (that is, near the magnetic equator).

Characterization of any plasma inhomogeneity structure that
might develop was therefore one major goal of the optical measure-
ments on the depletion region that we planned from the AFGL/DNA
aircraft, NKC-135 55-3120. The ionosphere hole has several other
effects on radiowave – in particular, HF – and radar propagation
(Ref 30),interpretation of which is facilitated by images of the after-
glow (which, as we will show, "map" the recombination radiation).
In a larger sense, the aircraft measurements were intended to in-
vestigate the chemical and diffusive processes governing the dynamics
of the disturbed F-region, and to determine rate coefficients for re-
actions that result in loss of free electrons and emission of optical/IR
sky background radiations.

TECHNICAL BACKGROUND

Release into the ionosphere of H_2 and H_2O molecules initiates
a rapid ($\sim$ min) reduction of electron density by converting what is
essentially an atomic ion plasma (consisting of O^+ and e) to a mole-
cular ion plasma (OH^+, H_2O^+, H_3O^+ and e), which is able to re-
combine by two-body – two-body reactions.

Deionization in the undisturbed nighttime F region proceeds
by 1) O^+ charge transfer to O_2 (slow, the rate-limiting step) followed
by 2) electron dissociative recombination with the O_2^+ ions (fast, ~ 10
sec). This latter reaction excites some of the product oxygen atoms to the
two metastable states of the ground configuration, resulting in a natural
airglow intensity of about 1/10 kR in the $^1D \rightarrow {}^3P$ red doublet. H_2 and H_2O
molecules have about 100X greater rate coefficient than O_2 for reaction with O^+,
so that wherever their concentration is greater than 1/100 that of O_2,
most of the positive charge resides on species such as HO^+ and H_2O^+
(Ref's 30, 38). As these molecular ions' rate coefficient for dissociative
recombination is sensibly the same as that of O_2^+, even a moderate
probability of population of radiative excited states of the product
atoms (or molecular fragments) would result in enhanced airglow.

96

Representing this process schematically (with some simplification),

— O^+ AND E ARE MAJOR CONSTITUENTS OF THE AMBIENT IONOSPHERE

— H_2 AND H_2O ARE INPUT FROM THE CENTAUR ENGINE EXHAUST

$$H_2 + O^+ \longrightarrow H + OH^+, \text{ THEN}$$

$$OH^+ + E \longrightarrow H + \begin{array}{l} O^1S \xrightarrow{\frac{1}{2} SEC} O^1D + \underline{\text{GREEN LINE}} \ h\nu \\ O^1D \xrightarrow{100 \ SEC} \underline{\text{RED LINE}} \ h\nu + O^3P \end{array}$$

$$H_2O + O^+ \longrightarrow O + H_2O^+, \text{ THEN}$$

$$H_2O^+ + E \longrightarrow H + OH^{*,\ddagger} \longrightarrow \begin{array}{l} \text{VIBRATIONAL AND/OR} \\ \text{ELECTRONIC BANDS} \ h\nu \end{array}$$
$$ \longrightarrow O^*?$$
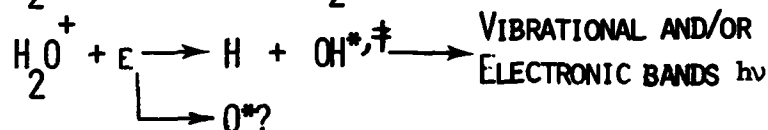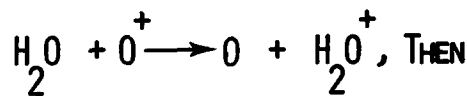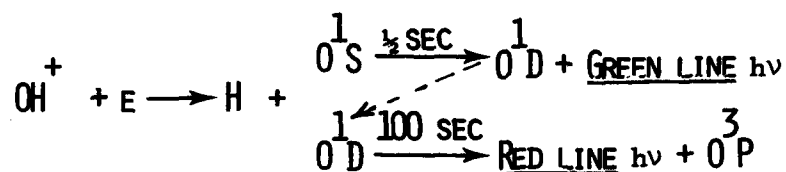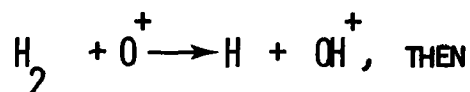
Two major enhancements are expected, in the OI forbidden lines and in hydroxyl bands. The maximum zenith column intensity of the oxygen red line was predicted to be about 1 kR (Ref's 31, 32).

As dissociative recombination of H_2O^+ is about $7\frac{1}{2}$ eV exothermic, the $A^2\Sigma^+$ electronic state of OH is energetically accessible. This is the upper state of the well-known A-X system; under various laboratory conditions its (0,0) transition longward of 3064 Å is the most intense in the sequence, which has numerous other bands between about 3460 Å and 2444 Å (Ref 39). Since none of the aircraft instruments are sensitive at wavelengths near the stratospheric ozone cutoff at ~3050 Å, no measurements of electronic excitation of OH could be made. Additionally, population of vibrational states above those from which the Meinel-band nightglow arises was predicted (Ref 32), and OH (10,4)

band emission is thought to have been detected following the 1977 Lagopedo F-region release (Ref 29). The response of the aircraft's photometer and radiometers to hydroxyl vibrational radiation is discussed later in this Section.

COORDINATING MEASUREMENTS

For orientation, we review briefly the other diagnostics of the ionosphere disturbance produced by the Centaur upper stage burn. Preliminary results of the various measurements were presented at a workshop held at North Andover, MA on 12-13 Nov 79 under sponsorship of the U.S. Department of Energy (Solar Power Systems Office, Argonne National Laboratory; the field program was organized by M. Mendillo of Boston University). Fig 33 shows the trajectory of the rocket from Kennedy Space Center, FL, and of the aircraft; the direction from ground receivers (operated by Stanford University, SRI International, Naval Research Laboratory, Air Force Geophysics Laboratory, Boston University, U.S. Army Electronics Command, and other cooperating groups) to VHF beacons on five geosynchronous satellites;and the two incoherent-scatter radars (Millstone Hill and Arecibo). The HF links monitored and the ground optical stations are discussed later in the text.

The most extensive series of measurements of the plasma depletion was made by a network of polarimeters, which determine by Faraday rotation the total electron-column content along lines of sight to satellite beacons. A total of ten units was deployed between $25\frac{1}{2}^{\circ}$ and 31° N latitude along the Florida-Georgia coast (pointing toward the Italian communications satellite Sirio at 14.77°W, 0.07°S,transmitting at 136.140 MHz) and in Bermuda (pointing toward two of the four U.S. beacons shown; two doppler receivers were operating at 250 MHz). These compose low-resolution, 1-dimensional "images" of the volume densities projected onto a line near the meridian direction or converging toward the Bermuda station. All-sky camera
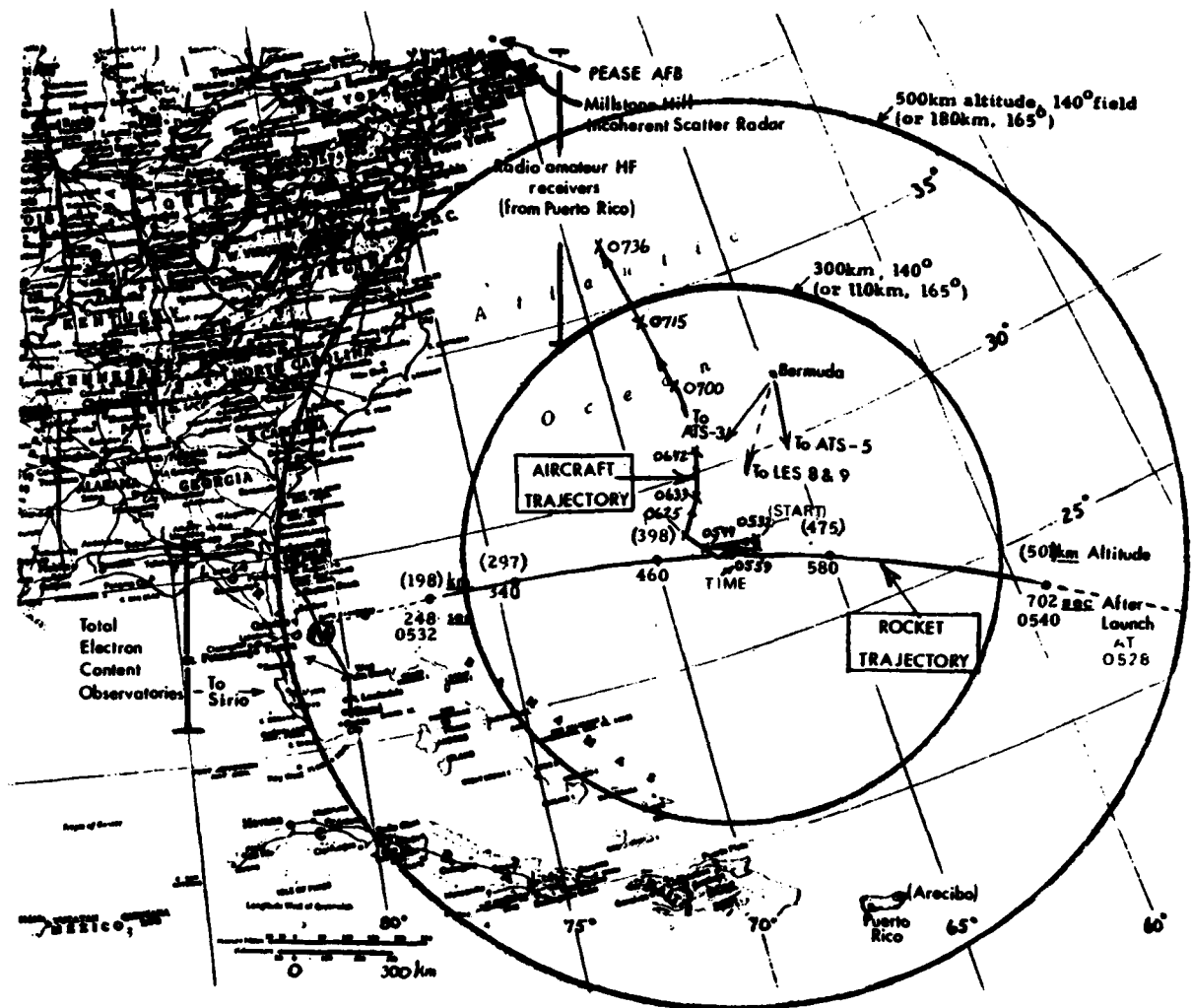
Figure 33. Plan view of flight trajectories of the Centaur rocket and NKC-135 55-3120. H_2 and H_2O are exhausted over the section of trajectory drawn as a solid line. The large circles show the horizontal range to the intercept of the all-sky camera's 165° field (or 140° segment of field) at the altitudes indicated, corrected for earth curvature. Also shown are the directions to five radio beacons in geosynchronous orbit from polarimeters (total line-of-sight electron content meters) in Florida and Bermuda. HF paths between Puerto Rico and amateur receiver sations in the northeast US, would involve ionosphere reflection in the depleted volume. The optical site at Melbourne, FL is marked with a circled M.

views of the airglow from below represent complementary high-spatial-resolution, 2-D projections of the column rates of destruction of free electrons in reactions with OH^+ (and perhaps H_2O^+).

Those polarimeters directed within ~200 km of the rocket trajectory measured about factor-of-four decreases in the ionosphere's total electron content, which developed within a few min and persisted until at least 1 hr before dawn. The location, amplitude, and dimensions of the ionospheric hole were confirmed by differential doppler measurements (by a University of Texas group), which use transmissions from low-orbit satellites. The onset of restoration of the F-layer's electron density before it becomes illuminated by the sun, observed from two of the stations, is not understood.

A larger volume depletion (factor-of-ten) near the F-region peak was measured by MIT's Millstone Hill incoherent-scatter radar, which is capable of scanning to within a few degrees of the horizon. No clear effect of the release was observed by the Arecibo radar, which can scan only as far as 20° from its zenith. Some fading was observed at HF links (six frequencies were beamed to radio amateurs from Puerto Rico, and various DoD communication links were monitored), although the effects were by no means pronounced in comparison to those produced by natural variations in the ionosphere.

Optical data other than those from the aircraft are extremely sparse. A station on the South Carolina coast (Marshall Space Flight Center) was clouded in, clouds severely hampered attempts to measure toward the north from Arecibo Observatory, and a video system at Arecibo (Boston College) failed. Los Alamos Scientific Laboratory operated commercially-available instruments at a ground station at Patrick AFB, FL (Melbourne, 28.0°N; see Fig 33). The Pritchard filter photometer, video camera (unfiltered, and without means for recording the signal), and Spex spectrometer did not have sufficient sensitivity to measure pre-launch background sky radiances. The photometer, whose elevation angle was changed several times

while the 6300 Å airglow intensity was above threshold, recorded a maximum of 20 kR along a slant path at $21\frac{1}{2}°$. No sky brightness increase was detectable on the video monitor. Spectrum scans at wavelengths above 6200 Å showed only the OI 6300-6364 Å doublet (no hydroxyl emission was above system noise). As is frequently the case, the AFGL/DNA aircraft-observatory, with its capability for flying above atmospheric clouds and water vapor at a favorable location, and with its state-of-the-art instruments, returned far more useful optical/IR data than all these other projects combined.

AIRCRAFT OPERATIONS

HEAO-C's launch window lay within a moon-down period during which the aircraft was being used to measure SWIR emission from the sunlit auroral ionosphere (Section 5), in flights based at Pease AFB, NH. The flight coordinator was kept informed about readiness by Kennedy Space Center, who provided 2 days' firm notice that launch had been scheduled for 20 September. Diversion of one mission for measurements on the large-scale ionosphere disturbance resulted in only minimal interference with the SWIR structure-sources program.

A flight profile that called for 1.8 hr of measurements along a single back-and-forth track close to the release trail had been prepared and filed. The coordinator was informed by KSC Range Safety 36 hr before the mission that the aircraft would be restricted to a "box" just north of the rocket trajectory between 66° and 68° W longitude (see Fig 33). The effect of this change of plan is that the instruments sampled more frequently along a narrower segment of the depletion region. Actual takeoff from Pease was at 0235 UT, arrival on station at 0458, and departure from the "box" near 0625. The instruments, which are those used in the auroral-SWIR program with the changes in the 12-channel photometer described below, were operated throughout the period when the aircraft was at flight altitude.

10° Field
IR RADIOMETER
1.27 μm $O_2{}^1\Delta$
1.70 μm $OH_{\Delta v}=2$

2° Field
PHOTOMETER
6300Å OI
5577Å OI
7000-8500 Å OH
6700 Å OH (10,4)
+5 others

0.4° Field
IR RADIOMETER
2.9 μm $OH_{\Delta v}=1$,
5577Å OI,
& 3914 Å

20° Field CAMERA

165° Field CAMERA
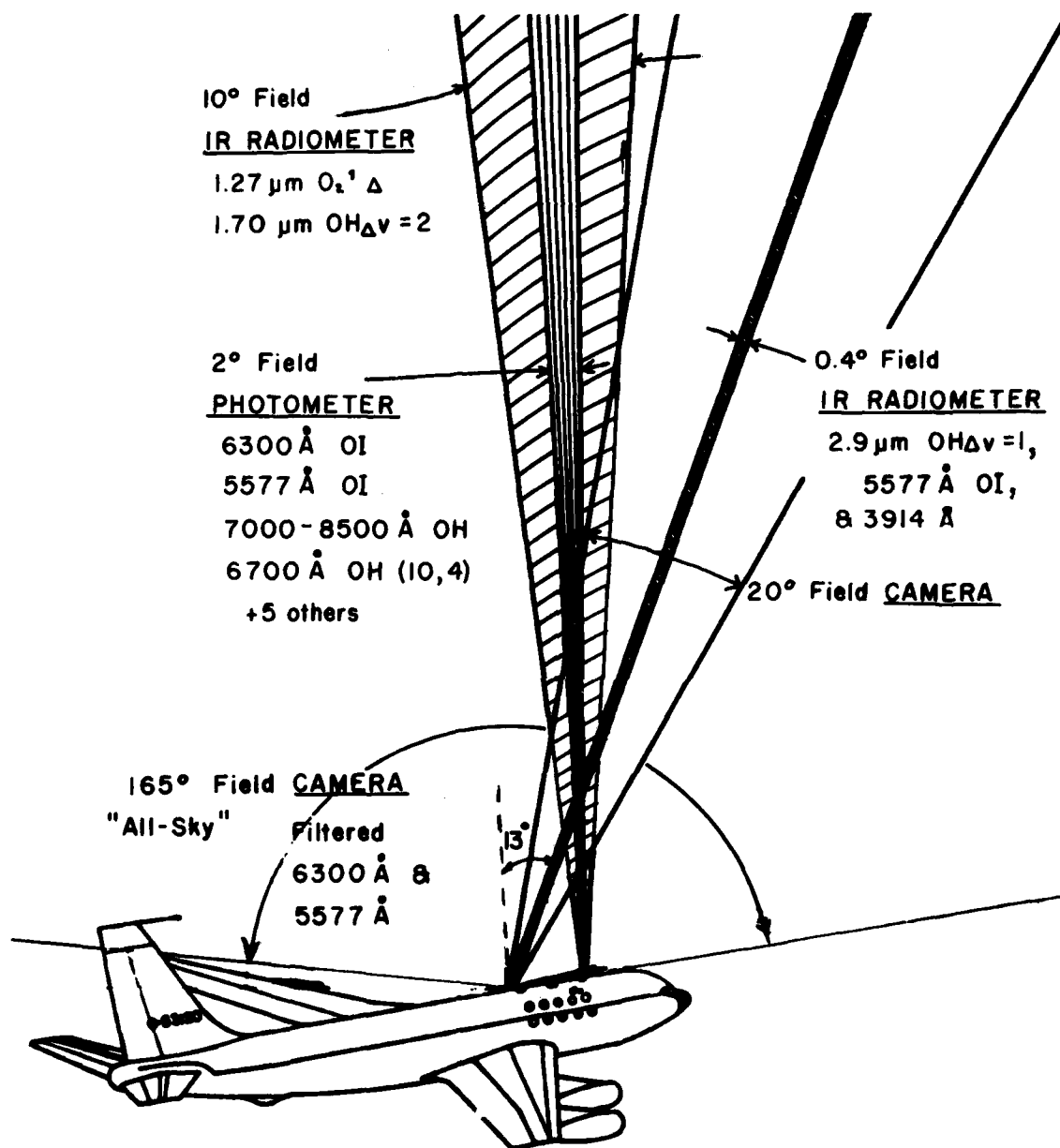"All-Sky"   Filtered
6300Å &
5577 Å

13°

Figure 34. Instrument fields of view and wavelengths
for measurements of afterglows from the
Centaur exhaust gas release. All field
centers are on the aircraft's longitudinal
axis.

The instrument fields and nominal emission features measured (Ref 1) are shown in Fig 34. No changes were made in the SWIR radiometers or in the low light level video camera, which is capable of imaging the glow with 20 Å wavelength isolation at 6300 Å and 5577 Å, and in a ~ 1000 Å "fluorescence" band below ~ 4700 Å. The 1.7μm radiometer is sensitive to the P and Q branches of the (5, 3) and the R branch of the (6, 4) OH Meinel bands, and the 2.9μm radiometer to the P of (1, 0), all the (2, 1), and the R and Q of (3, 2).

The sensitivity of the photometer is shown against a mean night-glow spectrum (Ref 40) in Fig 35. Three of its interference filters were replaced to permit measurement of hydroxyl airglow:

- FWHM 6667-6762 Å, OH (10, 4) band;

- FWHM 7100-7900 Å (Wratten 89B filter + S-20 response of photocathode), OH Meinel bands as shown;

- FWHM 6425-6435 Å background monitor, negligible OH emission in bands originating from vibrational states $\leq$ 9.

These photometer channels have not yet been absolutely calibrated, as insufficient time was available between procurement of the new filters and the start of the series of flights. Note that the photometer measures transitions from high and intermediate vibrational states of OH, the 1.7μm radiometer from the 5th and 6th states, and the 2.9μm radiometer from the three lowest states.

No pre-event estimate of the column rate of vibrational excitation of hydroxyl was available. The zenith intensity in each of the Meinel fundamental and overtone bands excited in the mesosphere is of the order of about 100 kR (10^{11} photons /cm^2 col sec), and the nightglow in transitions in which the vibrational quantum number changes by 4 and 5 is in Fig 35. Bands originating from the tenth and higher states, for example the (10, 4), would be measured against a generally lower background. The (10, 8) band, which is ~ 10^2 more intense, lies near 2.33μm;

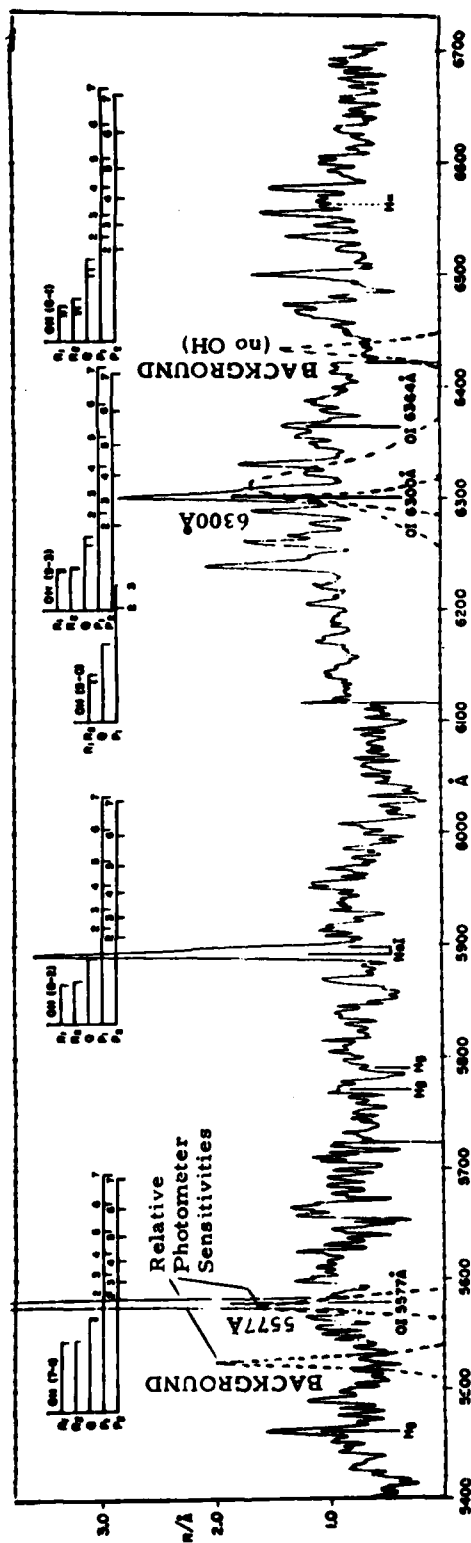Figure 35. Spectral sensitivity of the aircraft photometer normalized to the nightglow spectrum from Ref 40. The locations of the rotational lines of the (10,4) hydroxyl vibrational band are tentative. In addition to those shown, the photometer has 10 Å channels measuring the $N^2D - ^4S$ doublet at 5199 Å, continuum at 5310 Å, and N_2^+ First Negative (0,1) band at 4278 Å.

104
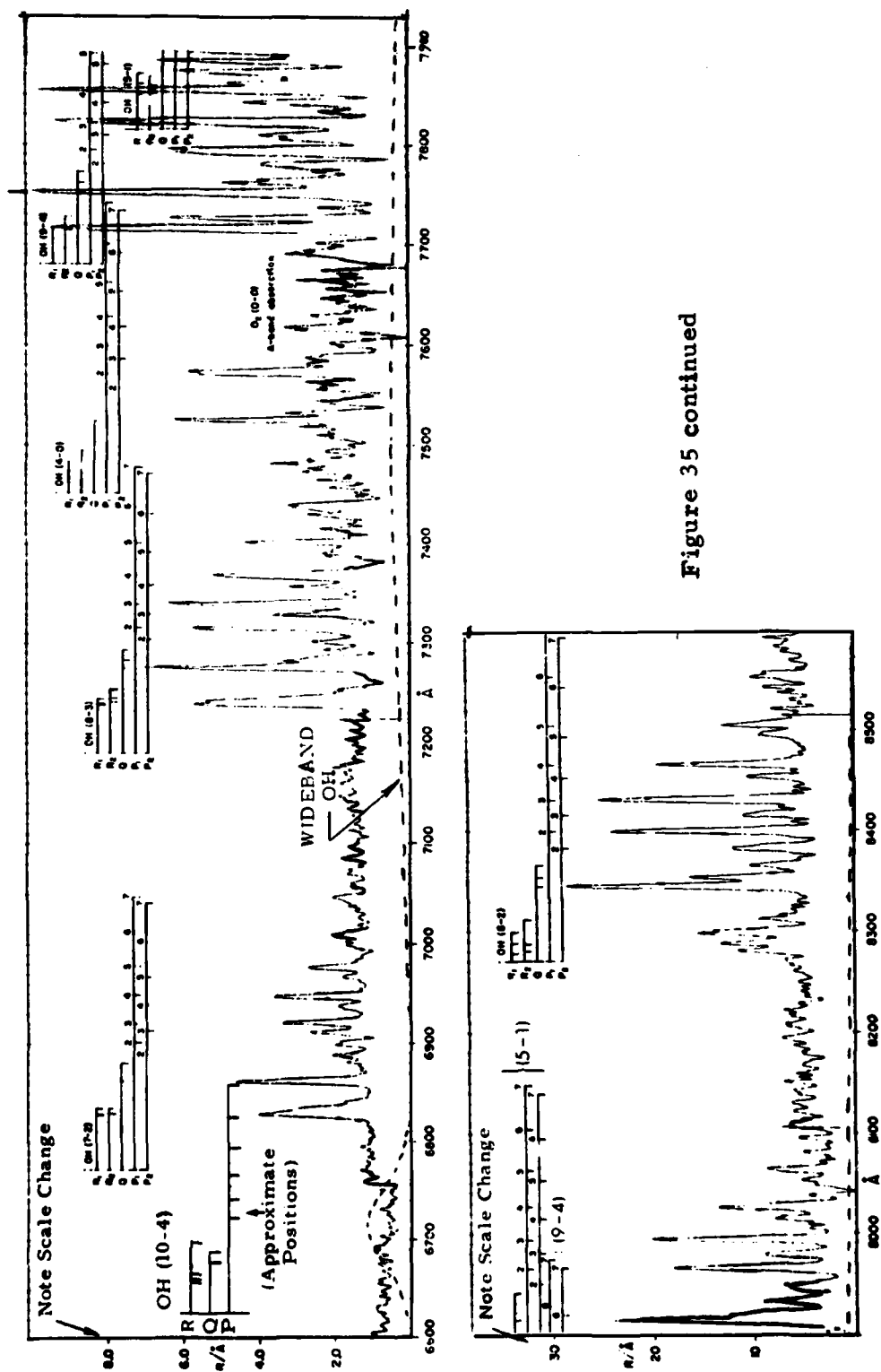
Figure 35 continued

105

and the (10,9), weaker than (10,8) because of the OH radical's anharmonicity, near 4.8μm.

RESULTS

The <u>video camera</u> recorded high-signal/noise all-sky images of the 6300 Å afterglow for at least 1 hr after the rocket was launched at 0528. The early glow was also detectable on the monitor in 5577 Å, but not in the wideband fluorescence channel. None of the aircraft observers was able to resolve visually this increase in sky radiance.

Fig 36 is an overview of the development of the red afterglow. A small patch comes into the camera's field from the west, expands north-south, passes the aircraft zenith (toward which the photometers point), and eventually grows to cover most of the all-sky frame. The conventional explanation of the broad sky brightness minimum surrounding its centerline is that the F-region is already depleted near the rocket trail proper. As noted, the 6300 Å radiance is proportional to the column rate of recombination of e with OH^+ (and perhaps H_2O^+) to within ~ the 128-sec lifetime of O^1D (this "delay" can be deconvolved out in the final data evaluation).

The southern edge of the glow region becomes steeper than the northern edge, a "hardening" somewhat similar to that observed in barium-ion clouds before they striate. Otherwise the video record, including the segments with 17° x 21° field, shows no obvious radiance irregularities of a spatial scale greater than the camera resolution (about 6 km at the release height with the all-sky lens, 1 km with the longer-focus lens).

The video images are radiometrically calibrated, in that the signal voltage at any picture element can be related to the voltage at the position of the photometer's field of view. Thus the brightness at each point in the scene can be determined from the photometer reading (a correction for vignetting by the lens is required). Frames can be co-added to further improve signal/noise, and Fourier-analyzed
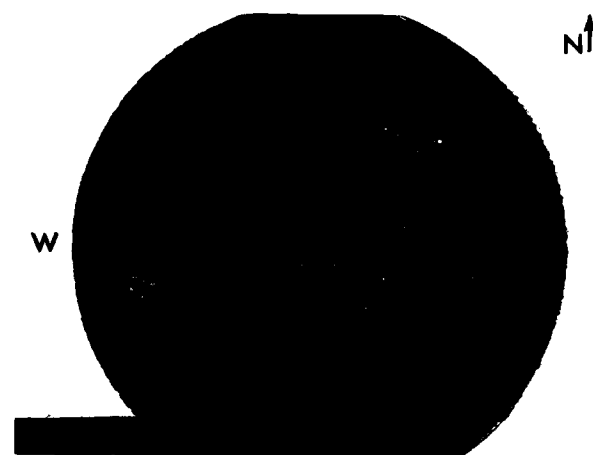
N↑

+ 466 sec
Rocket Altitude
400 km
Zenith 6300 Å
135 R

W
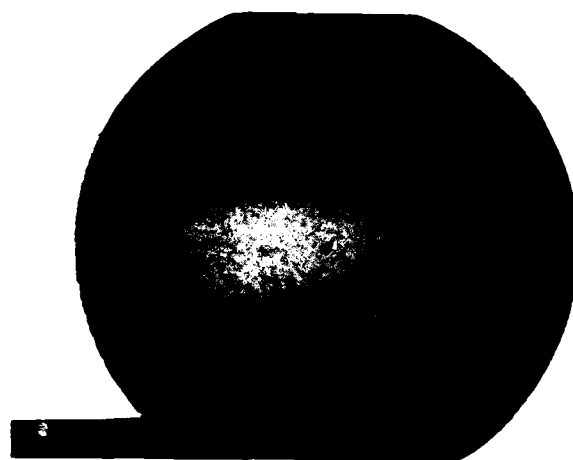
+581 sec
475 km
1400 R
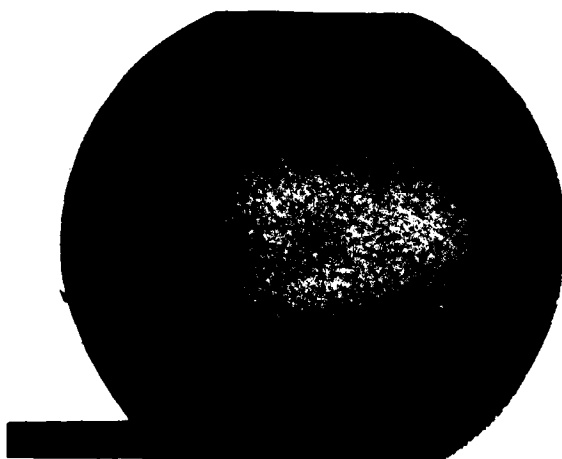
+784 sec
Engine off
4300 R

Figure 36.

All-Sky projections to the aircraft
of the 6300 Å-line glow at three
times after Centaur launch.

to determine the power spectrum of airglow brightness fluctuations; and the dimensions and movement of the afterglow can be unambiguously defined from the "edge" and centroid of the bright area. The original videotape has been copied onto SMPTE Format C tape for digitization and further quantification by AFGL/OPR's image analysis computer.

The <u>zenith photometer</u> was operated partly in 24 sec cycling mode to measure emission at nine wavelengths (two 6300 Å-sensitive channels were provided to double the sampling rate for the OI red line), and partly fixed on 6300 ± 5 Å to measure variations that would result from spatial-temporal structure. Preliminary radiances in the two forbidden oxygen atom lines are plotted in Fig 37. Maximum brightness of the F-region airglow in the moving aircraft's zenith was 8.3 kR 6300 Å, which is substantially higher than predicted. (The total red-doublet column intensity is 11.1 kR, as the photometer is not sensitive to the 1/3 as intense 6364 Å component that terminates on the $^3P_2$ state.) The photometer measurement from Melbourne at $21\frac{1}{2}°$ elevation angle, corrected for its longer slant path length through the depleting ionosphere, is in good agreement with this figure. Peak-to-peak amplitude of the noise on the aircraft photometer chart record appears to be about the same as when the instrument is being calibrated against a standard monochromatic uniform-radiance source. The contribution of optical scintillation to this fluctuation, if any, can be determined from the power spectrum of the recorded signal.

After reaching its peak in ∼ 2 min after onset (Fig 37) the 6300 Å signal decreased with an initial halflife of $2\frac{1}{2}$ min. At 5577 Å the peak is reached in 1 min and the maximum increase was 0.90 kR above the 0.30 kR nightglow (almost all of which comes from neutral chemical reactions in the lower thermosphere). The relative horizontal velocity of the eastward-moving rocket and westward-moving aircraft during this measurement period is 270 km/min; the actual

velocity of the radiation front as a function of exhaust altitude can be determined from the all-sky images.

We made a preliminary attempt to derive from the data in Fig 37 a branching ratio for population of the ^{1}D and ^{1}S states in the dissociative recombination reaction(s) that excite the oxygen atom airglow (purportedly, principally e + OH$^+$). The results are so far inconclusive, most probably because the characteristic time for excitation of O^{1}D atoms is comparable to their 128-sec radiative lifetime, so that the steady-state approximation that we applied is not valid. A more detailed assessment of these photometer data,which may also require taking relative motions into account, is needed.

The signals from six of the filter photometer's other channels over a more limited time period are shown in Fig 38. Their fluctuations before the afterglow reaches the zenith are in large part due to passage of stars through the narrow (2°) field of view. No clear indication of an increase is evident in either the OH (10, 4) monitor signal, or in the Meinel hydroxyl bands to which the longer-wavelength channel is sensitive. The ~1 R or 1 R/$\overset{o}{A}$ increases recorded in the three 10 $\overset{o}{A}$-wide channels sensitive at wavelengths below 6300 $\overset{o}{A}$ have not yet been evaluated. Filter leakage is one possible explanation, as a ~10^4 Rayleigh sky extends well beyond the field of view; this hypothesis can be tested by exposing the photometer to the laboratory calibrator with similar spectral radiance.

Fig's 37 and 38 show only part of the photometer data, sampled to illustrate the gross features of the depletion glow in the aircraft's zenith.

The chart record from the radiometers and 13° forward-pointing photometer near the time the rocket passed the aircraft is reproduced in Fig 39 (received from E.R. Huppi of AFGL/OPR; the stripout for 1.27μm is not yet available). Times during which the aircraft was banking and turning were verified against the
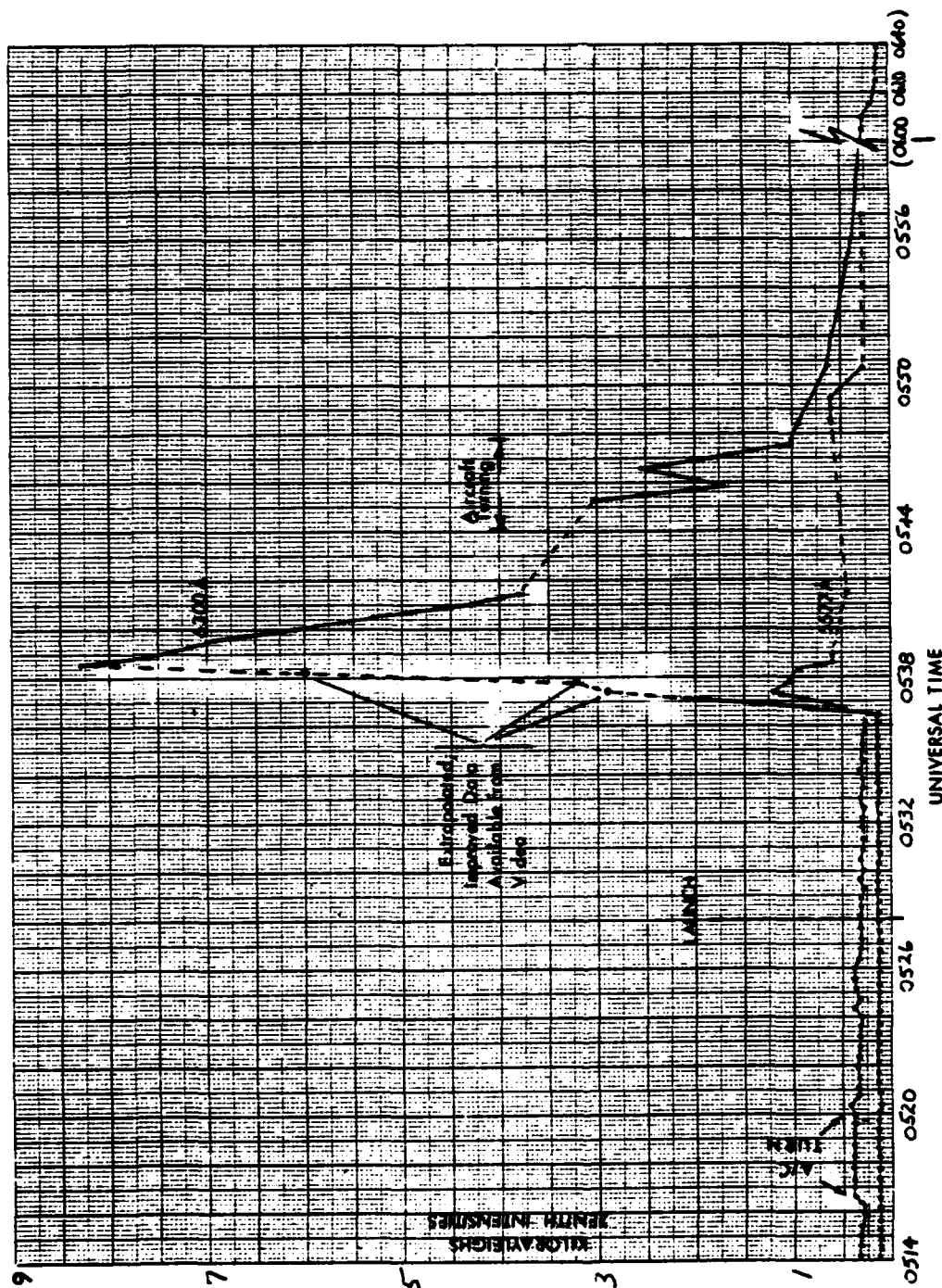
Figure 37. OI 6300 Å and 5577 Å radiance of the nightglow and afterglow of the Centaur release in the aircraft's zenith.

110
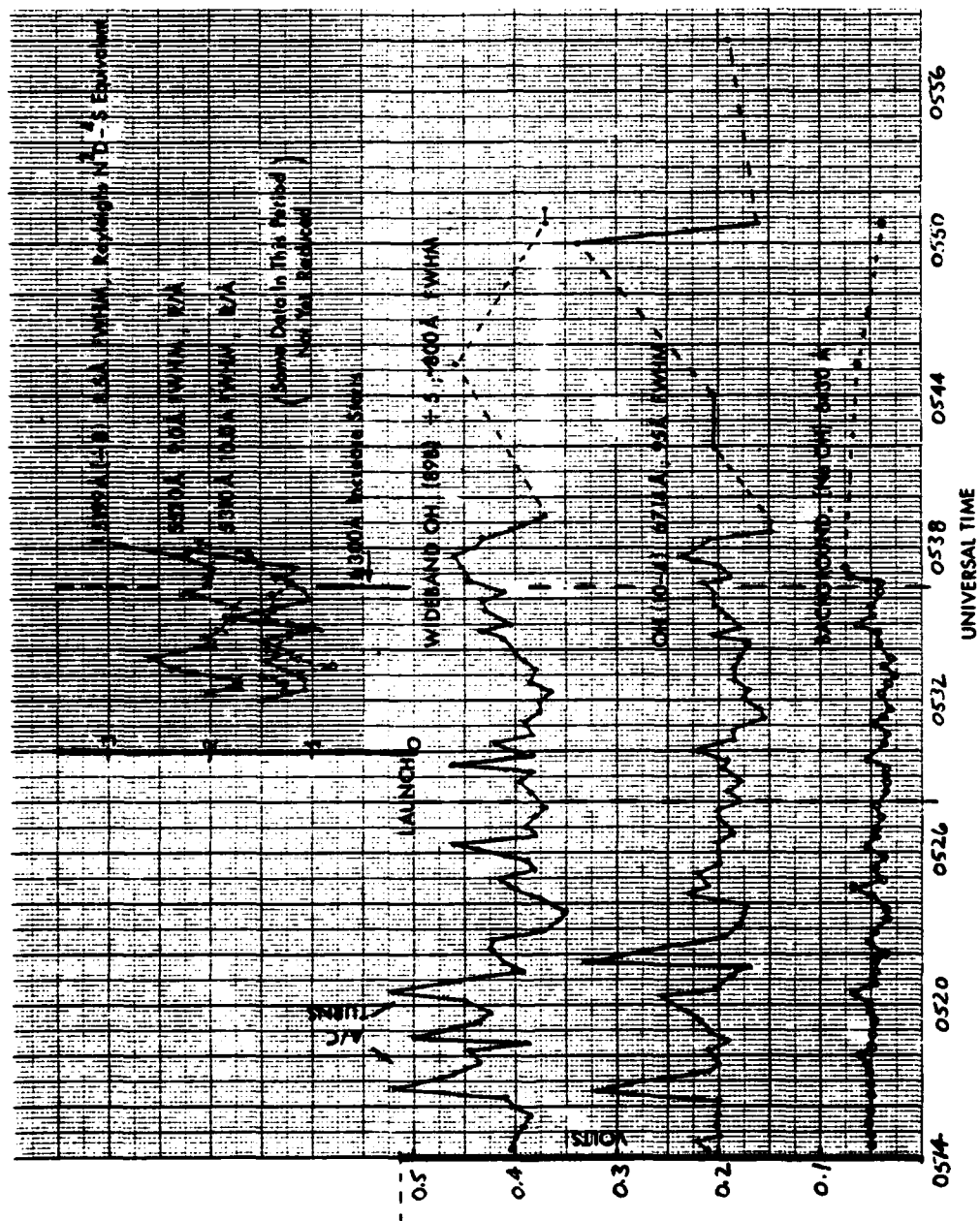
Figure 38. Zenith radiances measured by the aircraft photo-
meter's 5199 Å, 5310 Å, 5520 Å, 6430 Å, 6714 Å
and wideband near-infrared channels.

111
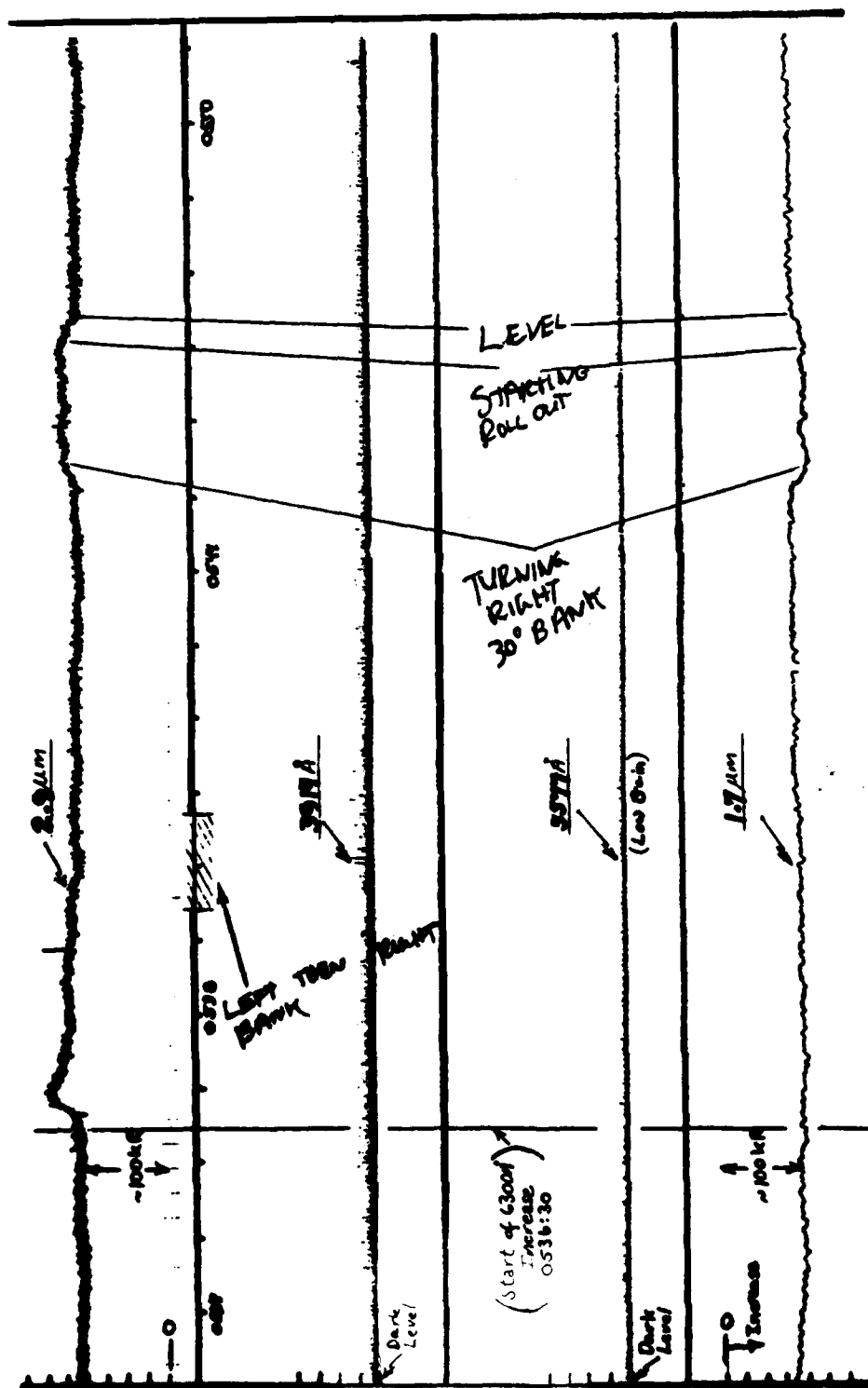
Figure 39. Chart record of the 13° forward-pointing narrow-field instruments and zenith-pointing wide-field OH (1.7μm) radiometer. The aircraft bank is a maximum of 20° near 0540, and 30° where both the 1.7μm and 2.9μm signals are enhanced near 0545.

zenith photometer chart record; roll and azimuth angles can be
determined from the all-sky images, and further information about
the aircraft's orientation is available on the tape of the crewmembers'
voice communications. As the forward-tilted photometers' amplifiers
were set at low gain,no 5577 $\overset{o}{A}$ enhancement is resolvable. The ~30%
increase in the 2.832-3.14µm (FWHM) signal appears to be real,
since when the trace is advanced by the time required for the zenith
photometer's field to reach the radiometer's field it correlates well
with the "prompt" (delayed $\lesssim$ 1 sec by the O^1S state's radiative life-
time) 5577 $\overset{o}{A}$ zenith enhancement (Fig 40). We calculated this time
as

$$\frac{(420 \text{ km rocket trail height}) \times (\tan 13^o)}{(4.5 \text{ km sec}^{-1} \text{ relative velocity})} = 21 \text{ sec.}$$
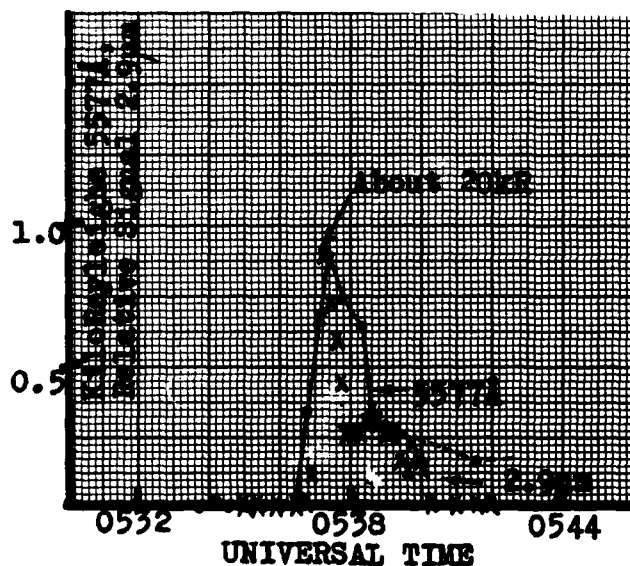
Figure 40.

Comparison of OI 5577 $\overset{o}{A}$ and 2.832-
3.14µm (FWHM) glow enhancements.
The 2.9µm readings have been
delayed by 21 sec to correct for
the offset of the fields of the zenith-
pointing photometer and 13° west-
ward pointing radiometer.

The aircraft banks that start near the end of the enhancement
in the 2.9µm-band signal (at 0539:20, Fig 39) extend to less than 20°,
and produce no discernible change at 1.7µm. In contrast, the bank-
and-turn maneuver starting at 0545, during which the fuselage's roll

113

angle is about 30°, results in 15% (or ~15 kR) increases in the radiances measured by the 1.7μm as well as 2.9μm radiometer. (A final calibration of these two instruments will be available shortly.) This increase is what would be expected from the van Rhijn pathlength gain through the hydroxyl layer, $1/\cos 30^{\circ} = 1.155$; OH airglow (Ref 5) is the source of the sky backgrounds. Similarly a bank to 20° would result in only 6% increases in signal. We conclude that the left-then-right aircraft banks between 0539:20 and 0540:40 — 2-1/3 to 3-2/3 min after the SWIR peak — have only a small effect on the enhancement measured in the 2.9μm band.

The fact that its time dependence follows that of the oxygen green line and its magnitude is about the same as that of the red line suggests that the SWIR increase is also associated with an electron-loss process. One obvious possibility is direct vibrational excitation of OH in dissociative recombination of H_2O^+ ions. The absence (or, perhaps, weakness) of increases in the signals from the other aircraft instruments, which are sensitive to radiation originating from the fifth and higher vibrational levels of $OH(X^2\pi)$ — the radiometer measures in the (1, 0), (2, 1), and (3, 2) Meinel bands —, indicates that most or perhaps all of this original excitation is to low-lying states. (Population of the lower states by the radiative cascade increases the relative intensity of the bands to which the 2.9μm radiometer is sensitive, so that initial excitations to above the fourth vibrational level might be producing OH-band radiation with intensity below the detection thresholds of the other instruments.)

A perhaps even more attractive hypothesis is that the low-lying vibrational states of OH are indirectly populated, following emission of the (A-X) electronic bands. One third of the photons in the spectrums observed under laboratory conditions ("from almost all sources where water vapour is present," Ref 39) are from transitions that terminate in the first and second OH vibrational state, and the remainder in the ground vibrational state. Thus excitation of OH $(A^2\Sigma^+)$ in dissociative recombination of H_2O^+ (and/or, perhaps,

H_3O^+) would provide a selective population mechanism for the (1,0) and (2,1) hydroxyl vibrational bands, which would be measured by the 2.9μm radiometer. This process could have been verified by monitoring the (1,1) and (0,1) electronic bands between ~3200 and 3450 Å.

An afterglow might also result from thermal emission by exhaust H_2O vapor or droplets (or perhaps collisionally-excited OH†). At upper-thermospheric temperatures (≈1500 K) the 2.7μm water molecule band extends to wavelengths within the radiometer's sensitivity range, and liquid water has a strong absorption-emission band centered at 2.99μm. In this regard, calculations (Ref 41) indicate that 1/6 of the H_2O molecules exhausted by the Centaur engine agglomerate into clusters in the nozzle, albeit at temperatures near 200 K where their initial infrared radiation intensity would be low.

DISCUSSION

The mechanisms responsible for the emission in the 2.9μm-band can of course be better identified from a more thorough evaluation of its time dependence, and of the signals from the instruments sensitive to radiation originating from higher vibrational states of OH. The mean zenith radiance within the filter band is 1 watt/sterad per horizontal square kilometer. If the SWIR glow's area is comparable to that of the red glow measured by the video system – as would result from chemiluminescence, and probably also from thermal emission – a background of this order would extend over an area of some $10^4 - 10^5$ km². In a limb view the intensity would be about a factor 3 higher, over an area of ~10^4 km² at F-region heights. It should be noted that although this SWIR background is considerably less intense than that produced by auroral-particle precipitation, it is present over a wide range of higher altitudes.

Excitation of the low-lying metastable states of O proceeds more rapidly than was expected, resulting in higher radiances in the 6300-6364 Å and 5577 Å lines. In contrast the predicted emission

115

in the (10, 4) OH vibrational band is not detectable in the first inspec-
tions of the data trace. Rate coefficients and branching ratios for
initial-state populations, upper limits to sky background enhancements
at other visible infrared wavelengths, and — probably most important —
the growth and transport of the region of ionosphere in which the
plasma deplection is taking place, can be derived from the aircraft
data.

The 136 MHz polarimeters measured polarization changes
of $\sim 4\pi$ during the few min that the depletion grew in, and afterward
detected no abnormal phase or amplitude scintillations in the satellite
transmissions. Some phase fluctuations (possibly due to multi-path
effects) were present, however, in the data from the differential
doppler radar, which has a different set of paths through the depleted
volume. The video images of a "smooth" afterglow appear to verify
the finding of the polarimeter network that no plasma structure of
~ 1 km Fresnel zone dimension developed, and in addition extend this
spatial scale upward to ~ 50 km. (Neither type of sensor would have
resolved F-region irregularities smaller than ~ 1 km, which affect
communication at higher frequencies.) Absence of inhomogeneities —
at least in the nighttime period during which the depletion region was
observable, and at $\gtrsim 1$ km scale size — is thought to be due to the high
dip angle of the geomagnetic field near the release trail (60°, or only
30° from the buoyancy vector).

REFERENCES

1. I. L. Kofsky, D. P. Villanucci, and W. S. Andrus, Assessment of Rocketborne and Airborne Infrared Data, HAES Report No. 79, DNA 4731F (30 Nov 78).

2. R. J. Huppi and J. W. Reed, Aircraft Borne Measurements of Infrared Enhancements During ICECAP 1975 and 1976, HAES Report No. 68, AFGL-TR-77-0232 (28 Sep 77).

3. J. H. Schummers and R. J. Huppi, Interpretation of NO and OH Emission From 1976 Airborne Measurements, HAES Report No. 80, AFGL-TR-79-0027 (1 Jan 79).

4. F. Delgreco and J. Kennealy, private communication (04 Jan 78).

5. I. L. Kofsky, D. P. Villanucci, and R. B. Sluder, Data Reduction and Auroral Characterizations for ICECAP III, HAES Report No. 59, DNA 4220F (31 Jan 77).

6. I. L. Kofsky, D. P. Villanucci, and G. Davidson, Assessment and Evaluation of Simulation Data, HAES Report No. 69, DNA 4303F (15 Nov 77).

7. Photometric and photographic data supplied by the Geophysical Institute at the University of Alaska, College, AK (1977).

8. D. Baker, private communication (1977).

9. A. E. Belon, G. J. Romick, and M. H. Rees, Planet. Space Sci. 14, 597 (1966).

10. A. T. Stair Jr., and J. C. Ulwick (jt. ed.'s), Proceedings of the Second DNA Infrared Data Review Meeting, AFGL-TM-18 (Apr 79).

11. Preliminary Field Report, Nike-Hydac Energy IR807.57-1 Flight Results, SDC TM-1540, Space Data Corporation (27 Nov 78).

12. D. Baker, private communication (1978).

13. M. A. McCready and J. D. Kelly, Chatanika Radar Operations During Flights of DNA Rockets SWIR (IC807.15-1), TMA (IC 806.35-1), and IR (IR807.57-1) on 26 October 1978, SRI Data Report on Project 5915 (Apr 79).

REFERENCES (continued)

14. Preliminary Field Report, Nike Hydac IC807.15-1, Nike Hydac
    IC807.15-2, Nike Javelin IC806.35-1, Nike Hydac IR807.57-1,
    Utah State University and Air Force Geophysics Laboratory
    (Oct 78).

15. W,F. Grieder and L.A. Whelan, Geometric Aspects of Rocket
    Photometry, HAES Report No. 41, AFGL-TR-76-0046 (Feb 76).

16. D.H. Archer, Requirements for Improved Infrared Prediction
    Capability, HAES Report No. 78, DNA 4585F (30 Apr 78).

17. M.J. Baron, private communication, July 1978.

18. R. Vondrak et al., Simultaneous AE-C and Chatanika Radar
    Measurements of Auroral Particle Fluxes and Ionospheric
    Electron Density Profiles, paper presented at Atmospheric
    Explorer Symposium, Bayse, VA, 1978.

19. R. Vondrak and R. Sears, J. Geophys. Res. 83, 1655 (1978).

20. E.R. Huppi, private communication (1978).

21. B.P. Sandford and L.R. Doan, Graphs of the Solar Depression
    Angle from 0° to 32° vs Local Hour Angle for Latitudes 0° to
    90°, AFCRL-69-0543 (Dec 69).

22. G.T. Best and N.W.Rosenberg, Spectroscopic Studies of Barium
    Releases, AFCRL-70-0724 (12 Nov 70).

23. W.G. Blattner et al., Applied Optics 13, 534 (1974).

24. Handbook of Geophysics and Space Environments, ed. S.L.
    Valley, McMillan, NY, 1965.

25. R. Nadile et al., Ref 10, pp 200 ff.

26. H.S. Mitchell, Ref 10, p 267 ff.

27. P.M. Banks and G. Kockarts, Aeronomy, Part A, Academic
    Press, NY 1973, p 57 ff.

28. M. Mendillo, G.S. Hawkins, and J.A. Klobuchar, Science 187,
    343 (1975); J. Geophys. Res. 80, 2217 (1975).

REFERENCES (continued)

29. AGU Meeting, April 1978, Session SPR on Active Ionosphere Modification; EOS Trans. AGU 59, 334-5 (1978).

30. P.A. Bernhardt, The Response of the Ionosphere to the Injection of Chemically Reactive Vapors, Stanford Electronics Laboratories Report SEL-76-009 (May 76).

31. D.N. Anderson and P.A. Bernhardt, J. Geophys. Res. 83, 4777 (1978).

32. J. Zinn and C.D. Sutherland, (LASL/J-10) Memorandum: Atlas-Centaur/HEAO-C Launch-Ionospheric Effects — Computer Model Predictions (21 Apr 79).

33. M. Mendillo and J.M. Forbes, J. Geophys. Res. 83, 151 (1978).

34. M. Mendillo, J. Baumgardner, and J.A. Klobuchar, EOS Trans. AGU 60 (#27) (3 July 1979).

35. P.A. Bernhardt, A.V. DaRosa, and M. Mendillo, EOS Trans. AGU 59, 1162 (1978).

36. I.L. Kofsky, Bimonthly Reports 1 and 2 on Contract DNA001-C-0162, 15 Mar and 15 May 1976; DNA 4439F-1 (HAES Report No. 72-1), 01 Feb 78.

37. S.L. Ossakow et al., NRL Memorandum Report 3769 (May 1978).

38. G.W. Sjolander and E.P. Szuszczewicz, J. Geophys. Res. 84, 4393 (1979).

39. R.W.B. Pease and A.G. Gaydon, The Identification of Molecular Spectra, Chapman and Hall, London, 1965.

40. A.L. Broadfoot and K.R. Kendall, J. Geophys. Res. 73, 426 (1968).

41. P.A. Bernhardt et al., Notes for HEAO-C/SPS Workshop, unnumbered.

Blank

APPENDIX I

MEMORANDUM

DATE: 18 April 1979

TO: Memo for Record –   To   Mayo, Stair, O'Neil
                                        (Davidson, Villanucci)

FROM: I. L. Kofsky

SUBJECT: Major Findings/Issues at DNA Infrared Data Review
            Meeting, 10-12 April 1979 -- <u>First Look</u>

The principal purpose of this preliminary summary of the second
Data Review is to identify priorities for future work on infrared sky
backgrounds. Mention is made, where appropriate, of progress since
the 1977 HAES IR Data Meeting in Falmouth, MA.

After a brief comment on the impetus provided by future surveillance
systems, the material in this (unclassified) note is broken out along the
lines of the meeting itself: SWIR, MWIR, LWIR, and Related Investiga-
tions and Applications.

Systems Overview

The fact that there are now under consideration several IR sur-
veillance systems, which would operate at a series of wavelengths and
viewing-geometries-against-the-atmosphere, is giving increased scope
to investigations of nuclear explosion-excited sky backgrounds. The
climate for taking these backgrounds into account in early stages of
sensor design is improving, in part due to the efforts of R&D Associates,
who have issued a handbook for use by SAMSO and their contractors.
(That is to say, information provided by DNA is used to help make new
systems effective, rather than assess existing ones.) Design and post
hoc performance evaluation are being facilitated by computer simu-
lations of the impact of spatially- and temporally-structured increases
in background radiance.

SWIR – 2.7μm Band

There was general agreement that more nitric oxide molecules are
produced by charged particle bombardment of air above 100 km than is
currently predicted by DoD or other aerochemical models, by a factor
2-10. No new hypothesis explaining this anomaly was advanced.

On the other hand, there remains substantial controversy on the
population of NO^+ and other potential radiators in the 2.7μm band
despite COCHISE's clarification of the partial rate coefficients in

$N^2D + O_2$ reactors and the essential validation of Billingsley's calculated NO^+ Einstein coefficients by COCHISE and LABCEDE. Here is a partial list of field simulation results that cannot be considered satis-factorily explained.

1. The near-zenith intensity at wavelengths between 2.63 and 2.859μm (FWHM) measured by the radiometer on IC807.15-1 (26 Oct 78) is about 50% higher than predicted by Ed Lee's "NO" model, which includes the aforementioned AFGL laboratory data as critical point.

2. The particle bombardment-associated zenith intensities near 2.8μm measured in the series of aircraft flights, after careful and systematic evaluation, contain almost factor-two variations at the 90% confidence level (PhotoMetrics presentation). The aircraft data have succeeded in showing that within the ~ 3/4 min, ~20 km resolution of the instrument system the SWIR output from air above ~100 km altitude follows the particle energy-deposition input, with linearity up to inputs equivalent to at least 60 kR N_2^+ 3914 Å-band column intensity.

It was suggested (by Dr. Stair) that variability of quenching by O atoms is the source of this variation in chemiluminous yields. We intend to check on this idea, using the [O] profiles tabulated by Hegblom and the quenching cross-sections codified by Kennealy. Other sugges-tions made by the participants – try throwing out the high data points, put the data in order of time, add a fixed background to some of the readings – appear less useful, but we'll nevertheless attmpt to consider them.

3. The 2.7μm signals measured up to ~10 msec after energy deposition in EXCEDE SWIR and EXCEDE II Test have the wrong intensities and altitude dependences. Attempts were made to explain these measurements by invoking water vapor from the rocket (and thus hydroxyl radicals), a beam-plasma discharge (in EXCEDE II Test), and unidentified near-prompt radiators. The 5.3μm signals from EXCEDE SWIR do appear to fit a $N^2D + O_2$ model (O'Neil presentation).

4. The vibrational spectrum at wavelengths above 5.2μm taken by HIRIS II's interferometer is not what would be expected from AFGL laboratory results. That the emission is indeed from NO is shown by the good spectral fit of rotational lines. A selective deactivation of the NO v = 2 state could bring the vibrational distributions into agree-ment. Also, HIRIS doesn't find the high 1,0 intensity from the NO + O interchange reaction that would be expected from other HAES rocket measurements; and the inferred rotational temperature 500 (+ 70, -60)K is perhaps a bit high, but not implausible.

The point was made (by Dr. Stair and others) that these unexplained simulations results may result from mechanisms that DoD modelers are not taking into account in their predictions of the intensity and structure of nuclear-induced IR emissions. Therefore, at the energy deposition altitudes and dose levels of actual interchange, the relative error in background that designers of survivable systems have planned for could be substantially greater than the relative departure of the field data from predictions of current codes.

The technical status of precursor and directly $NO^{\ddagger}$-producing and -quenching reactions is as follows. Population by N_2 (A) is not understood, with no discernible progress since 1977. Direct production of N^2D atoms is 0.9 per ion pair, according to Gilmore, to which the contribution from $e + NO^+$ and $e + N_2^+$ recombination reactions should be added. Stephens stated in his presentation that ROSCOE results could be very sensitive to these N^2D numbers and to the N^2P excitation yields. There remains a factor-of-three variation in estimates of the rate coefficient for quenching of N^2D by O, which competes with excitation of $NO^{\ddagger}$ at altitudes where debris energy is deposited. Rate coefficients for depopulation of $NO^{\ddagger}$ by O are in poor-to-fair shape.

The 2.7µm data from the coning 26 Oct 78 rocket have not been sufficiently well reduced, in my judgment, to merit the level of analysis given them for presentation at the meeting. Our own preliminary reduction showed a minimum in the chemiluminous SWIR yield near 105 km, which I would consider more important than this one more measurement of a "mean" photon ratio. This minimum was also measured by the sidelooking radiometer of A18.219-1 (HAES 59), and figures in Archer's calculations of quenching by $NO^{\ddagger}$ by O atoms (in HAES 78).

(Some further SWIR observations, and a comment on NO γ-band emission in aurora-excited air, are discussed in the final section on Related Investigations.)

MWIR – 4.3µm to ~6µm

Excess near-prompt radiation – above the predictions of the CO_2 pumping model – keeps appearing. Kumer interprets the 26 Oct 78 rocket data taken above 100 km as "suggesting a second auroral mechanism that is related to the instantaneous energy deposition ...," with in-band intensity 15 photons per N_2^+ 3914 Å photon. This would be a luminous energy yield of 3/4%. Mitchell pointed out that this interpretation would require the radiation to be measured also at lower altitudes, unless it were CO_2 direct fluorescence terminating in the ground state, since its spectrum would be unlikely to line up with the lower-altitude CO_2's rotational line absorption. EXCEDE SWIR (4.2-4.4µm sensitivity) measures 0.2 - 0.33 4.3µm photons per 3914 Å photon emitted within ~30 millisec of energy deposition at 98 km.

EXCEDE II Test (4.21 - 4.29μm sensitivity), with a much shorter effective viewing time because of the rocket's greater horizontal velocity, measures an increase from 0.1 to 0.74μm photons per 3914 Å photon between the higher altitudes 110 and 135 km. Various ideas on this near-prompt radiation and its altitude profile were presented, among them the quenching of $NO^{+\ddagger}$ by dissociative recombination in the dense free electron cloud produced by EXCEDE's accelerator.

The data presented by PhotoMetrics on the several "near-prompt" 4.3μm emissions measured by the az- and el-scanning radiometer of A18.219-1 lend themselves to interpretation in terms of $N_2^{\ddagger}$ -related predosing and/or CO_2 fluorescence or NO^+ emissions. Kofsky and Kumer stressed the value of multiple-field rocket radiometry of the emission, backed up of course by measurements of predosing and winds-transport.

While much has been learned in the last two years about collisional quenching of vibrationally-excited NO^+, nothing has been turned up on excitation distributions from the three or four exothermic reactions known to produce NO^+ ions. On the other hand the possibility of a contribution to 4.3μm-band radiation from $^{15}N^{14}N^{\ddagger}$ has been largely discounted, on the grounds that the molecule's band strength is orders of magnitude lower than estimated by the Russian promulgators (Markov & collaborators) of emission by $^{15}N^{14}N$. The DNA analysts now believe that Markov's people misinterpreted an early paper by the theoretician D. R. Bates, which ascribed the previously-used higher figure to $^{15}N^{14}N^+$. Additionally, the $^2D^1H$ molecule, which would be expected to have a much greater electric dipole moment than $^{15}N^{14}N$, has a lifetime against vibrational radiation 100x longer than the Russians' 50-sec estimate for $^{15}N^{14}N$. AFGL (Cochise) has procured from England a liter STP of pure $^{15}N^{14}N$, with which they will attempt to get an upper limit to the integrated band strength in an absorption cell. It should be pointed out that in 1977 $^{15}N^{14}N$ was still considered to be a major potential 4.3μm radiator.

Other developments are that the (H + O_3 ? →) $OH^{\ddagger}$ → $N_2^{\ddagger}$ → $CO_2^{\ddagger}$ mechanism for exciting CO_2 ν_3 radiation is now generally accepted; and the ~20x greater probability of CO_2 radiating at 4.3μm than resonant scattering after absorbing 2.7μm (solar and other) photons, has been confirmed.

Backgrounds from N_2O molecules near 4.8μm (and at other wavelengths) have so far not been observed in the natural atmosphere. A possible exception is the 4.6μm data of 12 Mar 75 (Multi IC519.07.1B), which is perhaps better interpreted as CO (Kumer).

LWIR

The hot (ν_3) bands of O_3 between 9.64μm and ~11μm have now been seen both in the atmosphere (by SPIRE) and laboratory (COCHISE), in effect verifying Gilmore's prediction of some years ago. This new information has had important impact on the earth limb models used by DoD planners.

The Murcray phenomenon was laid to rest as a natural or nuclear-induced background. Nonetheless its interpretation requires considerably more water in the high-altitude stratosphere, in droplet and vapor form, that was previously thought to be present.

Considering the important future role of LWIR, as illustrated by Stair's review, only a small amount of new information was presented on LWIR backgrounds excited by nuclear explosions.

Related Investigations, Applications

1. Stair presentation: – as noted, the increased application of IR should increase the demand for information on post-attack performance.

2. Gilmore reaction-rates assessment: – of about 33 entries, at least 25 rated a Yes for additional work, and some others a No(?).

Gilmore stressed the potential importance of UO^+ and $A\ell O$, which, although present in concentrations ~10 those of "airlike" IR molecular radiators, may have comparably higher earthshine and sunlight scattering cross-sections. Little discussion developed on assigning priority to the experimental and theoretical investigations needed to generate reaction rate data. This must be at least in part a result of the focusing of DNA's Reaction Rate (nee Chemistry) program on directly user- and systems-oriented issues.

3. The issue of OH $\Delta v = 1$ intensity and structure was touched on; by Sears who can measure near 8000 Å when aurora is < IBC $\frac{1}{2}$, by Nadile who reports a double layer measured from limb-viewing SPIRE, and by Mitchell in his material on gravity waves. It is worth noting that the double layer has not been authoritatively reported before (although it was suggested by some zenith-viewing rocket profiles), and that fitting the new profile should provide a challenge for the aeronomy modelers. (Someone mentioned that the minimum could be "a temperature effect;" someone else talked about hydration of O_3 (which otherwise participates in the H + O_3 excitation reaction); and of course there is always the HO_2 + O mechanism.) SPIRE also provided what looks to be important information on the near-infrared scattering by aerosols in the stratosphere.

4. On the matter of γ-band emission from NO: – this is a topic that I had reviewed at earlier meetings, as the A-X transition (presumably excited by collisions of ambient NO with $N_2(A)$) leaves the NO molecule in a vibrationally excited state. Huffman brought out that the purported 1,0 band at 2150 Å, which has been the subject of study and even controversy over the past ten years because of its anomalously high intensity, is overlaid in aurora by a N^+ doublet with 4 Å separation. His CRL-246 spectrometer measurements (1 Å best resolution) should be able to resolve this issue. The point of this for the DNA community is, that past inferrals of high [NO] in energetic particle-excited air from the high signals near 2150 Å seen by lower-resolution instruments on sounding rockets and polar-orbiting satellites, are most probably incorrect.

5. On EXCEDE: – the standard of interpretation of the infrared radiances measurable in the short (millisecs) periods in which the onboard spectroradiometers maintain the electron-irradiated volume in their fields, has been sharply upgraded since the previous HAES data meeting. The models of grow-in of excitation developed by AFGL use as checkpoints the OI 5577 Å -line intensities measured from ground and rocket, and (particularly) the in situ measurements of electron and species concentrations by Narcisi's mass spectrometers.

6. AℓO radiation from PRECEDE's trail: – the results are certainly interesting, but taken out of the context of the many tri-methyl aluminum and aluminized grenade releases of the last twenty years they are not fully convincing. Specifically, while it is well known that the continuum emission requires the presence of O atoms, it is equally well established that the intensity doesn't directly follow [O] – that is, the process is kinetically complex. The rate coefficient figure presented in the abstract refers to disappearance of Aℓ – it is merely a hypothesis that it could be the rate for chemiluminous two-body reaction with O atoms. The potentially important point of the fortuitous trail release is its unexpected brightening in the regions irradiated by PRECEDE's electron beam.

- - - - - - - - - - - - - - - - - - - -

Suggestions for improving AFGL's first draft of the Proceedings of the meeting, in particular the direct quotes from the discussions of the presentations, were incorporated in the final edition, the page of comments in the original memorandum is therefore not reproduced here.)

In addition there were active, fast-moving discussions of several other issues. The value of including in systems codes natural atmospheric turbulence and winds which displace clutter areas and otherwise change the radiance structure, was debated by Ise and Zimmerman. The fact that atmospheric heave impacts chemistry, in ways not readily handled by systems codes, was brought out. Inability of systems codes to predict accurately the return to ambient and their inadequacy as

vehicles for assessing sensitivity to accuracy of rate coefficient information - both effects are due to the simplifications needed to reduce running time to manageable levels - was mentioned ("ROSCOE isn't designed to predict natural phenomena").

I would have liked to have heard more discussion on the minor topic of incoherent-scatter radar support of IR backgrounds investigations and the major question What further field simulation and laboratory data do we need, and what's the most effective way to get it?   While use of the perhaps - soon-to-depart Chatanika radar did receive mention, the radar's contribution was not clearly brought out. In practice the accurate energy deposition altitude profiles and E-region winds that it measures (it does a reasonable job on neutral winds, important in 4.3µm investigations) are useful in determining predosing and could be of some help in the aircraft program.   By providing a range-resolved probe of the auroral ionosphere, the radar gives added credibility to the IR-optical measurements -- all of this, of course, at the great cost of operating the facility. The review of past data, at its present stage of evaluation, should serve to get people thinking about what further investigations are needed to allow DNA to provide IR systems planners with reliable backgrounds predictions.

Blank

DISTRIBUTION LIST

DEPARTMENT OF DEFENSE

Assistant to the Secretary of Defense
Atomic Energy
    ATTN: Executive Assistant

Defense Advanced Rsch. Proj. Agency
    ATTN: TIO

Defense Nuclear Agency
2 cy ATTN: RAAE
4 cy ATTN: TITL

Defense Technical Information Center
12 cy ATTN: DD

Field Command
Defense Nuclear Agency
    ATTN: FCPR

Field Command
Defense Nuclear Agency
Livermore Division
    ATTN: FCPRL

Undersecretary of Defense for Rsch. & Engrg.
    ATTN: Strategic & Space Systems (OS)

DEPARTMENT OF THE ARMY

Atmospheric Sciences Laboratory
U.S. Army Electronics R&D Command
    ATTN: DELAS-EO-MO, M. Heaps
    ATTN: DELAS-EO-ME, K. Ballard
    ATTN: DELAS-EO, F. Niles

BMD Advanced Technology Center
Department of the Army
    ATTN: ATC-O, W. Davies
    ATTN: ATC-T, M. Capps

Harry Daimond Laboratories
Department of the Army
    ATTN: DELHD-I-TL, M. Weiner
    ATTN: DELHD-I-TL
    ATTN: DELHD-N-P

U.S. Army Ballistic Research Labs.
    ATTN: DRDAR-BLP, J. Heimerl
    ATTN: DRDAR-BLB, M. Kregel
    ATTN: DRDAR-BLT, J. Vanderhoff
    ATTN: DRDAR-TSB-S

U.S. Army Foreign Science & Tech. Center
    ATTN: DRXST-SD-3

U.S. Army Missile Command
    ATTN: Redstone Scientific Info. Ctr.

U.S. Army Nuclear & Chemical Agency
    ATTN: Library

U.S. Army Research Office
    ATTN: R. Mace

U.S. Army TRADOC Systems Analysis Activity
    ATTN: ATAA-PL

DEPARTMENT OF THE ARMY (Continued)

White Sands Missile Range
Department of the Army
    ATTN: STEWS-TE-AN, M. Squires

DEPARTMENT OF THE NAVY

Naval Electronic Systems Command
    ATTN: PME 117-20
    ATTN: ELEX 03
    ATTN: Code 501A

Naval Intelligence Support Ctr.
    ATTN: Document Control

Naval Ocean Systems Center
    ATTN: Code 532, R. Pappert
    ATTN: Code 4471
    ATTN: Code 5322, H. Hughes
    ATTN: Code 5321, I. Rothmuller
    ATTN: Code 532, J. Richter
    ATTN: Code 5324, W. Moler

Naval Postgraduate School
    ATTN: Code 0142, Library

Naval Research Laboratory
    ATTN: Code 7175, J. Johnson
    ATTN: Code 6780, J. Fedder
    ATTN: Code 7550, J. Davis
    ATTN: Code 7101, P. Mange
    ATTN: Code 4701, J. Brown
    ATTN: Code 1434, E. Brancato
    ATTN: Code 2627
    ATTN: Code 7120, R. Kinzer
    ATTN: Code 7122, D. McNutt
    ATTN: Code 4700, T. Coffey
    ATTN: Code 7175H, D. Horan
    ATTN: Code 4780, S. Ossakow
    ATTN: Code 6750, D. Strobel
    ATTN: Code 4709, W. Ali
    ATTN: Code 6750, K. Hain

Naval Surface Weapons Center
    ATTN: Code R41, D. Land
    ATTN: Code F31
    ATTN: L. Rudlin
    ATTN: Code F46, D. Hudson

Nuclear Weapons Tng. Group, Pacific
Department of the Navy
    ATTN: Nuclear Warfare Department

Office of Naval Research
    ATTN: Code 421, B. Junker
    ATTN: Code 465, G. Joiner

DEPARTMENT OF THE AIR FORCE

Air Force Technical Applications Center
    ATTN: TF, L. Seiler
    ATTN: TD
    ATTN: STINFO Office/TF

DEPARTMENT OF THE AIR FORCE (Continued)

Air Force Geophysics Laboratory
    ATTN: LKB, W. Swider, Jr.
    ATTN: OPR-1, J. Ulwick
    ATTN: SULL
    ATTN: LKB, T. Keneshea
    ATTN: LKB, E. Murad
    ATTN: LKB, J. Paulson
    ATTN: LKB, K. Champion
    ATTN: LKO, R. Van Tassel
    ATTN: LKD, C. Philbrick
    ATTN: LKD, R. Narcisi
    ATTN: PHG, F. Innes
    ATTN: OPR, T. Connolly
    ATTN: LKO, R. Huffman
    ATTN: OPR, A. Stair
    ATTN: OP, J. Garing
    ATTN: OPR, R. O'Neill
    ATTN: OPR, F. DelGreco
    ATTN: OPR, H. Gardiner
    ATTN: OPR, J. Kennealy

Air Force Weapons Laboratory
Air Force Systems Command
    ATTN: DYV, E. Copus
    ATTN: SUL

Foreign Technology Division
Air Force Systems Command
    ATTN: NIIS, Library
    ATTN: WE

Rome Air Development Center
Air Force Systems Command
    ATTN: OCS, V. Coyne
    ATTN: OCSA, J. Simons

USAFETAC/CB
    ATTN: CBTL, STOP 825

DEPARTMENT OF ENERGY CONTRACTORS

EG&G, Inc.
Los Alamos Division
    ATTN: P. Lucero
    ATTN: J. Colvin
    ATTN: D. Wright

Lawrence Livermore National Laboratory
    ATTN: L-71, J. Chang

Los Alamos National Scientific Laboratory
    ATTN: MS 664, J. Zinn
    ATTN: MS 668, H. Hoerlin
    ATTN: MS 560, W. Hughes
    ATTN: MS 668, J. Malik
    ATTN: MS 212, W. Barfield

Sandia National Laboratories
    ATTN: Org. 4241, T. Wright
    ATTN: Org. 1250, W. Brown

OTHER GOVERNMENT AGENCIES

Bureau of Mines
Pittsburgh Mining & Safety Rsch. Ctr.
    ATTN: J. Murphy

OTHER GOVERNMENT AGENCIES (Continued)

Department of Commerce
National Bureau of Standards
    ATTN: W. Lineberger
    ATTN: S. Leone
    ATTN: A. Phelps

Department of Commerce
National Bureau of Standards
    ATTN: M. Scheer
    ATTN: S. Abramowitz
    ATTN: R. Hampson, Jr.
    ATTN: J. Devoe
    ATTN: D. Lide
    ATTN: D. Garvin
    ATTN: M. Krauss
    ATTN: L. Gevantman
    ATTN: J. Cooper

Department of Commerce
National Oceanic & Atmospheric Admin.
    ATTN: J. Angell
    ATTN: L. Machta

Department of Commerce
National Oceanic & Atmospheric Admin.
    ATTN: Assistant Administrator, RD

Department of Commerce
National Oceanic & Atmospheric Admin.
    ATTN: E. Ferguson
    ATTN: D. Albritton
    ATTN: F. Fehsenfeld
    ATTN: W. Spjeldvik

Department of Transportation
Transportation Rsch. System Center
    ATTN: F. Marmo

NASA
Goddard Space Flight Center
    ATTN: Code 625, M. Sugiura
    ATTN: Code 625, J. Heppner
    ATTN: A. Aikin
    ATTN: S. Bauer
    ATTN: J. Vette
    ATTN: Technical Library

NASA
George C. Marshall Space Flight Center
    ATTN: W. Roberts

NASA
    ATTN: D. Dement
    ATTN: E. Schmerling
    ATTN: N. Roman
    ATTN: R. Schiffer

NASA
Johnson Space Center
    ATTN: Code JM6, Technical Library

NASA
Ames Research Center
    ATTN: N-245-3, R. Whitten
    ATTN: W. Starr
    ATTN: G. Poppoff

OTHER GOVERNMENT AGENCIES (Continued)

National Science Foundation
ATTN: R. Sinclair
ATTN: Div. of Atmos. Sci., R. McNeal

DEPARTMENT OF DEFENSE CONTRACTORS

Aero-Chem Research Labs., Inc.
ATTN: A. Fontijn

Aerodyne Research, Inc.
ATTN: F. Bien
ATTN: M. Camac
ATTN: Librarian, B. Duston
ATTN: M. Faist

Aeronautical Rsch. Assoc. of Princeton, Inc.
ATTN: H. Pergament

Aerospace Corp.
ATTN: H. Mayer
ATTN: M. Whitson
ATTN: R. Cohen
ATTN: Library
ATTN: T. Taylor

University of Alaska
ATTN: Technical Library
ATTN: N. Brown
ATTN: R. Parthasarathy

AVCO Everett Research Lab., Inc.
ATTN: C. Von Rosenberg, Jr.

Berkeley Research Associates, Inc.
ATTN: J. Workman

Boston College
ATTN: Dept. of Chemistry, D. McFadden
ATTN: Science Library, F. McElroy
ATTN: Chairman, Dept. of Physics

University of California at San Diego
ATTN: D. Miller

University of California at Santa Barbara
ATTN: M. Steinberg

California Institute of Technology
ATTN: S. Trajmar
ATTN: V. Anicich

University of California
ATTN: H. Johnston

Calspan Corp.
ATTN: Library
ATTN: W. Wurster
ATTN: C. Treanor

Chem Data Research
ATTN: K. Schofield

University of Colorado
ATTN: Dept. of Chemistry, V. Bierbaum

Columbia University
ATTN: H. Foley

DEPARTMENT OF DEFENSE CONTRACTORS (Continued)

University of Denver
ATTN: D. Murcray
ATTN: B. Van Zyl

Epsilon Labs., Inc.
ATTN: C. Accardo

ESL, Inc.
ATTN: W. Bell

General Electric Co.
ATTN: Technical Information Center
ATTN: J. Burns
ATTN: P. Zavitsanos
ATTN: J. Peden
ATTN: M. Linevsky
ATTN: R. Edsall
5 cy ATTN: T. Baurer
6 cy ATTN: M. Bortner

General Electric Co.
ATTN: J. Schroeder

General Electric Company-TEMPO
ATTN: D. Reitz
ATTN: B. Gambill
ATTN: M. Dudash
ATTN: DASIAC
ATTN: J. Thompson
ATTN: D. Chandler
ATTN: M. Stanton
ATTN: T. Stevens
ATTN: W. Knapp

General Research Corp.
ATTN: J. Ise, Jr.

General Research Corp.
ATTN: T. Zakrzewski

Howard University
ATTN: W. Jackson

HSS, Inc.
ATTN: D. Hansen
ATTN: M. Shuler

Information Science, Inc.
ATTN: W. Dueziak

Institute for Defense Analyses
ATTN: E. Bauer
ATTN: H. Wolfhard

Ion Physics Corp.
ATTN: C. Hauer

IRT Corp.
ATTN: D. Vroom
ATTN: J. Rutherford
ATTN: R. Neynaber
ATTN: R. Overmyer

Johns Hopkins University
ATTN: Document Librarian

Johns Hopkins University
ATTN: J. Kaufman

DEPARTMENT OF DEFENSE CONTRACTORS (Continued)

Kaman Sciences Corp.
    ATTN: W. Rich
    ATTN: D. Foxwell

KMS Fusion, Inc.
    ATTN: Library

Lockheed Missiles & Space Co., Inc.
    ATTN: D. Divis

Lockheed Missiles & Space Co., Inc.
    ATTN: J. Reagan
    ATTN: J. Evans
    ATTN: M. Walt
    ATTN: T. James
    ATTN: R. Sears
    ATTN: B. McCormac
    ATTN: R. Gunton
    ATTN: J. Kumer

University of Lowell
    ATTN: G. Best

M.I.T. Lincoln Lab.
    ATTN: B. Watkins

University of Maryland
    ATTN: Chemistry Dept., J. Vanderslice

University of Massachusetts
    ATTN: H. Sakai

University of Minnesota
    ATTN: J. Winkler

University of Minnesota
    ATTN: M. Hirsch

Mission Research Corp.
    ATTN: W. White
    ATTN: D. Sappenfield
    ATTN: M. Messier
    ATTN: M. Scheibe
    ATTN: V. Van Lint
    ATTN: R. Hendrick
    ATTN: D. Archer
    ATTN: R. Kilb

National Academy of Sciences
    ATTN: J. Sievers

State University of New York at Buffalo
    ATTN: G. Brink

Nichols Research Corp., Inc.
    ATTN: N. Byrn

Pacific-Sierra Research Corp.
    ATTN: E. Field, Jr.

Panametrics, Inc.
    ATTN: B. Sellers

Pennsylvania State University
    ATTN: J. Nisbet
    ATTN: L. Hale

DEPARTMENT OF DEFENSE CONTRACTORS (Continued)

PhotoMetrics, Inc.
    ATTN: I. Kofsky

Physical Science Lab.
    ATTN: W. Berning

Physical Sciences, Inc.
    ATTN: G. Caledonia
    ATTN: R. Taylor
    ATTN: K. Wray

University of Pittsburgh
    ATTN: F. Kaufman
    ATTN: W. Fite
    ATTN: M. Biondi

Quantum Systems, Inc.
    ATTN: S. Ormonde

R & D Associates
    ATTN: F. Gilmore
    ATTN: B. Gabbard
    ATTN: H. Ory
    ATTN: R. Turco
    ATTN: R. Lelevier
    ATTN: C. MacDonald

R & D Associates
    ATTN: B. Yoon
    ATTN: J. Rosengren
    ATTN: H. Mitchell

Radiation Research Associates, Inc.
    ATTN: N. Schaeffer

Rand Corp.
    ATTN: C. Crain

Science Applications, Inc.
    ATTN: D. Hamlin

Science Applications, Inc.
    ATTN: N. Byrn

Science Applications, Inc.
    ATTN: R. Johnston

Professor Chalmers F. Sechrist
    ATTN: S. Bowhill
    ATTN: C. Sechrist

SRI International
    ATTN: T. Slanger
    ATTN: A. Whitson
    ATTN: M. Baron
    ATTN: J. Peterson
    ATTN: A. Peterson
    ATTN: J. Moseley
    ATTN: E. Kindermann
    ATTN: D. Hildenbrand
    ATTN: R. Leadabrand
    ATTN: R. Hake, Jr.
    ATTN: G. Black
    ATTN: V. Wickwar

SRI International
    ATTN: C. Hulbert